Automated Report on the Performance of ANUGA on (all) Validation Test Problems

Sudi Mungkasi, Stephen Roberts, Gareth Davies, Rudy vanDrie

May 4, 2015

Contents

Chapter 1

Introduction

ANUGA is a free and open source software developed by Roberts and collaborators from the Australian National University (ANU) and Geoscience Australia (GA). It is devoted to fluid flow simulations, especially shallow water flows, such as floods, tsunamis and dam breaks. The official website of ANUGA is `http://anuga.anu.edu.au`.

The method implemented in ANUGA is a numerical finite volume method used to solve the shallow water equations. Some mathematical explanation of the method is given in the ANUGA User Manual [24]. In two dimensions, the domain is discretised into finite number of triangular elements. ANUGA then evolves the conserved quantities (water depth and momenta) with respect to time to obtain the numerical solution to a given problem. The evolution is based on the given quantity and flux values. The numerical flux used in ANUGA is the Kurganov's flux [13, 12]. The boundary conditions that we use in this work include reflective, transmissive, Dirichlet and time boundaries.

The results in this report were produced by ANUGA version 2.0 from svn repository revision 9730 at time Sun May 3 23:12:17 2015. The flow algorithm used was DE1, unless otherwise stated explicitly.

To get an automated report, we can run either run individual tests or the complete (whole) test.

To do an individual test, we can run the python module
`produce_results.py`
available in the corresponding test directory. The module will do the numerical simulation of the given problem, plot the simulation results in png files, and typeset the corresponding individual automated report. The individual automated report is in the pdf file `report.pdf` saved in the same directory.

To do the complete test, we can just run the python module
`validations_produce_results.py`
available in the directory
`validation_tests/reports`

Similar to the module for an individual test, this python module will do the numerical simulations of all the given problems, plot results in png files and save them in its corresponding directory, and finally type-set the complete report. The complete automated report is saved in the `validation_tests/reports` directory.

The simulation results can be analysed qualitatively and quantitatively. Qualitative analysis can be done by investigating the plots of the results whether they are physical or not, and whether the behaviour is the same as we expected. Quantitative analysis can be conducted by checking the numerical error.

We have also provided a python script `run_auto_validation_tests.py`in the `validation_tests` directory which will run a subset of the available tests having sensible "correct" results to test against.

The main parameters in the validations are the Courant–Friedrichs-Lewy (CFL) number and the flow algorithm. They are spelled `cfl` and `alg` respectively in the python module
`parameters`
which is available in the
`anuga.validation_tests`
module. In the default setting, we set the CFL to be 1.0 and the flow algorithm to be `DE0` (second order in space and first order in time). The complete available flow algorithms are as follow: `1_0`, `1_5`, `1_75`, `2_0`, `2_0_limited`, `2_5`, `tsunami`, `yusuke`, `DE0`, `DE1`, `DE2`.

They can be found in
`\anuga_core\source\anuga\shallow_water\shallow_water_domain.py`.

The report is organised as follows. We collect a number of tests against analytical exact solutions in Chapter 2. Tests against other reference data or solutions are given in Chapter 3. Tests against realistic case studies are given in Chapter 4, but at present these are not included in this document because they take too much time to run, although the code is provided the source. We provide explanations on how to add new tests in the Appendix.

Chapter 2

Tests against analytical exact solutions

2.1 Dam break involving a dry area

The dam break problem involving a dry area was solved analytically by Ritter [23] as well as Stoker [27, 28]. The analytical solution exhibits a rarefaction fan as a parabolic curve. As water moves, it involves wetting process over the dry area.

The initial condition is

$$u(x,0)=0, \quad v(x,y)=0, \quad \text{and} \quad h(x,0)=\begin{cases} h_1 & \text{if } x<0 \\ 0 & \text{if } x>0 \end{cases} \tag{2.1}$$

where $h_1 > 0$. The topography is a horizontal flat bed.

The analytical solution [23, 27, 28] at time $t > 0$ is

$$h(x)=\begin{cases} h_1 & \text{if } x \le -t\sqrt{gh_1} \\ h_R=\frac{4}{9g}(\sqrt{gh_1}-\frac{x}{2t})^2 & \text{if } -t\sqrt{gh_1} < x \le 2t\sqrt{gh_1} \\ 0 & \text{if } x \ge 2t\sqrt{gh_1} \end{cases} \tag{2.2}$$

which is the free surface and

$$u(x)=\begin{cases} 0 & \text{if } x \le -t\sqrt{gh_1} \\ u_R=\frac{2}{3}(\sqrt{gh_1}+\frac{x}{t}) & \text{if } -t\sqrt{gh_1} < x \le 2t\sqrt{gh_1} \\ 0 & \text{if } x \ge 2t\sqrt{gh_1} \end{cases} \tag{2.3}$$

which is the velocity.

2.1.1 Results

For our test, we consider $h_1 = 10$ in (2.1). The following figures show the stage, x-momentum, and x-velocity at several instants of time. We should see excellent agreement between the analytical and numerical solutions. The wet/dry interface is difficult to resolve and it usually produces large errors.

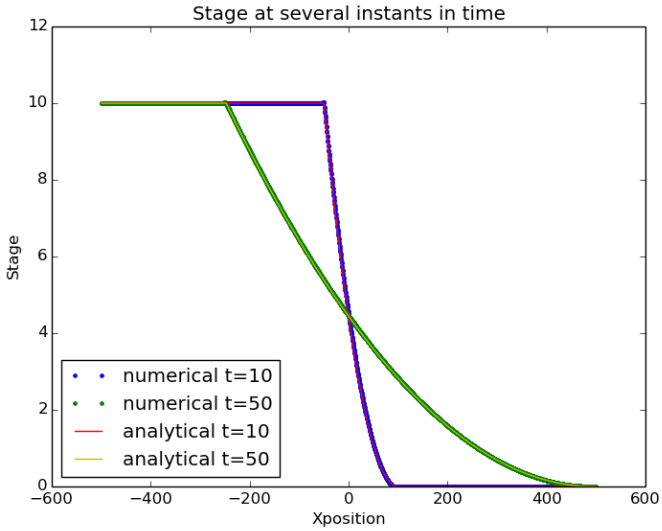

Figure 2.1: Stage results

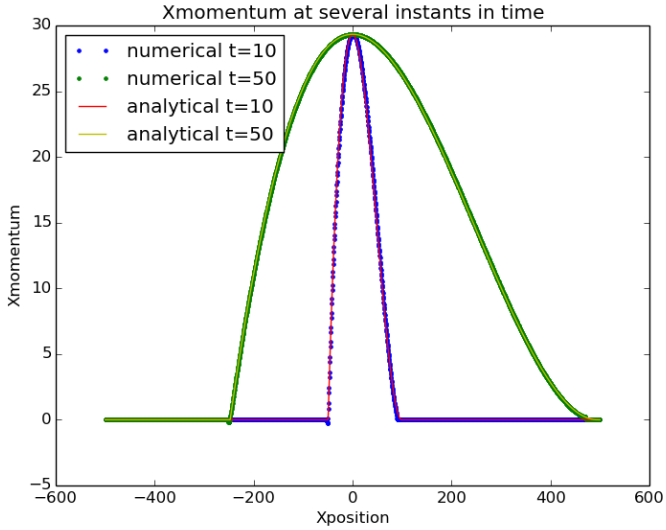

Figure 2.2: Xmomentum results

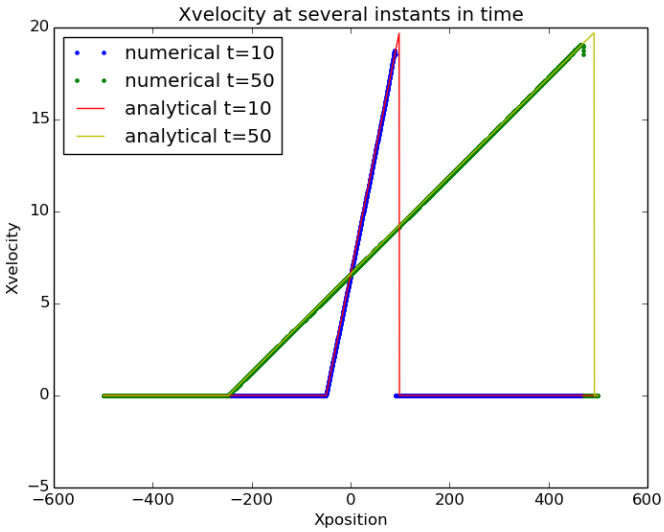

Figure 2.3: Xvelocity results

2.2 Dam break on wet areas

The dam break problem on wet areas was solved analytically by Stoker [27, 28]. The analytical solution exhibits a rarefaction and involves a shock. Generally this problem is easier to solve numerically than the dry dam break (the dam break on a dry area).

The initial condition is

$$u(x,0)=0, \quad v(x,y)=0, \quad \text{and} \quad h(x,0)=\begin{cases} h_1 & \text{if } x<0 \\ h_0 & \text{if } x>0 \end{cases} \tag{2.4}$$

where $h_1 > h_0 > 0$. The topography is a horizontal flat bed.

The analytical solution [27, 28] to the wet dam break problem is

$$h(x)=\begin{cases} h_1 & \text{if } x \le -t\sqrt{gh_1} \\ h_3=\frac{4}{9g}(\sqrt{gh_1}-\frac{x}{2t})^2 & \text{if } -t\sqrt{gh_1} < x \le t(u_2-\sqrt{gh_2}) \\ h_2=\frac{h_0}{2}\left(\sqrt{1+\frac{8\dot{\xi}^2}{gh_0}}-1\right) & \text{if } t(u_2-\sqrt{gh_2}) < x < t\dot{\xi} \\ h_0 & \text{if } x \ge t\dot{\xi} \end{cases} \tag{2.5}$$

and

$$u(x)=\begin{cases} 0 & \text{if } x \le -t\sqrt{gh_1} \\ u_3=\frac{2}{3}(\sqrt{gh_1}+\frac{x}{t}) & \text{if } -t\sqrt{gh_1} < x \le t(u_2-\sqrt{gh_2}) \\ u_2=\dot{\xi}-\frac{gh_0}{4\dot{\xi}}\left(1+\sqrt{1+\frac{8\dot{\xi}^2}{gh_0}}\right) & \text{if } t(u_2-\sqrt{gh_2}) < x < t\dot{\xi} \\ 0 & \text{if } x \ge t\dot{\xi} \end{cases} \tag{2.6}$$

at any time $t > 0$, where $\dot{\xi}$ is the shock speed constant given by

$$\dot{\xi}=2\sqrt{gh_1}+\frac{gh_0}{4\dot{\xi}}\left(1+\sqrt{1+\frac{8\dot{\xi}^2}{gh_0}}\right)-\left(2gh_0\sqrt{1+\frac{8\dot{\xi}^2}{gh_0}}-2gh_0\right)^{\frac{1}{2}}. \tag{2.7}$$

2.2.1 Results

For our test, we consider $h_1 = 10$ and $h_0 = 1$ in (2.4). The following figures show the stage, x-momentum, and x-velocity at several instants of time. We should see excellent agreement between the analytical and numerical solutions.

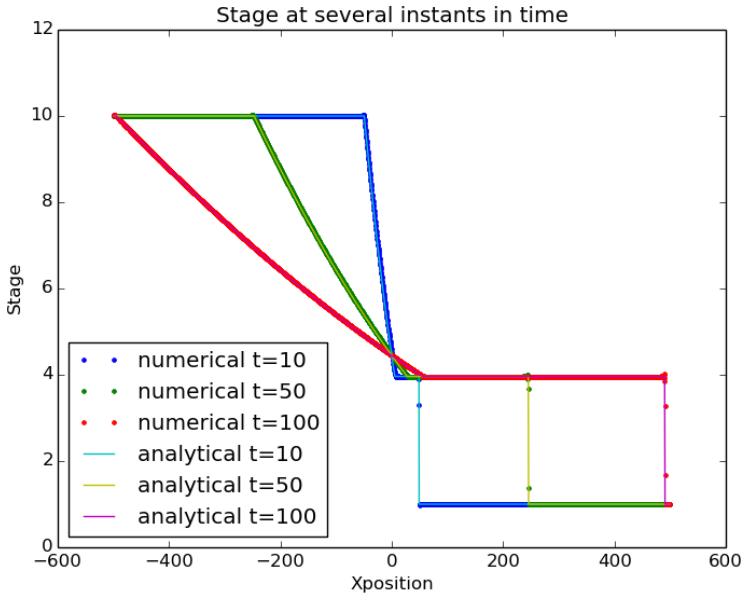

Figure 2.4: Stage results

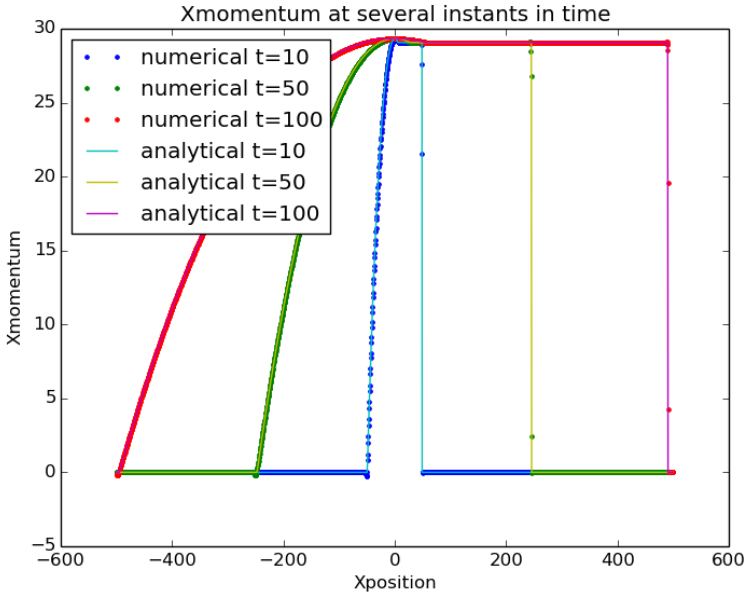

Figure 2.5: Xmomentum results

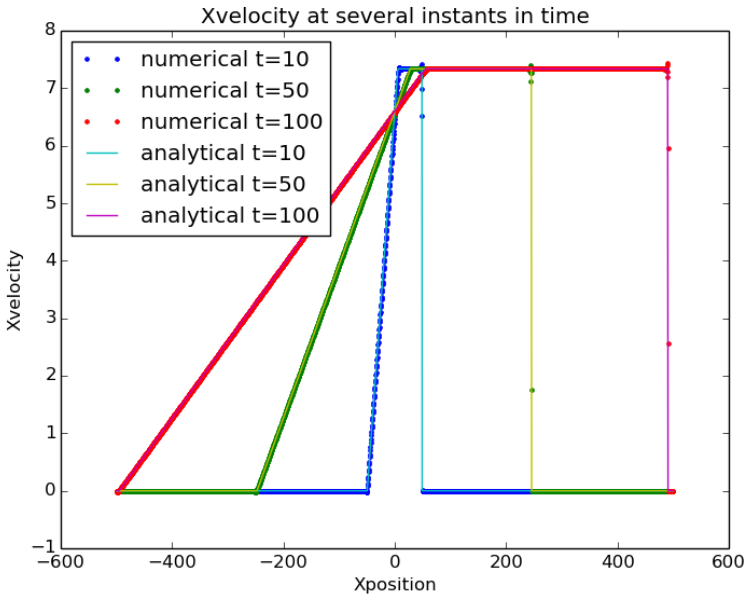

Figure 2.6: Xvelocity results

2.3 Avalanche involving a dry area

An avalanche problem involving a dry area is solved using shallow water approach. This problem is very similar to the dry dam break, but it is on a sloping topography. The debris could be snow, sand, or even rock. The simulation should show a rarefaction and wetting process, just like the dry dam break problem. The analytical solution of this problem was derived by Mungkasi and Roberts [18]. This shallow water approach to solve debris avalanche problems was also implemented by a number of researchers, such as Mangeney et al. [16] and Naaim et al. [21].

The initial condition is

$$u(x,0) = 0, \quad v(x,y) = 0, \quad \text{and} \quad h(x,0) = \begin{cases} h_1 & \text{if } x < 0 \\ 0 & \text{if } x > 0 \end{cases} \tag{2.8}$$

where $h_1 > 0$. The topography is a flat bed with positive slope.

The analytical solution [18] at time $t > 0$ is

$$h(x) = \begin{cases} 0 & \text{if } x \leq -2c_0 t + \frac{1}{2}mt^2 \\ h_R = \frac{1}{9g}\left(\frac{x}{t} + 2c_0 - \frac{1}{2}mt\right)^2 & \text{if } -2c_0 t + \frac{1}{2}mt^2 \leq x \leq c_0 t + \frac{1}{2}mt^2 \\ h_0 & \text{if } x \geq c_0 t + \frac{1}{2}mt^2 \end{cases} \tag{2.9}$$

which is the free surface and

$$u(x) = \begin{cases} 0 & \text{if } x \leq -2c_0 t + \frac{1}{2}mt^2 \\ u_R = \frac{2}{3}\left(\frac{x}{t} - c_0 + mt\right) & \text{if } -2c_0 t + \frac{1}{2}mt^2 \leq x \leq c_0 t + \frac{1}{2}mt^2 \\ mt & \text{if } x \geq c_0 t + \frac{1}{2}mt^2 \end{cases} \tag{2.10}$$

which is the velocity. Here $m = -g\tan\theta + F$, where $\tan\theta$ is the slope of the topography. Variable F is the Coulomb-type friction given by

$$F = g\cos^2\theta \tan\delta, \tag{2.11}$$

in which $\tan\delta$ is a given value of friction slope such that $\tan\delta \leq \tan\theta$.

2.3.1 Results

For our test, we consider $h_0 = 20$ in (2.8). The following figures show the stage, x-momentum, and x-velocity at several instants of time. We should see excellent agreement between the analytical and numerical solutions. The wet/dry interface is difficult to resolve and it usually produces large errors, similar to the dry dam break problem.

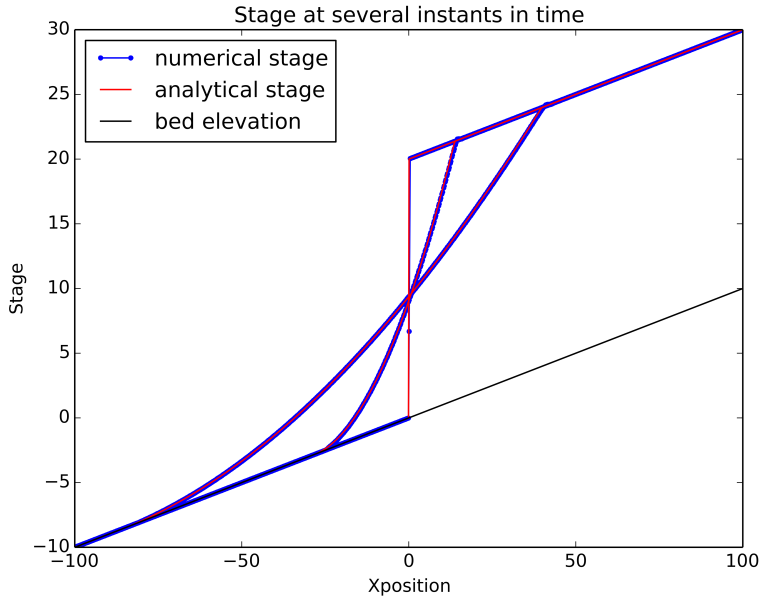

Figure 2.7: Stage results

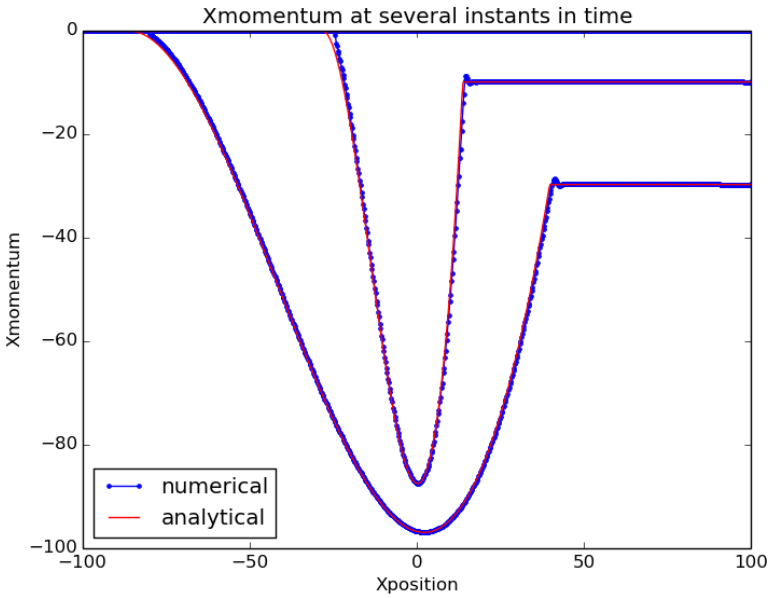

Figure 2.8: Xmomentum results

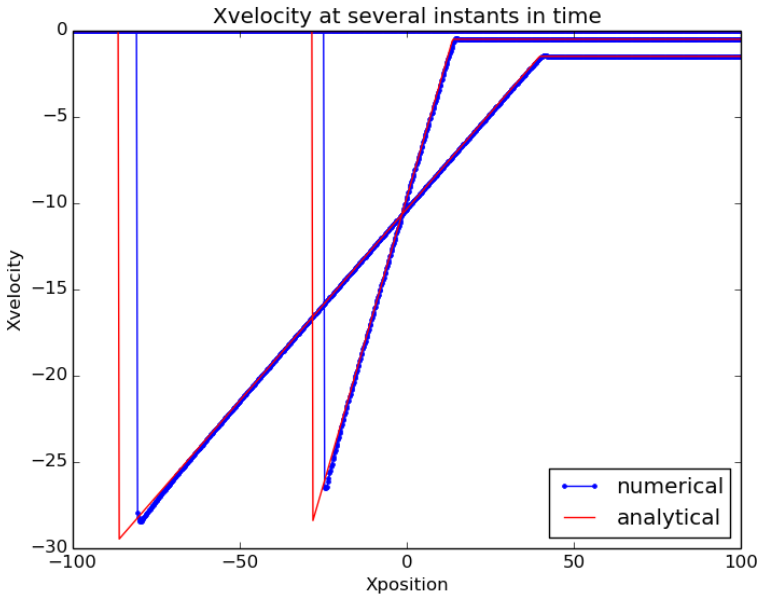

Figure 2.9: Xvelocity results

2.4 Avalanche involving a shock wave

We consider an avalanche involving a shock wave. This problem is similar to dam break on wet areas, and so, it involves a shock. We consider a flat topography with positive slope. Shallow water approach is used to solve the problem. The analytical solution of this problem was derived by Mungkasi and Roberts [19]. This shallow water approach was also implemented by a number of researchers, such as Mangeney et al. [16] and Naaim et al. [21]. The simulation should show a rarefaction and a shock.

The initial condition is

$$u(x,0)=0, \quad v(x,y)=0, \quad \text{and} \quad h(x,0)=\begin{cases} h_1 & \text{if } x<0 \\ h_0 & \text{if } x>0 \end{cases} \tag{2.12}$$

where $h_0 > h_1 > 0$. The topography is a flat bed with positive slope. Note that when $h_1 = 0$, the problem becomes avalanche involving a dry area [18].

The analytical solution [19] at time $t > 0$ is

$$h(x,t)=\begin{cases} h_1 & \text{if } x < \sigma t + \frac{1}{2}mt^2\,, \\ h_2 & \text{if } \sigma t + \frac{1}{2}mt^2 \le x < (u_2+c_2)t + \frac{1}{2}mt^2\,, \\ \frac{1}{9g}\left(\frac{x}{t} + 2c_0 - \frac{1}{2}mt\right)^2 & \text{if } (u_2+c_2)t + \frac{1}{2}mt^2 \le x < c_0 t + \frac{1}{2}mt^2\,, \\ h_0 & \text{if } x \ge c_0 t + \frac{1}{2}mt^2\,, \end{cases} \tag{2.13}$$

and

$$u(x,t)=\begin{cases} mt & \text{if } x < \sigma t + \frac{1}{2}mt^2\,, \\ u_2 + mt & \text{if } \sigma t + \frac{1}{2}mt^2 \le x < (u_2+c_2)t + \frac{1}{2}mt^2\,, \\ \frac{2}{3}\left(\frac{x}{t} - c_0 + mt\right) & \text{if } (u_2+c_2)t + \frac{1}{2}mt^2 \le x < c_0 t + \frac{1}{2}mt^2\,, \\ mt & \text{if } x \ge c_0 t + \frac{1}{2}mt^2\,, \end{cases} \tag{2.14}$$

for time $t > 0$. Here u_2, c_2, and σ are the solutions of the three simultaneous equations

$$u_2 = \sigma - \frac{c_1^2}{4\sigma}\left(1 + \sqrt{1 + 8\left(\frac{\sigma}{c_1}\right)^2}\right), \tag{2.15}$$

$$c_2 = c_1\sqrt{\frac{1}{2}\left(\sqrt{1 + 8\left(\frac{\sigma}{c_1}\right)^2} - 1\right)}, \tag{2.16}$$

and

$$-2c_0 = u_2 - 2c_2. \tag{2.17}$$

The value of h_2 is calculated using relation $c_2 = \sqrt{gh_2}$. Here $m = -g\tan\theta + F$, where $\tan\theta$ is the slope of the topography. Variable F is the Coulomb-type friction given by

$$F = g\cos^2\theta\tan\delta, \tag{2.18}$$

in which $\tan\delta$ is a given value of friction slope such that $\tan\delta \le \tan\theta$.

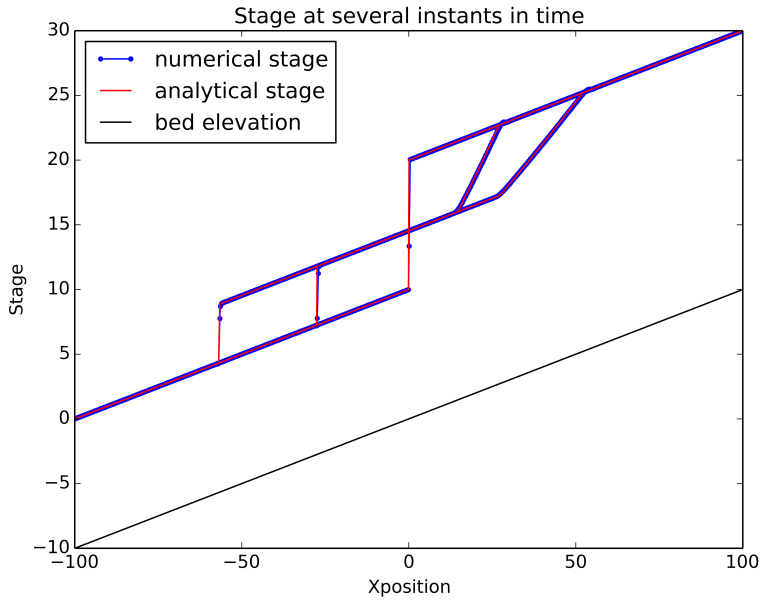

Figure 2.10: Stage results

2.4.1 Results

For our test, we consider $h_0 = 20$ and $h_1 = 10$ in (2.12). The following figures show the stage, x-momentum, and x-velocity at several instants of time. We should see excellent agreement between the analytical and numerical solutions.

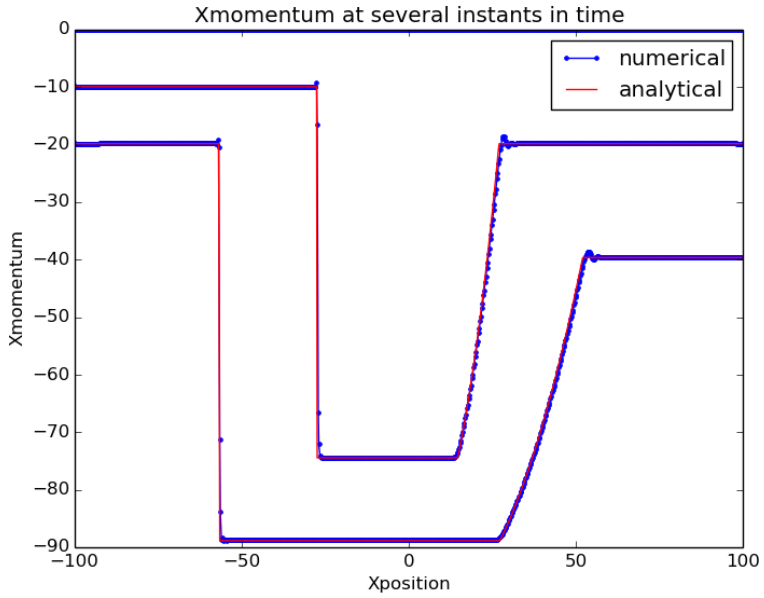

Figure 2.11: Xmomentum results

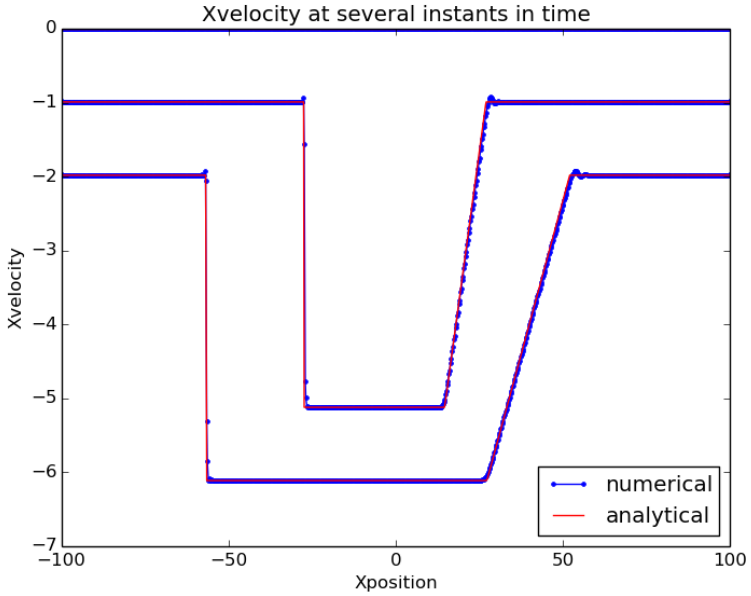

Figure 2.12: Xvelocity results

2.5 Carrier-Greenspan periodic solution

Periodic solutions for flows on a sloping beach were proposed by Carrier and Greenspan [2]. The solutions have been widely used to test the performance of numerical methods used to solve the shallow water equations [10, 20].

This test can be described in dimensional and dimensionless equations. For our reference, please note that dimensional quantities shall be denoted by starred variables, while dimensionless quantities by unstarred variables for brevity of our analytical presentation. This notational convention is used only in this test.

The problem is set up as follows. Consider a one dimensional domain through the x^*-axis. Recall the shallow water equations

$$h^*_{t^*} + (h^* u^*)_{x^*} = 0\,, \tag{2.19}$$

$$(h^* u^*)_{t^*} + \left(h^* u^{*2} + \frac{1}{2} g h^{*2}\right)_{x^*} = -g h^* z^*_{x^*}\,. \tag{2.20}$$

Here, x^* represents the one-dimensional domain, t^* is the time variable, $u^* = u^*(x^*, t^*)$ represents the velocity, $z^* = z^*(x^*)$ denotes the water bed topography (elevation), $h^* = h^*(x^*, t^*)$ denotes the height (water depth), that is, the distance from the free surface to the water bed topography, and g is the acceleration due to gravity. Now, consider the situation on a sloping beach. The topography changes linearly with x^*

$$z^* = (h^*_0/L^*)x^* - h^*_0\,, \tag{2.21}$$

in which h^*_0 is the vertical distance from the origin O to the topography at any time, and L^* is the horizontal distance from the origin O to the topography when the water is still. This implies that when the water is still: $z^* = -h^*$ over the spatial domain, $z^* = -h^*_0$ at $x^* = 0$, and the position of the shoreline is $x^* = L^*$. More detailed descriptions are given by Mungkasi and Roberts [20].

The free surface or called stage is defined by $w^* := h^* + z^*$. Scaling the horizontal distance by L^*, the vertical distance by h^*_0, the time by $L^*/\sqrt{g h^*_0}$, and the velocity by $\sqrt{g h^*_0}$, the nonconservative dimensionless shallow water equations can be expressed as

$$w_t + [(w + 1 - x)\, u]_x = 0\,, \tag{2.22}$$

$$u_t + u u_x + w_x = 0\,. \tag{2.23}$$

For smooth solutions, equations (2.22) and (2.23) are equivalent to the conservative dimensionless shallow water wave equations

$$h_t + (hu)_x = 0\,, \tag{2.24}$$

$$(hu)_t + \left(hu^2 + \frac{1}{2}h^2\right)_x = -hz_x\,. \tag{2.25}$$

Carrier and Greenspan showed that

$$w = -\frac{1}{2}u^2 + \mathcal{A}J_0\left(\frac{4\pi\sqrt{w+1-x}}{T}\right)\cos\left(\frac{2\pi\,(u+t)}{T}\right), \tag{2.26}$$

$$u = -\frac{\mathcal{A}J_1\left(\frac{4\pi\sqrt{w+1-x}}{T}\right)}{\sqrt{w+1-x}}\sin\left(\frac{2\pi\,(u+t)}{T}\right) \tag{2.27}$$

satisfies the shallow water equations. This was verified by Johns [10] as well as Mungkasi and Roberts [20]. Equations (2.26) and (2.27) are the Carrier–Greenspan periodic solutions for flows on a sloping beach, which are written in the dimensionless form. Obviously, this can be rescalled back to the dimensional form.

Because this solution is periodic, the initial condition can be set by substituting $t = 0$ into the analytical solution (2.26) and (2.27).

2.5.1 Results

We consider a spatial domain given by the interval $[-50, 55050]$. The dimensional length is $L^* = 50,000$, dimensional height $h_0^* = 500$, and dimensional period $T^* = 900$. At $x^* = 0$ the dimensional amplitude is $\epsilon^* = 1.0$. After four cycles, periodic motions are clear.

The following figures show the stage, x-momentum, and x-velocity at several instants of time through a cross-section of the domain. Perturbation at the zero point of the spatial domain is also shown. We should see excellent agreement between the analytical and numerical solutions.

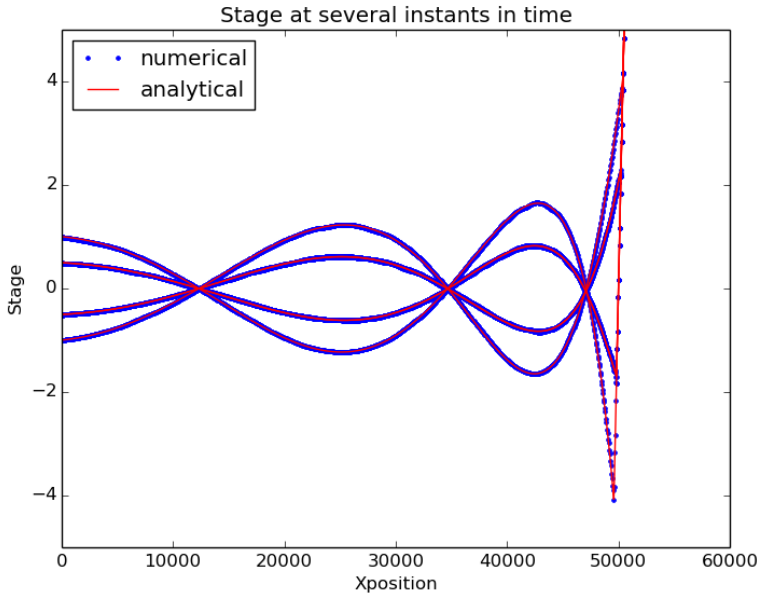

Figure 2.13: Stage results

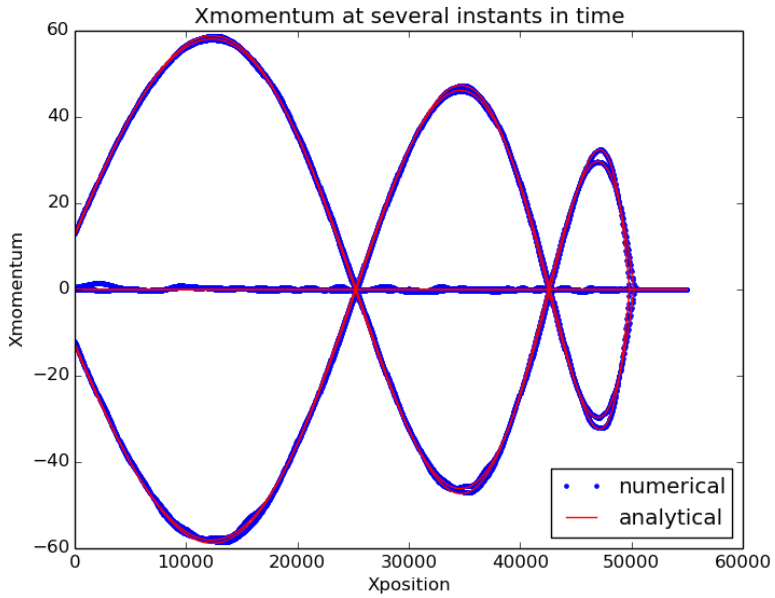

Figure 2.14: Xmomentum results

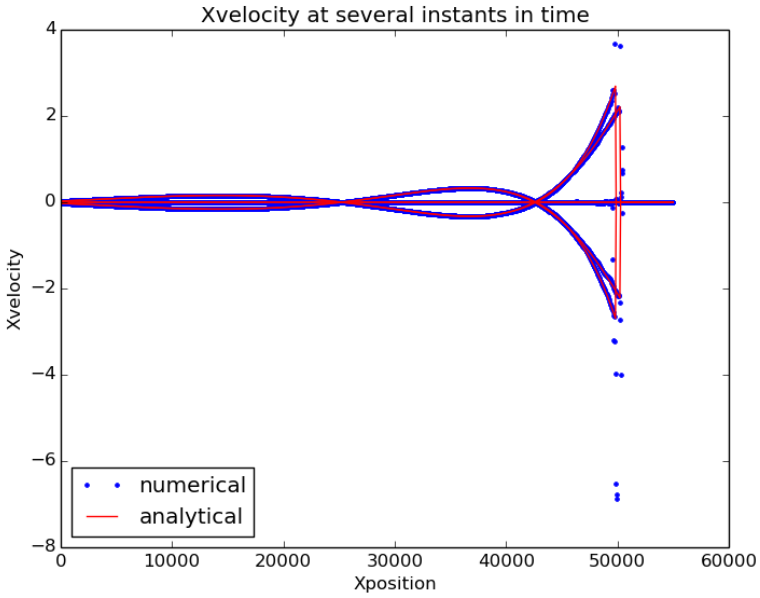

Figure 2.15: Xvelocity results

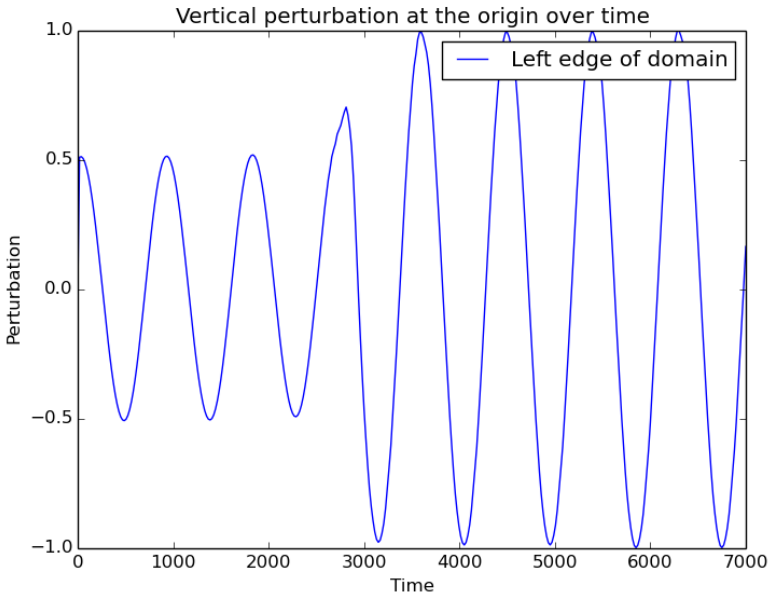

Figure 2.16: Perturbation at the origin

2.6 Carrier–Greenspan transient solution

A transient solution for flows on a sloping beach was proposed by Carrier and Greenspan [2]. The water moves to the shore at an early time, then it becomes still when time is large.

Consider the dimensionless shallow water equations, as presented in the Carrier–Greenspan periodic solution.

The analytical solution is:

$$w = -\frac{u^2}{2} + \epsilon Re\left[1 - 2\frac{5/4 - i\lambda}{\{(1-i\lambda)^2+\sigma^2\}^{3/2}} + \frac{3}{2}\frac{(1-i\lambda)^2}{\{(1-i\lambda)^2+\sigma^2\}^{5/2}}\right], \tag{2.28}$$

$$u = \frac{8\epsilon}{a} Im\left[\frac{1}{\{(1-i\lambda)^2+\sigma^2\}^{3/2}} - \frac{3}{4}\frac{1-i\lambda}{\{(1-i\lambda)^2+\sigma^2\}^{5/2}}\right], \tag{2.29}$$

where

$$t = \frac{1}{2}a\lambda - u\,, \quad c = \frac{1}{4}a\sigma\,, \tag{2.30}$$

in which $c = \sqrt{gh}$ is the wave propagation speed. Here $\sigma \geq 0$ and we take $a = 1.5(1 + 0.9\epsilon)^{1/2}$. Carrier and Greenspan [2] observed that the waves do not break if ϵ is very small, namely $\epsilon \leq 0.23$. Setting $\sigma = 0$ into this solution, we get the motion of the shoreline.

The initial condition is given by setting time $t = 0$ in this analytical solution. Note that this analytical solution is defined in the dimensionless space. To implement this in the numerical test, we just need to scale it back to the dimensional space.

2.6.1 Results

We consider $\epsilon = 0.2$. The following three figures show the stage, x-momentum, and y-momentum at several instants in time. We should see excellent agreement between the analytical and numerical solutions.

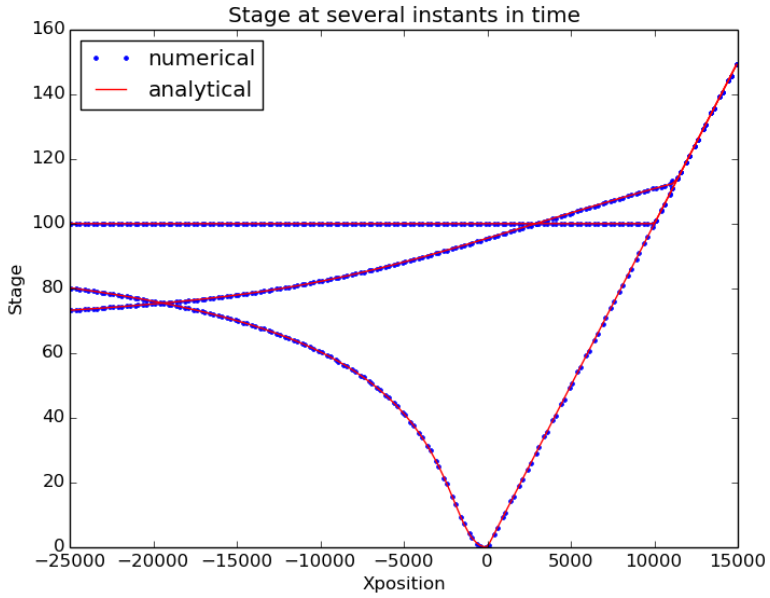

Figure 2.17: Stage results

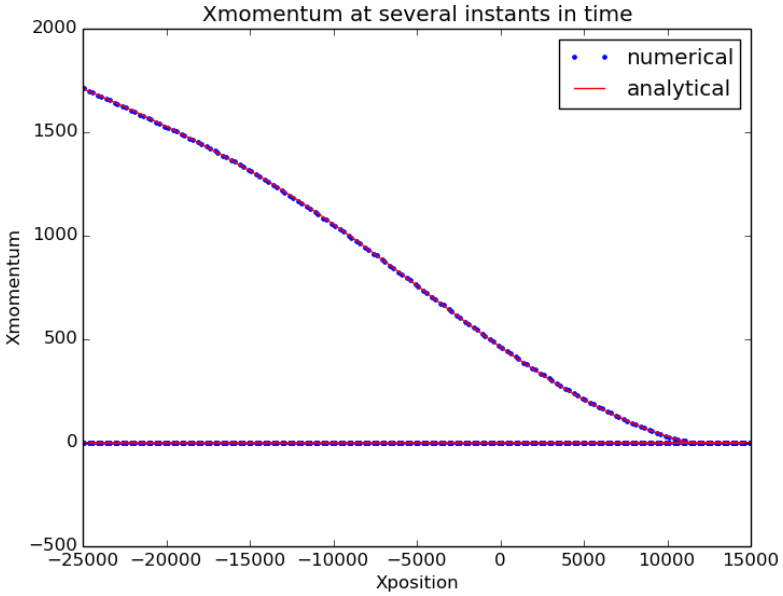

Figure 2.18: Xmomentum results

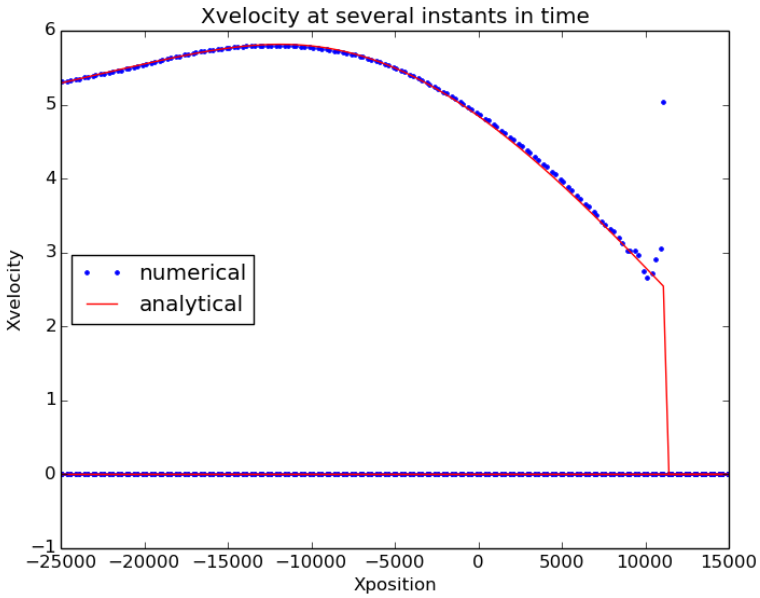

Figure 2.19: Xvelocity results

2.7 Deep Water Wave Propagation

This simulates the free propagation of a sinusoidal wave in deep water. The initial condition is still water in a "large" box with uniform depth. The wave is generated from the left boundary and propagates to the right. The depth on the right boundary is set as time dependent function

$$h(t) = A \sin \frac{2\pi t}{\lambda} \tag{2.31}$$

with $u = v = 0$. Here A is the amplitude of the generating wave, t is time variable, and λ is the wave length as well as the period of the generating wave.

Analytically, the wave should travel through the domain without deformation. Lower-order-accuracy algorithms may result in undue wave dampening with the mesh size used in the current problem. This can have practical implications e.g. for tsunami propagation problems, and is usually dealt with by using second-order accurate methods. Alternatively you can refine the mesh until the dampening becomes insignificant, but this may be computationally expensive in realistic problems.

This example can also illustrate difficulties with radiation-type boundary conditions where the wave exits the domain (of course, for this problem, we could do that by exploiting the analytical solution - but this is not possible for general wave propagation problems). This will most obviously affect the right edge of the domain, but its effects will ultimately be felt throughout.

2.7.1 Results

In this test, we consider $A = 1$ and $\lambda = 300$. Figure 2.20 shows the time-evolution of the water elevation at three points in the domain. Ideally these time series should show the wave propagating without deformation or attenuation (i.e. the wave has the same shape, amplitude, period, mean water level etc. at each point).

The corresponding momentums of Figure 2.20 are shown in Figures 2.21 and 2.22.

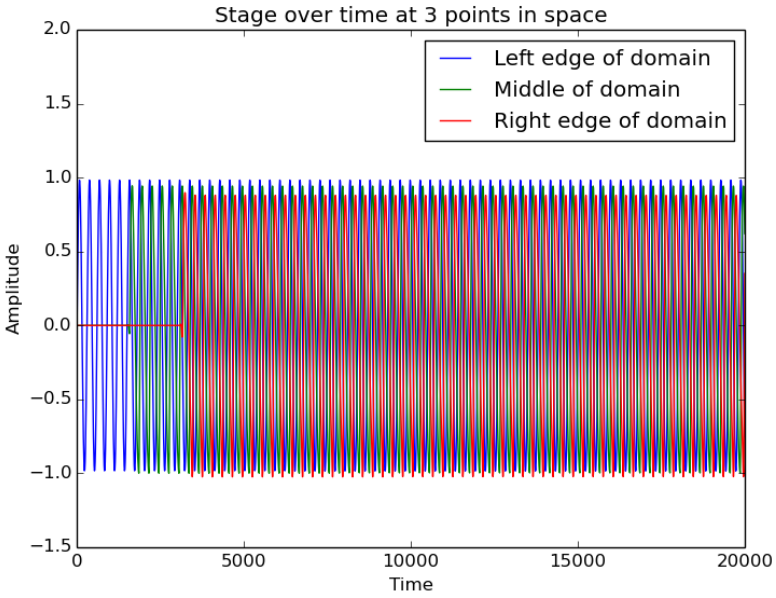

Figure 2.20: Stage over time at 3 points in space

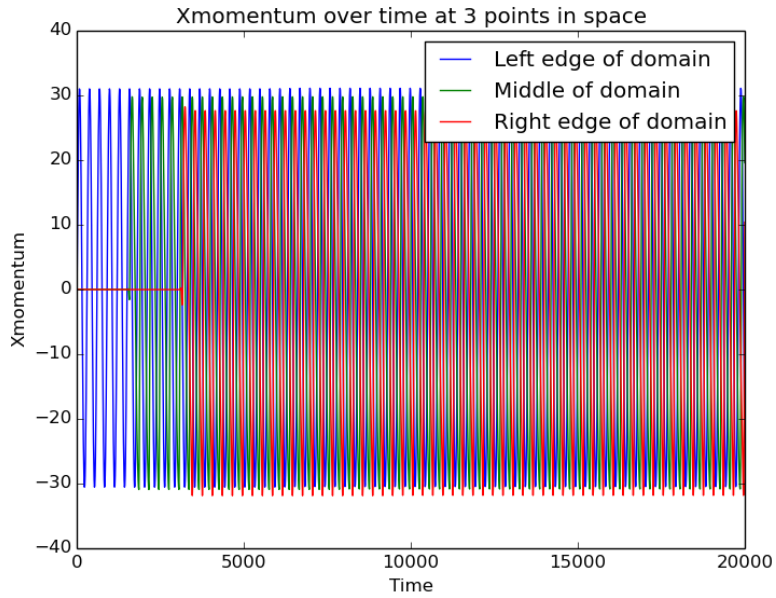

Figure 2.21: Xmomentum over time at 3 points in space

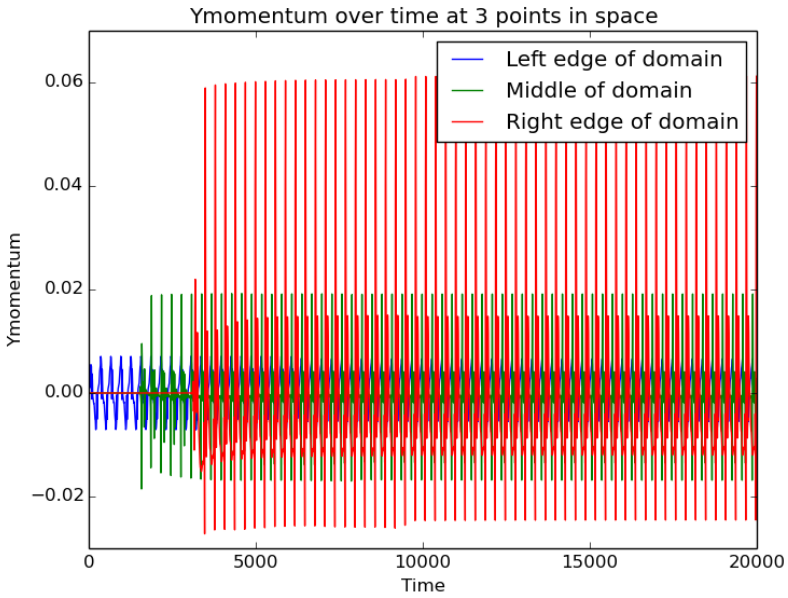

Figure 2.22: Ymomentum over time at 3 points in space

2.8 A MacDonald's solution: transcritical flow with a shock

This is a MacDonald's steady flow test involving a shock in a short channel. This test was used by Delestre et al. [6] in their SWASHES benchmark library of shallow water analytical solutions. The original derivation of the analytical solution was given by MacDonald et al. [14, 15]. MacDonald's analytical solution was derived using a backward framework, that is: given the water depth, we construct the topography which satisfies the shallow water equations.

When water is in a steady state, we have a fixed depth and velocity with respect to time. Consider a one dimensional domain. Suppose that we are given the depth $h(x)$. The steady state conditions make the shallow water equations to the single identity

$$z_x = \left(\frac{q^2}{gh^3} - 1\right) h_x - S_f \tag{2.32}$$

where $q = uh$ is the momentum or water discharge and S_f is the symbol for the force of bottom friction involving Manning's coefficient n. We take

$$S_f = n^2 \frac{q|q|}{h^{10/3}}. \tag{2.33}$$

The topography is then determined by

$$z(x) = -\int_x^L z_x \, dx \tag{2.34}$$

in which L is the channel length.

2.8.1 Results

For our test, suppose that the channel length $L = 100$ and at steady state the discharge $q = 2$. The initial condition is $u = v = 0$ and $w = 2.87870797$. The boundary condition is enforced such that the upstream boundary has $q = 2$ and the downstream boundary has $h = 100$. When water is steady, suppose that a shock occurs at $x = 66\frac{2}{3}$. Following Delestre et al. [6], we consider the water depth

$$h(x,y) = \begin{cases} \left(\frac{4}{g}\right)^{1/3} \left(\frac{4}{3} - \frac{x}{100}\right) - \frac{9x}{1000}\left(\frac{x}{100} - \frac{2}{3}\right) & \text{if} \quad 0 \le x < 66\frac{2}{3} \\ \left(\frac{4}{g}\right)^{1/3} \Big[a_1 \left(\frac{x}{100} - \frac{2}{3}\right)^4 + a_1 \left(\frac{x}{100} - \frac{2}{3}\right)^3 \\ \quad -a_2 \left(\frac{x}{100} - \frac{2}{3}\right)^2 + a_3 \left(\frac{x}{100} - \frac{2}{3}\right) + a_4\Big] & \text{if} \quad 66\frac{2}{3} \le x \le 100 \end{cases} \tag{2.35}$$

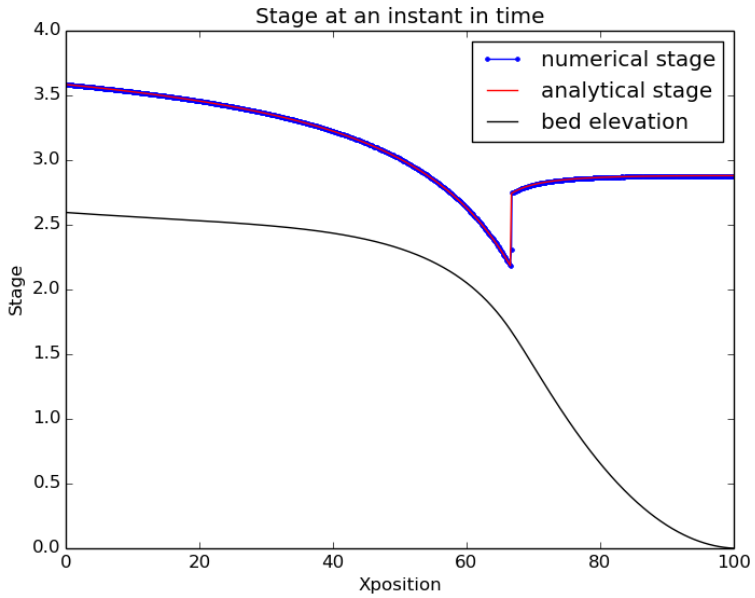

Figure 2.23: Stage results

where $a_1 = 0.674202$, $a_2 = 21.7112$, $a_3 = 14.492$, $a_4 = 1.4305$, and $n = 0.0328$.

The following three figures show the stage, x-momentum, and x-velocity when water is steady. We should see excellent agreement between the analytical and numerical solutions.

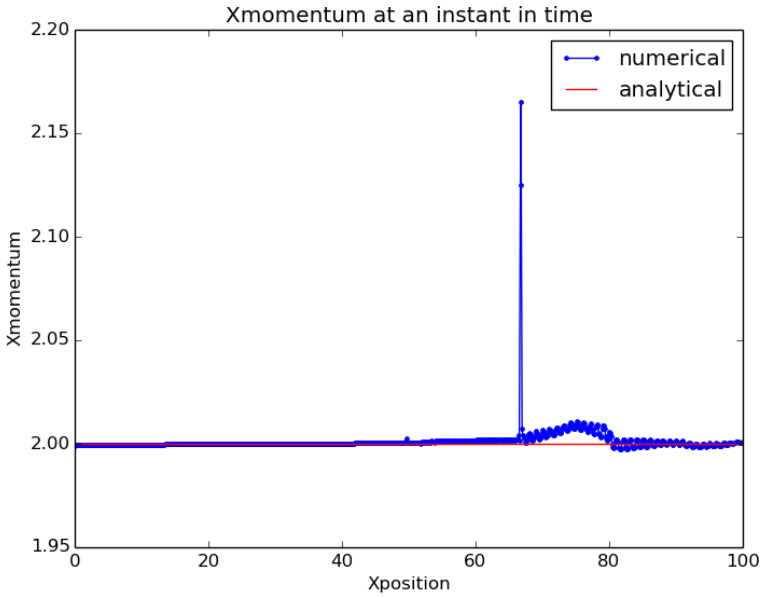

Figure 2.24: Xmomentum results

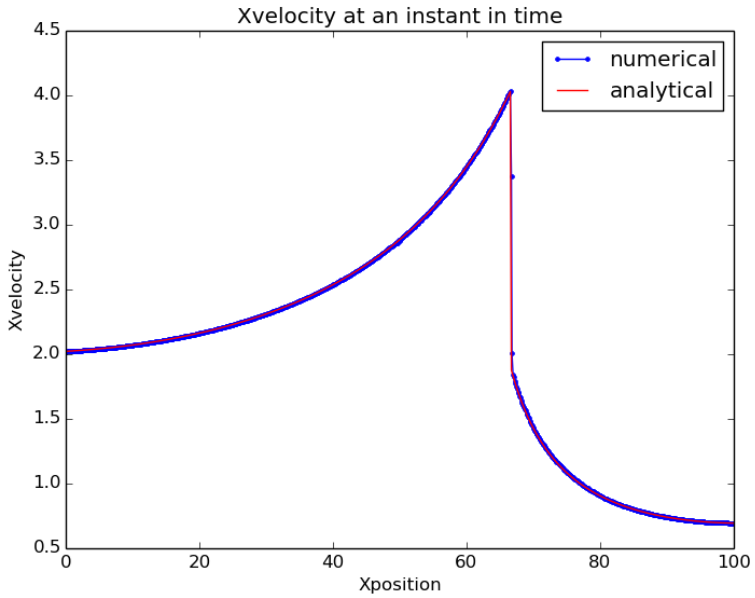

Figure 2.25: Xvelocity results

2.9 Thacker's Planar Oscillations on a Parabolic Basin

This test simulates planar oscillations of water in a parabolic basin. The analytical solution was derived by Thacker [29], and is periodic. At any instant in time, the free surface elevation is planar, and the velocity is constant (in wet regions). The scenario includes regular wetting and drying, as the flow oscillates back and forth in the basin. As well as testing the ability of the code to do wetting and drying, it will highlight any numerical energy loss or gain, and manifest as an increase or decrease in the magnitude of the flow oscillations over long time periods (compared with the analytical solution).

Consider the topography

$$z(x) = D_0 \left(\frac{x}{L}\right)^2 \tag{2.36}$$

where D_0 is the largest depth when water is still and L is the distance between the centre of water surface and the shore when water is still. The analytical solution is

$$u(x,t) = -A\omega \sin(\omega t), \tag{2.37}$$

$$w(x,t) = D_0 + \frac{2AD_0}{L^2}\cos(\omega t)\left(x - \frac{A}{2}\cos(\omega t)\right). \tag{2.38}$$

Here $\omega = \frac{\sqrt{2gD_0}}{L}$. The initial condition is set by taking $t = 0$ in the analytical solution.

2.9.1 Results

For our test, we consider $D_0 = 4$, $L = 10$, and $A = 2$. After running the simulation for some time, we have Figures 2.26–2.28 showing the stage, x-momentum, and x-velocity respectively. There should be a good agreement between numerical and analytical solutions. Small velocity spikes may appear at the moving wet-dry edge in some ANUGA algorithms. As time goes on, some small deviations may also appear. These are shown in Figures 2.29–2.31, which illustrate the stage, x-momentum, and x-velocity at the centroid of the domain.

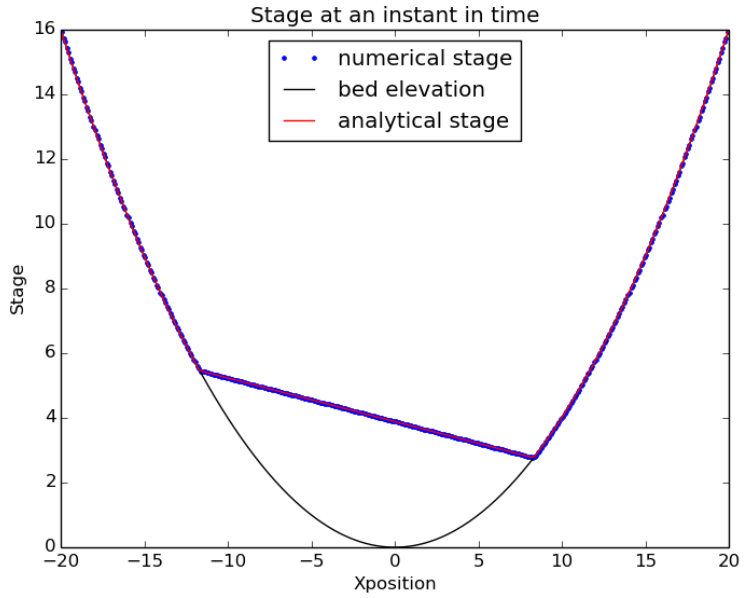

Figure 2.26: Stage on a cross section of the basin at time $t = 10$.

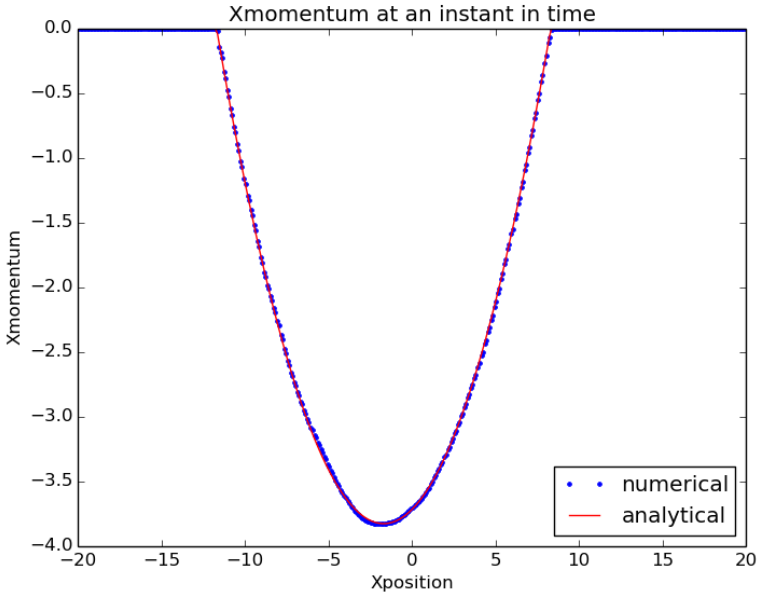

Figure 2.27: Xmomentum on a cross section of the basin at time $t = 10$.

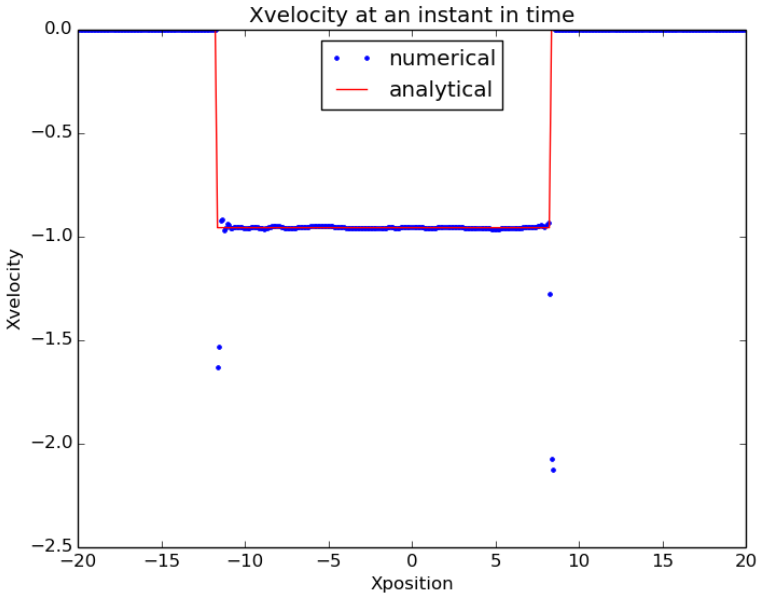

Figure 2.28: Xvelocity on a cross section of the basin at time $t = 10$.

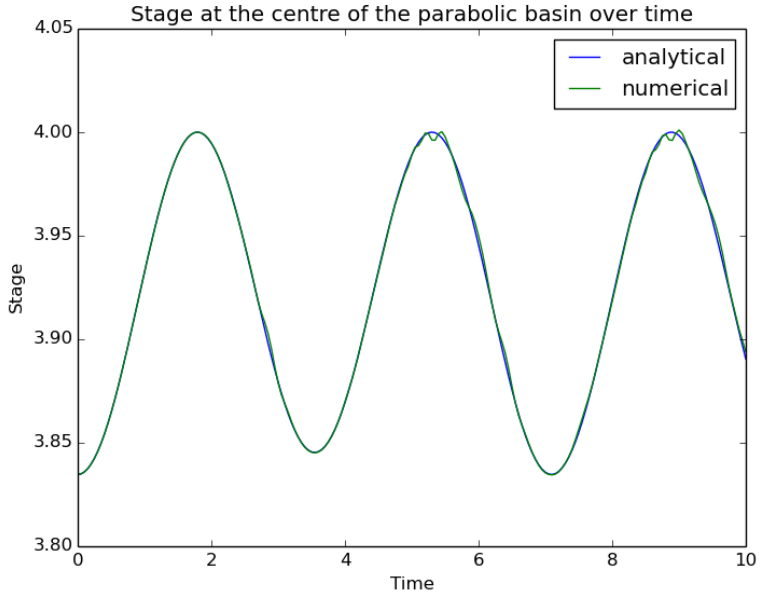

Figure 2.29: Stage over time in the centre of the parabolic basin.

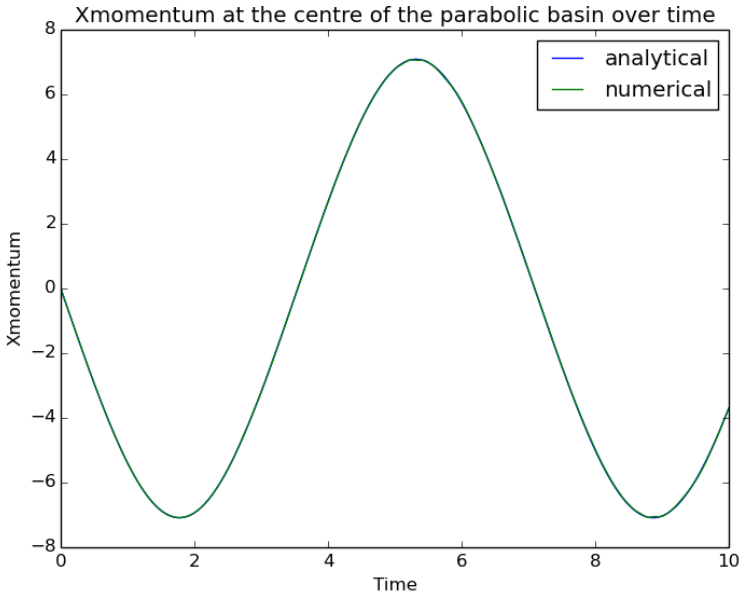

Figure 2.30: Xmomentum over time in the centre of the parabolic basin.

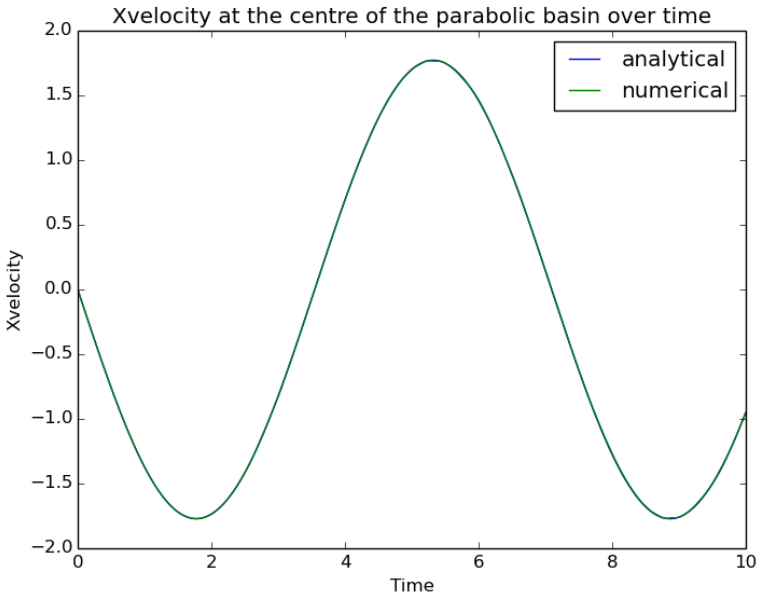

Figure 2.31: Xvelocity over time in the centre of the parabolic basin.

2.10 Oscillations on a paraboloid basin

This test simulates water oscillations on a paraboloid basin. The analytical solution was derived by Thacker [29], and is periodic. At any instant in time, the free surface elevation is paraboloid, and the velocity is linear. The scenario includes regular wetting and drying, as the flow oscillates up and down in the basin. As well as testing the ability of the code to do wetting and drying, it will highlight any numerical energy loss or gain, and manifest as an increase or decrease in the magnitude of the flow oscillations over long time periods (compared with the analytical solution). This test was also implemented by Yoon and Cho [30] to investigate the performance of their numerical method.

Consider the topography in two dimensions

$$z(x, y) = -D_0 \left[1 - \left(\frac{r}{L}\right)^2\right] \tag{2.39}$$

where $r = \sqrt{x^2 + y^2}$. Here D_0 is the largest depth when water is still and L is the distance between the centre of water surface and the shore when water is still. The analytical solution is

$$u(x, y, t) = \frac{\omega r A \sin(\omega t)}{2\left[1 - A\cos(\omega t)\right]}, \tag{2.40}$$

$$w(x, y, t) = D_0 \left[\frac{\sqrt{(}1 - A^2)}{1 - A\cos(\omega t)} - 1 - \left(\frac{r}{L}\right)^2 \frac{1 - A^2}{[(1 - A\cos(\omega t))^2] - 1}\right]. \tag{2.41}$$

Here $\omega = \frac{2\sqrt{2gD_0}}{L}$ and $A = \frac{L^4 - R_0^4}{L^4 + R_0^4}$ and R_0 is the horizontal distance between the centre of water surface and the shore at the initial condition. The initial condition is set by taking $t = 0$ in the analytical solution.

2.10.1 Results

For our test, we consider $D_0 = 1000$, $L = 2500$, and $R_0 = 2000$. After running the simulation for some time, we have Figures 2.32–2.34 showing the stage, x-momentum, and x-velocity respectively. There should be a good agreement between numerical and analytical solutions, although wet-dry artefacts may appear in the 'nearly-dry' areas, where the numerical method can cause the water to drain too slowly (similar to that reported in [11] using a finite volume scheme with similarities to discontinuous elevation algorithms in ANUGA).

As time goes on, some small deviations may appear. These are shown in Figures 2.35–2.37, which illustrate the stage, x-momentum, and x-velocity at the centroid of the domain.

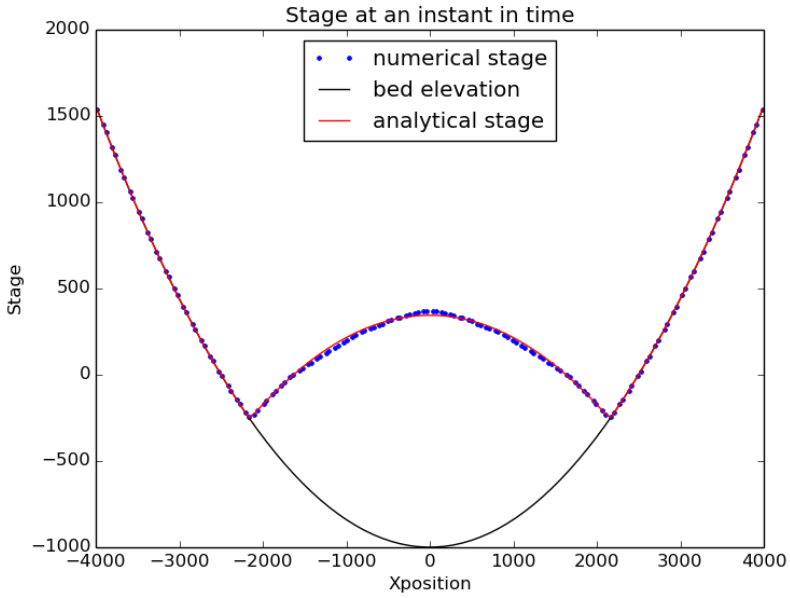

Figure 2.32: Stage on a cross section of the basin at time $t = 50$.

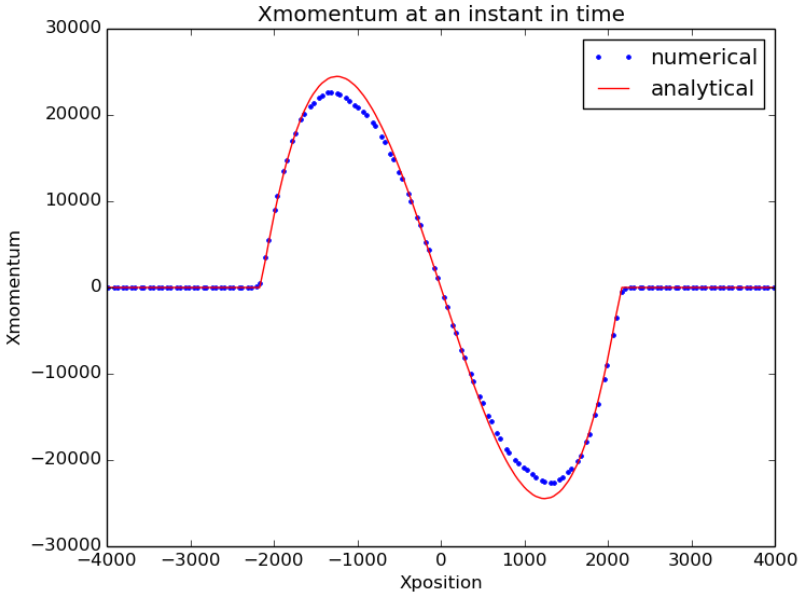

Figure 2.33: Xmomentum on a cross section of the basin at time $t = 50$.

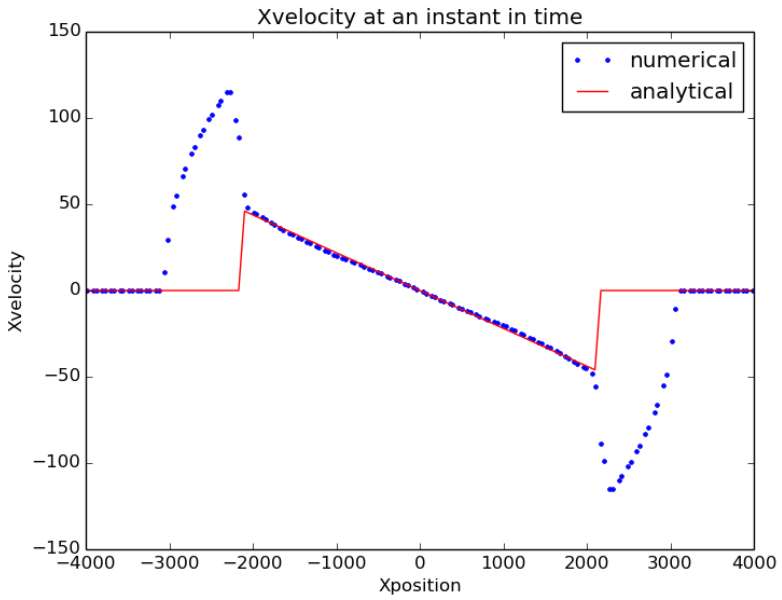

Figure 2.34: Xvelocity on a cross section of the basin at time $t = 50$.

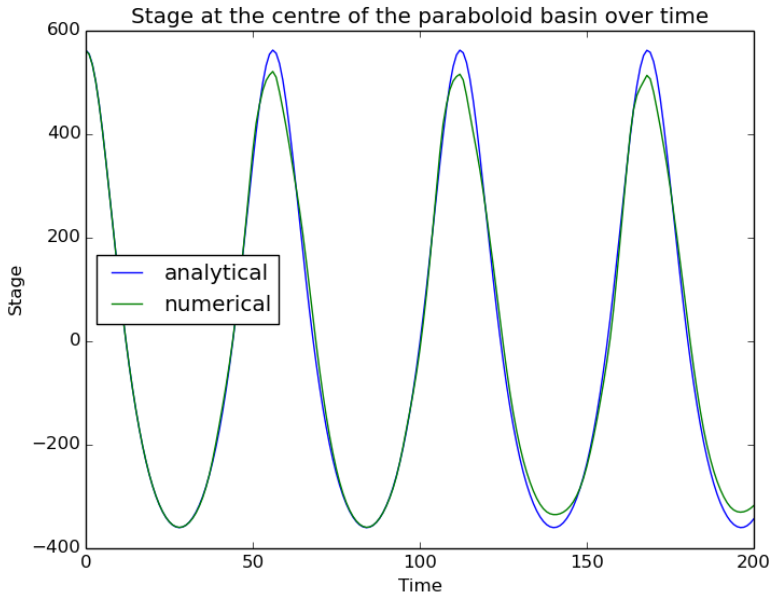

Figure 2.35: Stage over time in the centre of the paraboloid basin.

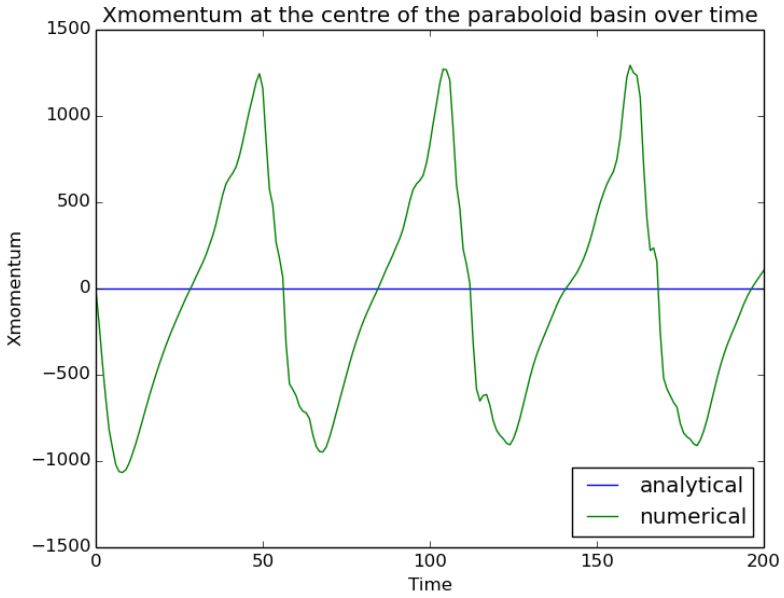

Figure 2.36: Xmomentum over time in the centre of the paraboloid basin.

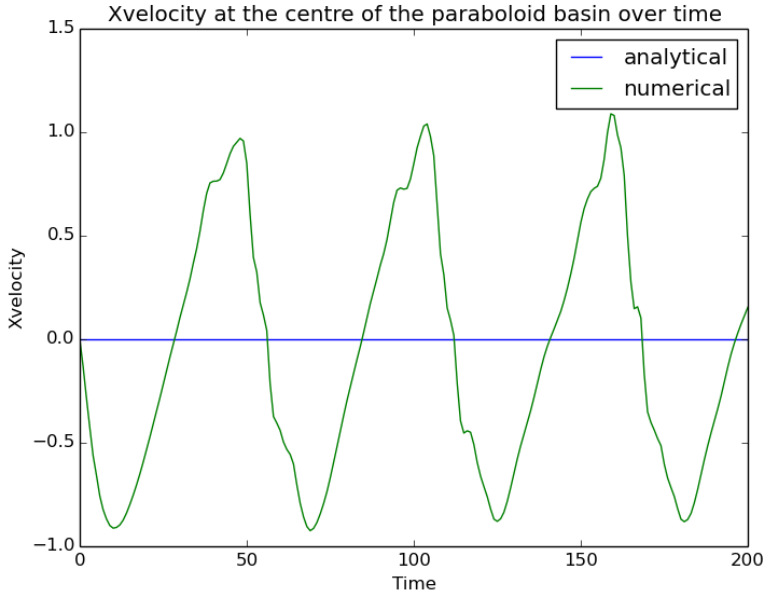

Figure 2.37: Xvelocity over time in the centre of the paraboloid basin.

2.11 Simple wave runup

This scenario simulates a wave flowing up a planar beach. Following the initial wave runup, eventually the water elevation should become constant, and the velocities should approach zero. This test follows from the ANUGA User Manual [24]. Instead of demonstrating how ANUGA simulates a water flow test as given in the ANUGA User Manual [24], here we investigate the behaviour of the wetting (and possibly the drying) process handled by ANUGA.

2.11.1 Results

To do the investigation, we consider initial and boundary conditions different from those given in the ANUGA User Manual [24] so that we have a large dry region. Consider a rectangular domain with $x \in [0, 1]$ and $y \in [0, 0.03]$. The initial conditions are $u = v = 0$ and

$$z(x) = -\frac{x}{2} \tag{2.42}$$

with the stage at wet region is $w = -0.45$. The boundary condition on the rightend of the domain is Dirichlet with stage $w = -0.4$ and discharges in x and y directions are zero.

At an early runup, representatives of the results are as follows. Figure 2.38 shows the water surface at time $t = 1$ (in the cross-shore direction). It is not constant as the water is flowing up the beach at this time. Figure 2.39 shows the corresponding x-velocity during the wave runup. The velocities should be free from major spikes.

After a much longer time, representatives of the results are as follows. Figure 2.40 shows the water surface at time 30s (in the cross-shore direction). It should be nearly constant (= -0.1m) in the wet portions of the domain. Figure 2.41 shows the corresponding velocity at time 30s. It should be nearly zero (e.g. $<<$ 1 mm/s). This case has been used to illustrate wet-dry artefacts in some versions of ANUGA.

2.11.2 Comment on wet-dry artefacts

Earlier ANUGA algorithms showed some wet-dry artefacts in this scenario, which manifest as a high velocity at the wet/dry interface, and water creeping up the slope (this was a feature of earlier ANUGA algorithms). If the process is handled correctly in ANUGA, water should not "creep-up" to the left for a long distance (the discontinuous elevation + tsunami algorithms should have no problem with this).

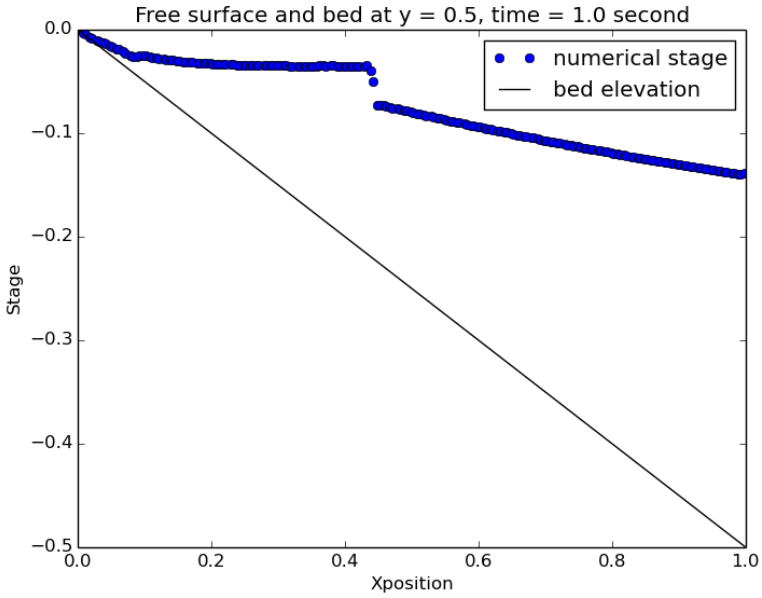

Figure 2.38: Water surface during the wave runup at time $t = 1.0$.

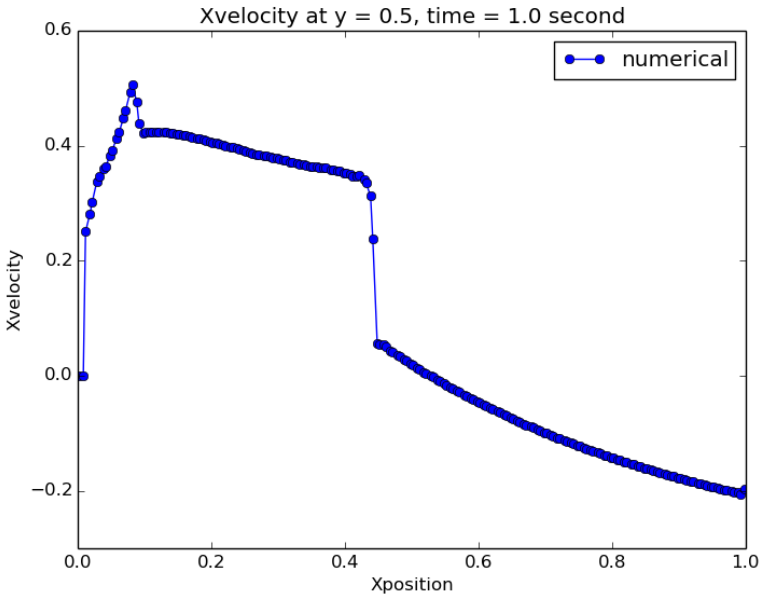

Figure 2.39: Xvelocity during the wave runup at time $t = 1.0$.

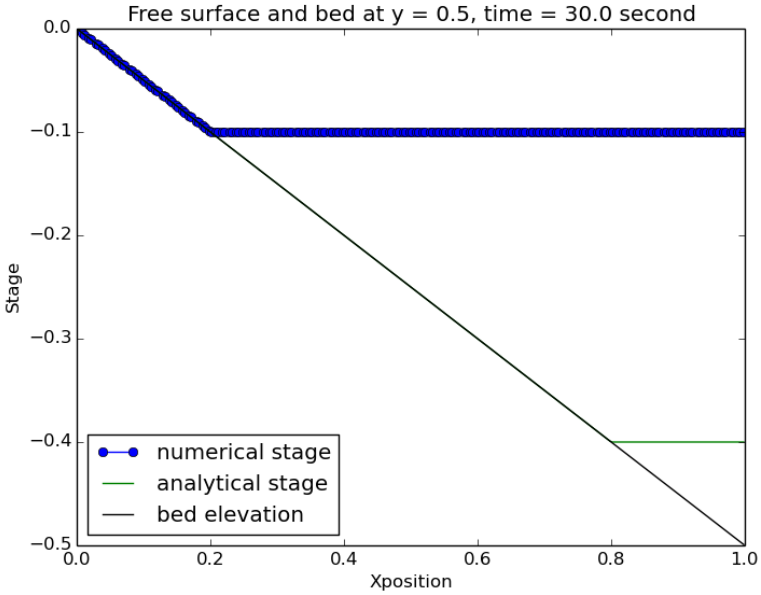

Figure 2.40: Water surface at time 30s after the wave runup. It should be nearly constant in wet parts of the domain.

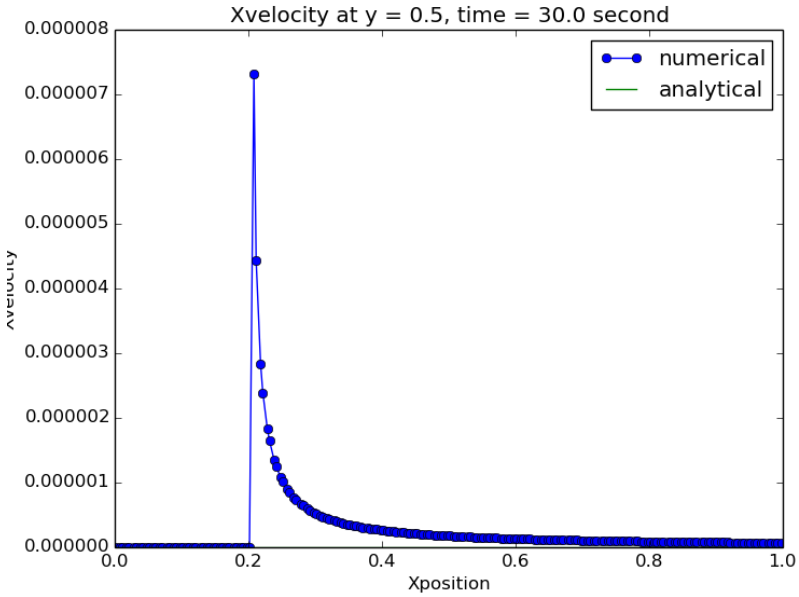

Figure 2.41: Xvelocity at time 30s after the wave runup. It should be nearly zero.

2.12 Wave runup over sinusoidal ridges

This scenario simulates a wave flowing up a beach with skewed sinusoidal ridges. Following the initial wave runup, eventually the water elevation should become constant, and the velocities should approach zero.

2.12.1 Results

Figure 2.42 shows the centroid velocities during the wave runup. The flow should be concentrating in the channels near the shore, and be free from major spikes.

Figure 2.43 shows the velocities profile at time 40 s. They should be nearly zero (e.g. O(10^{-3}) m/s). This case has been used to illustrate wet-dry artefacts in some versions of ANUGA.

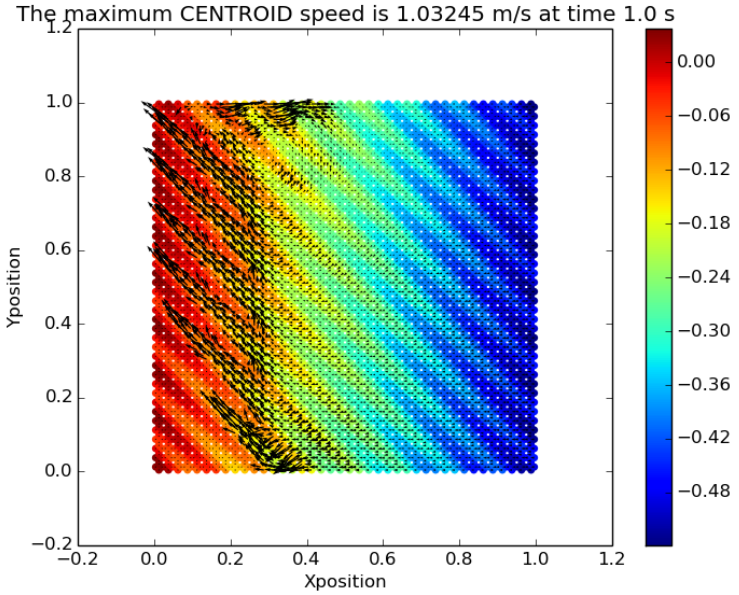

Figure 2.42: Velocity during the wave runup. Point color corresponds to the bed elevation

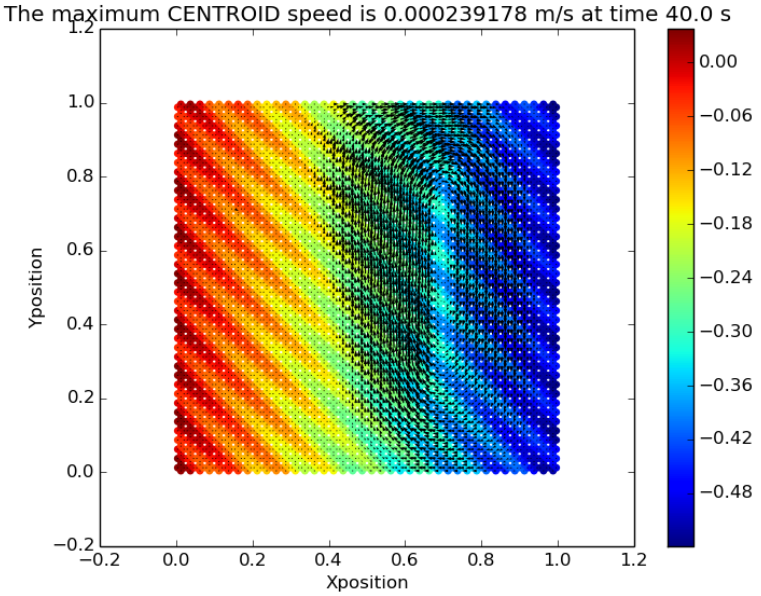

Figure 2.43: Velocity at time 20s after the wave runup. The flow speed should be nearly zero. Point color corresponds to the bed elevation.

2.13 Tsunami Runup Analytical Solution

This test case is 'Benchmark Problem 1' from the 'Third International workshop on long-wave runup models, June 17-18 2004'. It models the runup of an initial waveform on a linearly sloping beach. The analytical solution was produced using the techniques of Carrier, Wu and Yeh [3]. The problem descriptions and solution were sourced from `http://isec.nacse.org/workshop/2004_cornell/bmark1.html`

2.13.1 Results

Figures 2.44-2.45 compare the modelled and analytical stage and velocity at various instances in time, while Figure 2.46 shows the time-evolution of the shoreline position and velocity at the shoreline. For the numerical model, the shoreline position and velocity are defined based on two depth thresholds (see figure titles), as ANUGA does not explicitly track the wet-dry interface. We expect to see good agreement between the analytical and numerical solutions for both stage and velocity over most of the domain. A discrepency near the shoreline can occur in some ANUGA algorithms, particularly in the velocity.

2.13.2 Comment on algorithm-specific performance

At the time of writing (17/05/2013), the 'tsunami' algorithm has a small phase-lag during the runup stage. This is attributed to the extra mass storage in each numerical cell associated with that algorithm, which slightly reduces the rate of inundation. It can be further reduced with mesh refinement. Regardless, the solution quality is quite comparable with results using other solvers on similar sized meshes [4, 22].

The discontinuous elevation algorithms show different artefacts, related to their tendency to have slow drainage in nearly-dry areas (so a very shallow layer of water keeps flowing down-slope even when analytically, the slope should have dried). This will be manifest most obviously in in velocity aftefacts over the nearly-dry slope following draw-down. The amount of water retained on the slope is small, so this is issue is not obvious in the stage plots. However, it does complicate the definition of the wet-dry interface, leading to potentially large discrepencies in the computed velocity at the shoreline and the shoreline location.

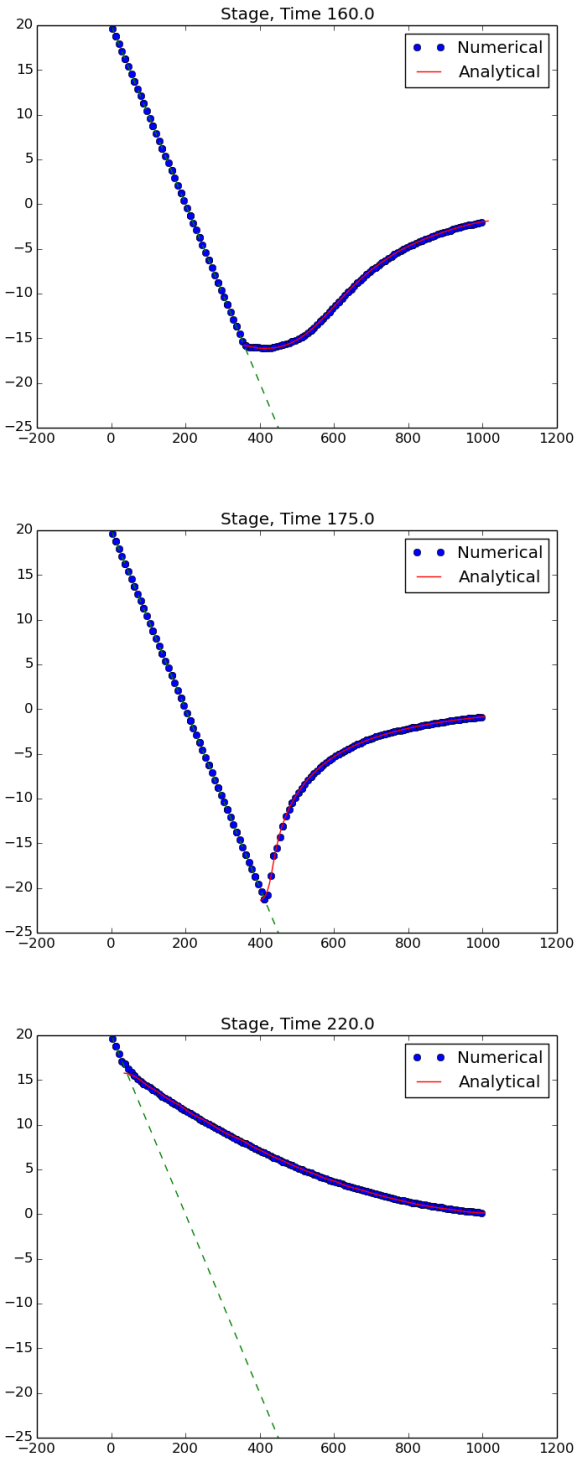

Figure 2.44: Water surface elevation at several instants in time

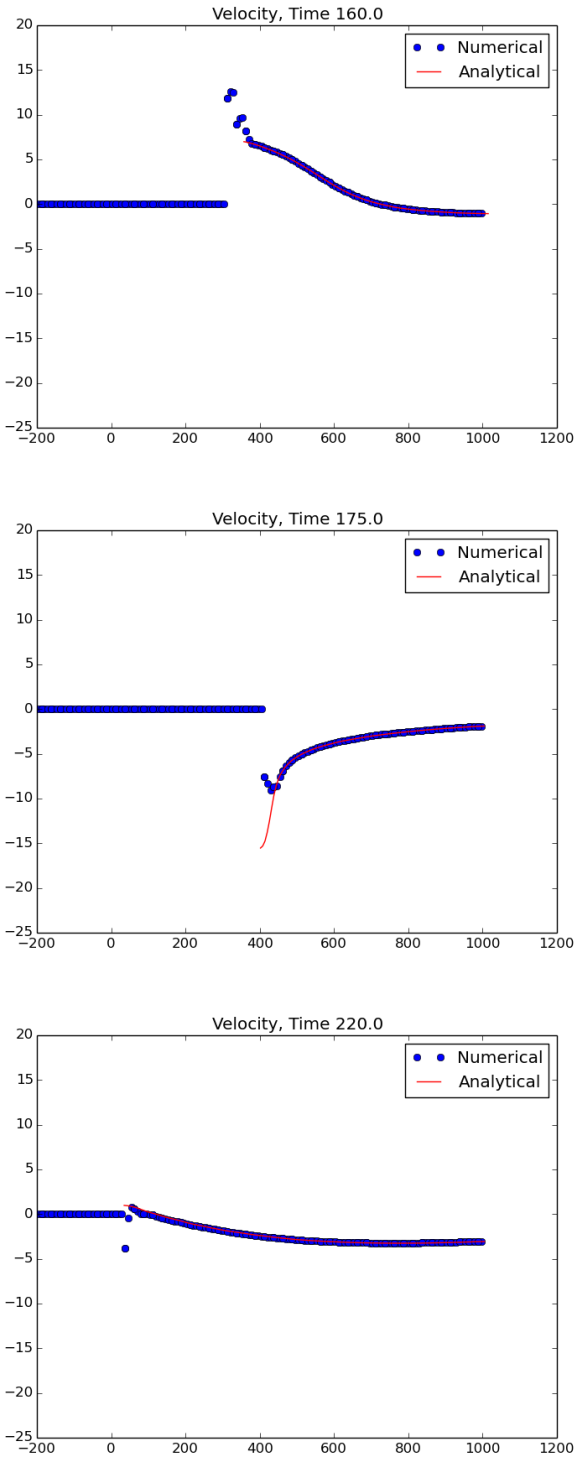

Figure 2.45: Velocity at several instants in time

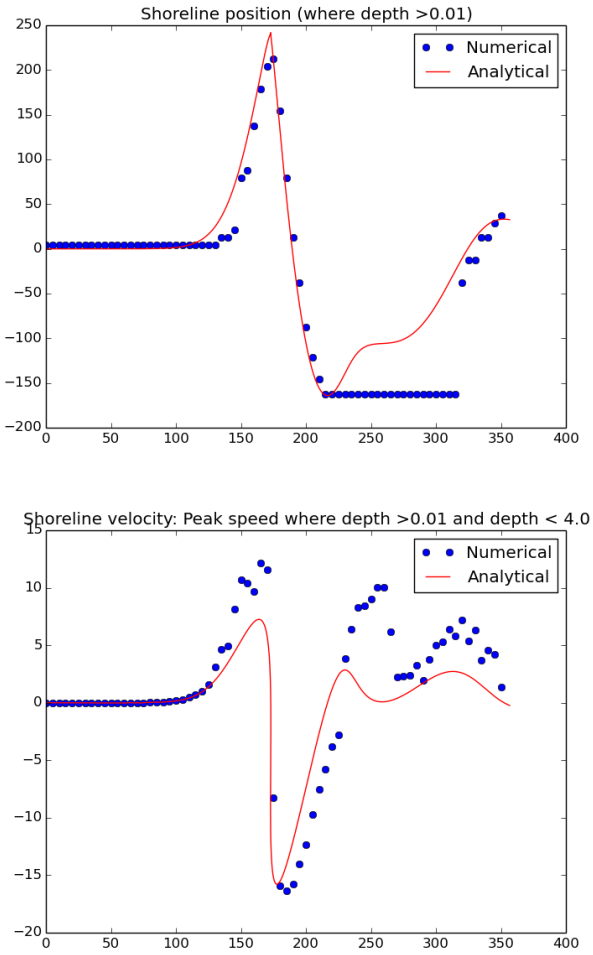

Figure 2.46: Timeseries of shoreline position and velocity

2.14 Lake at rest with an immersed bump

This is a simple test if the method is well-balanced. The initial condition is a lake at rest with water depth 0.5. The topography is

$$z(x) = \begin{cases} 0.2 - 0.05\,(x-10)^2 & \text{if} \quad 8 \le x \le 12\,, \\ 0 & \text{otherwise,} \end{cases} \tag{2.43}$$

The analytical solution is obviously a lake at rest, that is, $w = 0.5$ and $u = v = 0$.

2.14.1 Results

Setting up the boundaries to be reflective, we should see excellent agreement between the analytical and numerical solutions if the method is well-balanced. Some oscillations may occur, but if the method is well-balanced, they should be very close to the order of the machine precision. The following three figures show the stage, x-momentum, and x-velocity after running ANUGA for some time.

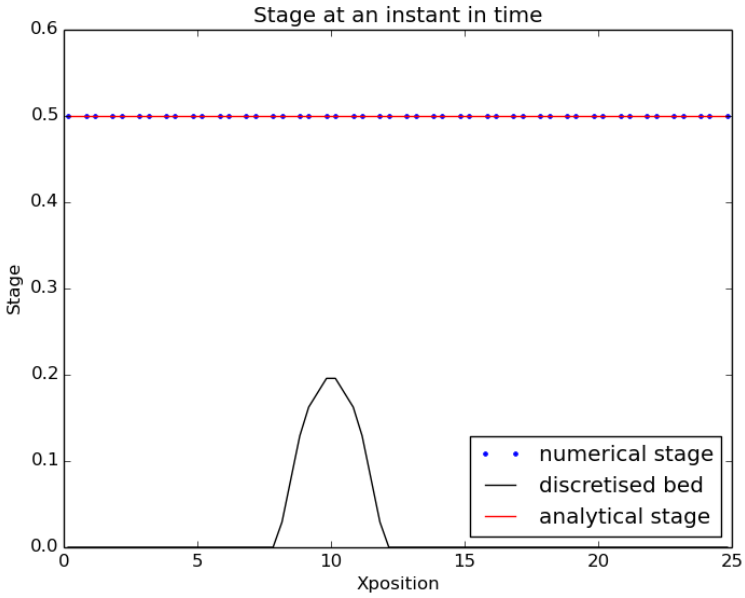

Figure 2.47: Stage results

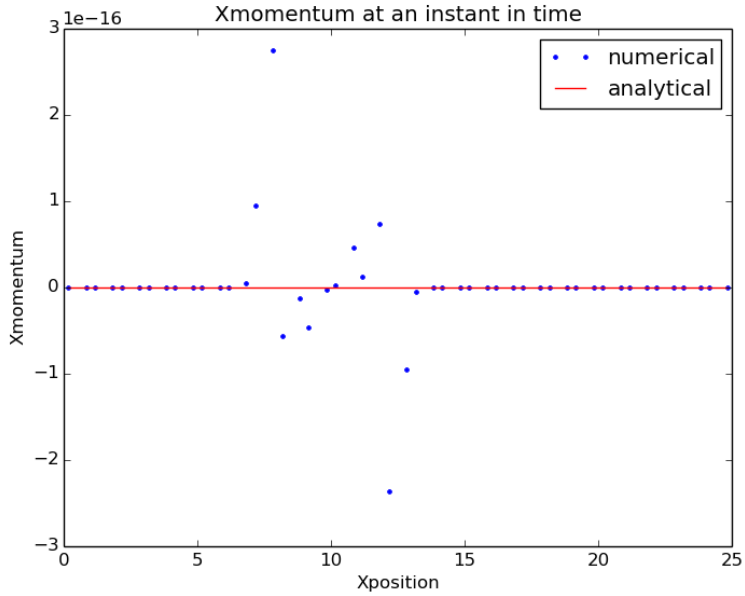

Figure 2.48: Xmomentum results

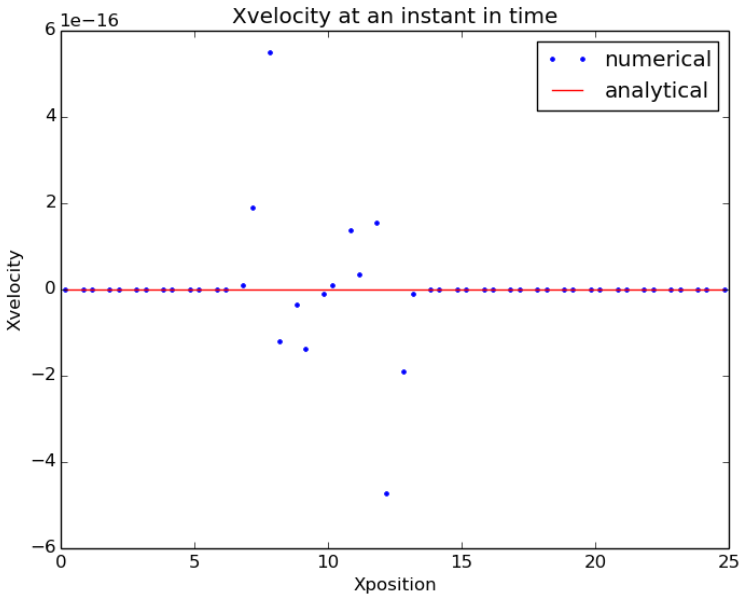

Figure 2.49: Xvelocity results

2.15 Lake at rest with a steep island

This is a test if the method is well-balanced. Furthermore, we test if the wet/dry interface has been correctly treated for a steep island. This test is taken from the work of Mungkasi and Roberts [17].

The initial condition is a lake at rest with water depth 4.5. The topography is

$$z(x,y) = \begin{cases} -0.01(x-200)+4 & \text{if} \quad 0 \le x < 200 \\ -0.02(x-200)+4 & \text{if} \quad 200 \le x < 300 \\ -0.01(x-300)+2 & \text{if} \quad 300 \le x < 400 \\ (-1/75)(x-400)+2 & \text{if} \quad 400 \le x < 550 \\ (1/11250)(x-550)(x-550) & \text{if} \quad 550 \le x < 700 \\ 0.03(x-700) & \text{if} \quad 700 \le x < 800 \\ -0.03(x-800)+3 & \text{if} \quad 800 \le x < 900 \\ 6 & \text{if} \quad 900 \le x < 1000 \\ (-1.0/20000)(x-1000)(x-1400) & \text{if} \quad 1000 \le x < 1400 \\ 0 & \text{if} \quad 1400 \le x < 1500 \\ 3 & \text{if} \quad 1500 \le x < 1700 \\ -0.03(x-1700)+3 & \text{if} \quad 1700 \le x < 1800 \\ (4.5/40000)(x-1800)(x-1800)+2 & \text{otherwise,} \end{cases} \tag{2.44}$$

The analytical solution is the lake at rest, that is, $w = 4.5$ and $u = v = 0$.

2.15.1 Results

Older versions of ANUGA might not handle a discontinuous island well, but newer versions should be exact to numerical precision (including the discontinuous-elevation and tsunami algorithms). The following three figures show the stage, x-momentum, and x-velocity respectively, after we run the simulation for some time. We should see excellent agreement between the analytical and numerical solutions if the method is well-balanced and if the wet/dry interface has been correctly treated. Note the figure scales - momenta will probably be plotted on a scale varying only a tiny range, since the result is zero to numerical precision.

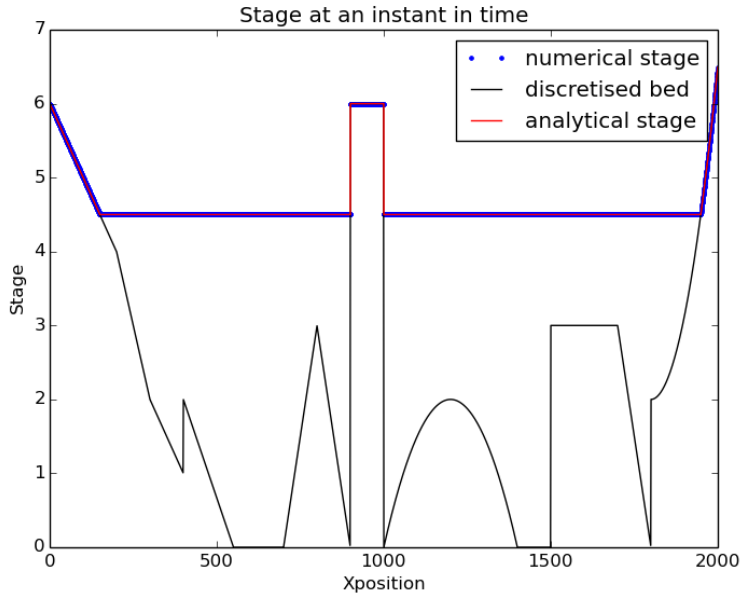

Figure 2.50: Stage results

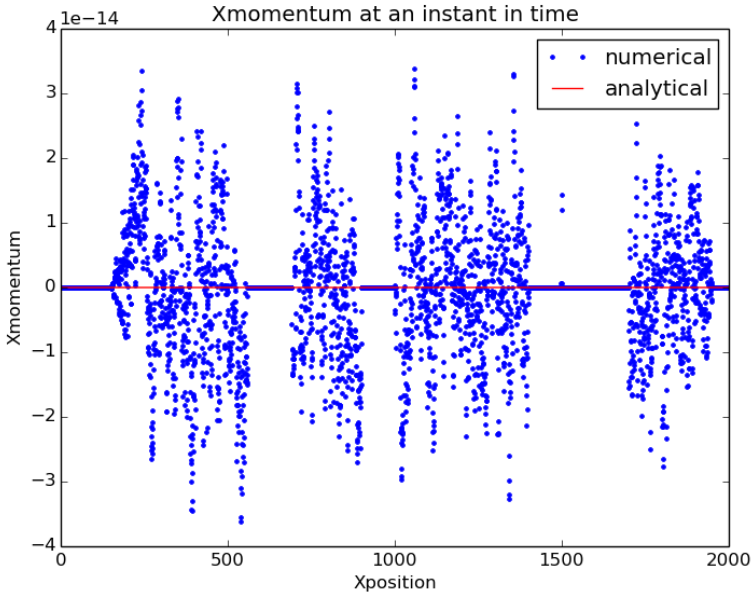

Figure 2.51: Xmomentum results

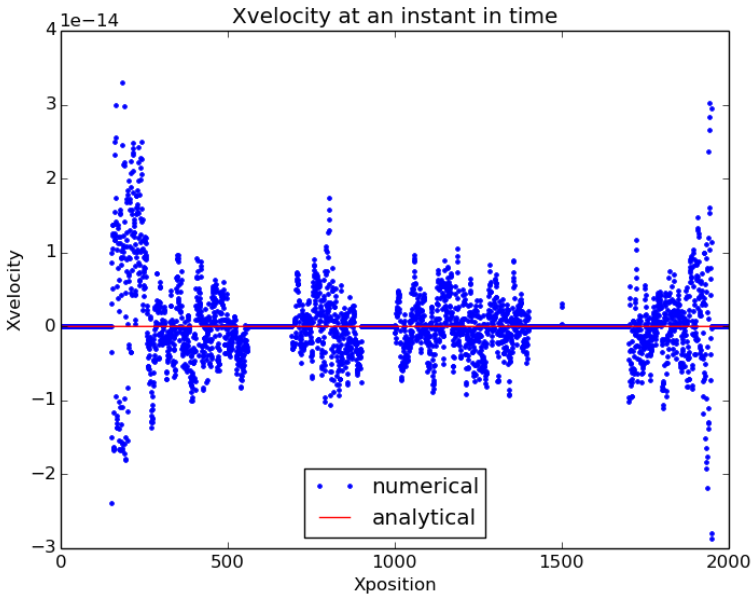

Figure 2.52: Xvelocity results

2.16 River at rest with varying width and topography

This is a test if the method is well-balanced. Furthermore, we test if the wet/dry interface has been correctly treated for steep river banks. This test is taken from the work of Goutal and Maurel [9].

The initial condition is a river at rest with water depth 12.0. Boundary conditions are solid wall. The width and topography of the river are defined as piecewise linear interpolations of the data presented in Table 2.1. The analytical solution is the river at rest, that is, $w = 12.0$ and $u = v = 0$.

2.16.1 Results

Old versions of ANUGA might not treat the wet/dry interface appropriately, but the discontinuous-elevation and tsunami algorithms should do this correctly. The following figures show the stage, x-momentum, and x-velocity respectively, after we run the simulation for some time. The first three show a slice in the x direction (down the river) and the last three figures show a cross section across the river. We should see excellent agreement between the analytical and numerical solutions if the method is well-balanced and if the wet/dry interface has been correctly treated. Note the scale of the figures (since in cases that are accurate to numerical precision, the figure scale will only vary over a tiny range).

Table 2.1: River width and topography (see Goutal and Maurel [9]).

x	topography	width
0	0	40
50	0	40
100	2.5	30
150	5	30
250	5	30
300	3	30
350	5	25
400	5	25
425	7.5	30
435	8	35
450	9	35
470	9	40
475	9	40
500	9.1	40
505	9	45
530	9	45
550	6	50
565	5.5	45
575	5.5	40
600	5	40
650	4	30
700	3	40
750	3	40
800	2.3	5
820	2	40
900	1.2	35
950	0.4	25
1000	0	40
1500	0	40

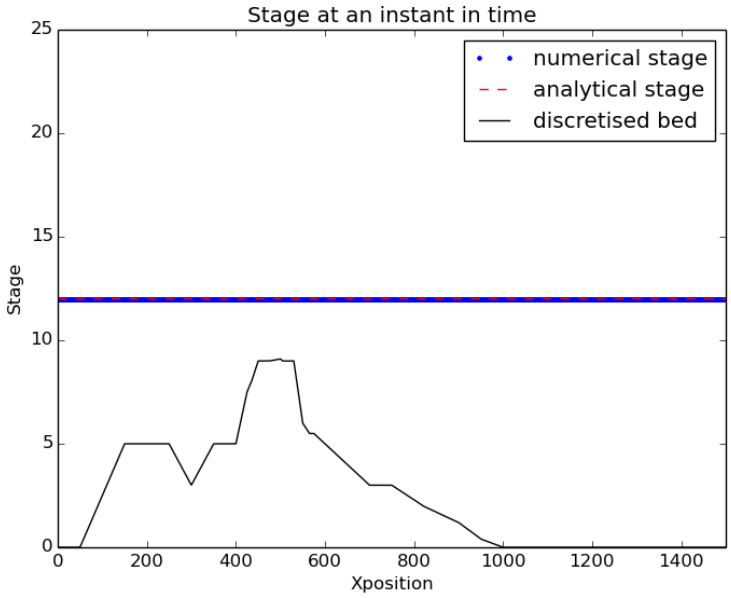

Figure 2.53: Stage results down the river

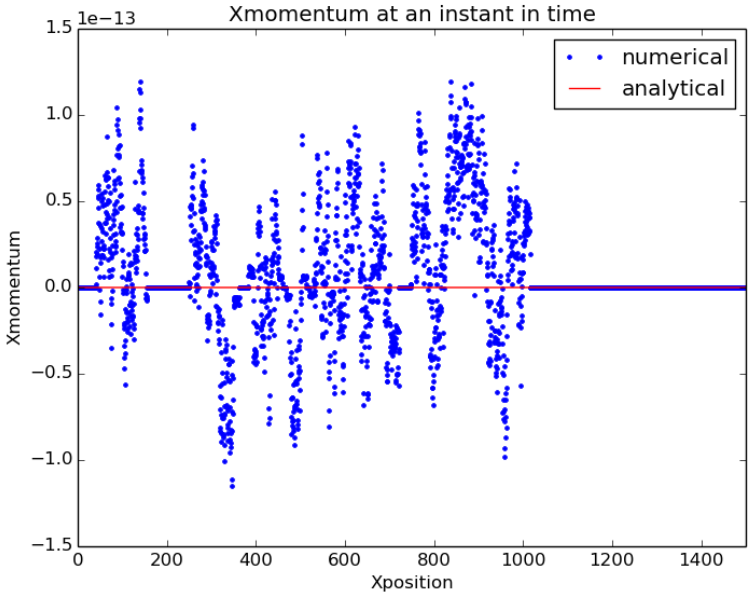

Figure 2.54: Xmomentum results down the river

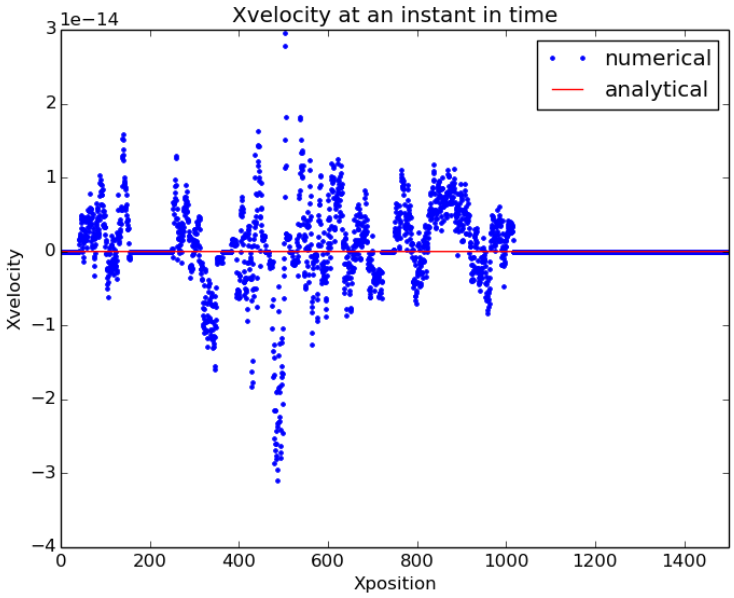

Figure 2.55: Xvelocity results down the river

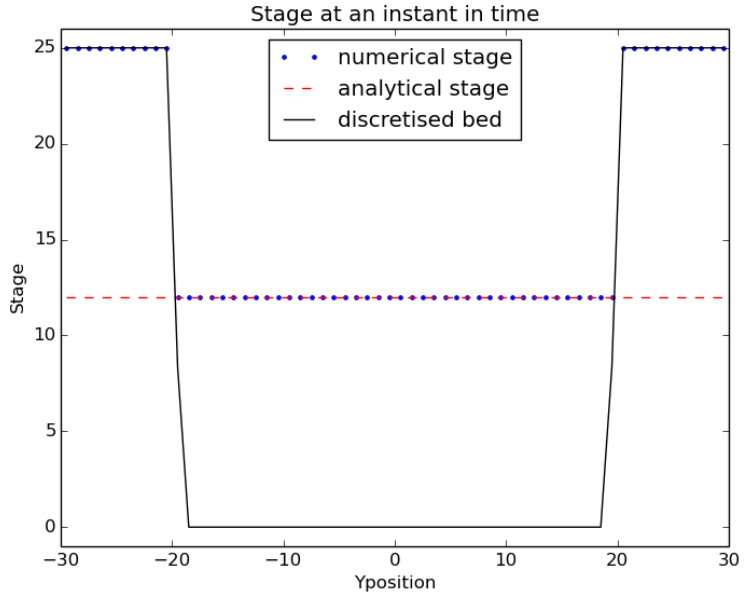

Figure 2.56: Stage results across the river

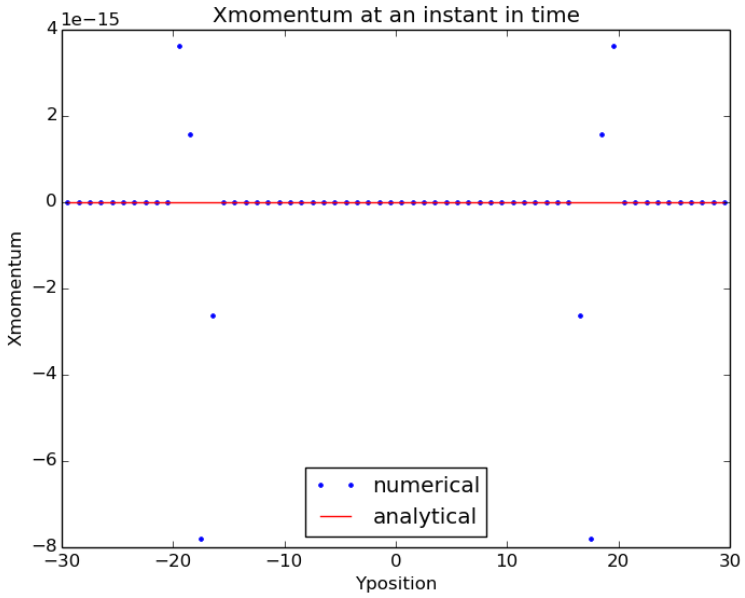

Figure 2.57: Xmomentum results across the river

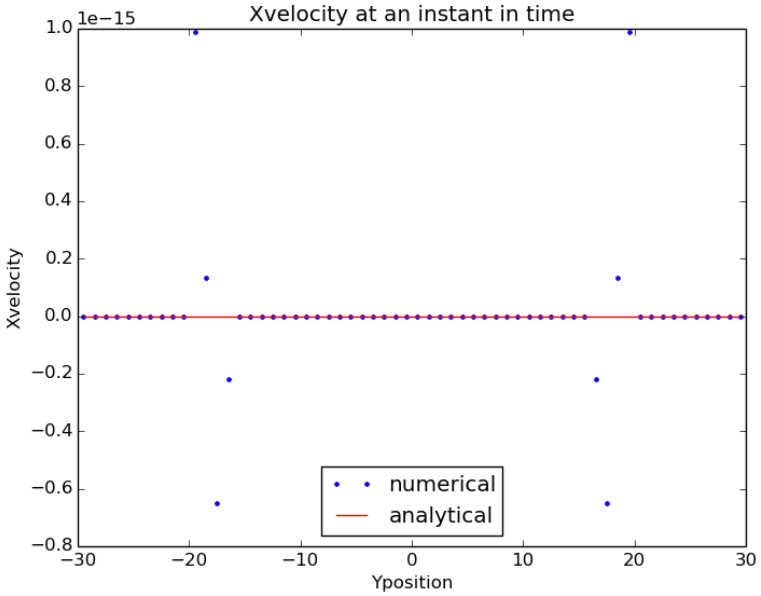

Figure 2.58: Xvelocity results accros the river

2.17 Shallow flow down a mild slope

This case simulates very shallow flow running down a mild slope topography. It represents an idealisation of the rainfall-runoff problem, which will often involve very shallow flows down such a topography. This case has an analytical solution, and in particular, we consider the steady-uniform solution with the values of bed slope and friction slope are the same.

Suppose that we are given a one dimensional domain. The steady state conditions with a contant water depth everywhere make the shallow water equations to the single identity

$$z_x = -S_f, \tag{2.45}$$

where z_x is the bed slope, and S_f is the symbol for the force of bottom friction. We take Manning's friction

$$S_f = n^2 \frac{q|q|}{h^{10/3}} \tag{2.46}$$

where n is the Manning's coefficient and q is the discharge uh. If q, n, and z_x are given, then the analytical solution for u and h is

$$u(x) = \left[-n^{-2} q^{4/3} z_x\right]^{3/10}, \tag{2.47}$$

$$h(x) = \frac{q}{u}\,. \tag{2.48}$$

2.17.1 Results

For our test, we consider a square dimensional domain with length and width 100. We take $q = 0.2$, $n = 0.03$, and $z_x = -0.1$. The topography is

$$z(x, y) = -0.1x\,. \tag{2.49}$$

The initial condition is $u = v = 0$ and

$$w(x, y, 0) = -0.1x + 0.01\,. \tag{2.50}$$

Some simulation results are as follows. Figures 2.63 shows the steady state depth in the downstream direction. There should be a good agreement with the analytical solution, at least away from the boundaries.

Figures 2.65 shows the steady state depth across the slope around the line x = 50m. There should be a good agreement with the analytical solution, at least away from the boundaries.

Figures 2.66 and 2.67 show the steady state x- and y-velocities, along a slice in the cross slope direction (near $x = 50$). The x-velocities should agree well with the analytical solution, and the y-velocities should be zero.

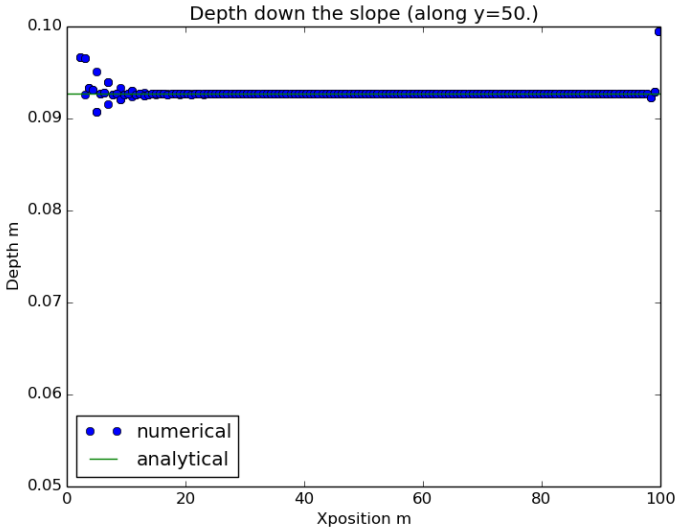

Figure 2.59: Depth in the downstream direction

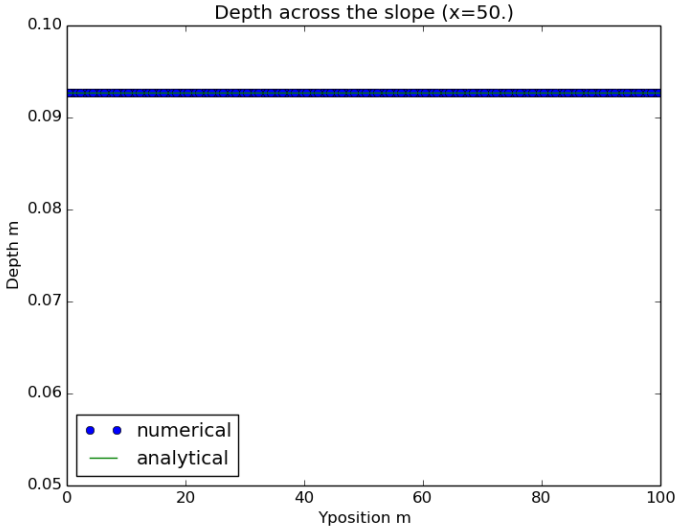

Figure 2.60: Depth across the slope around $x = 50$m

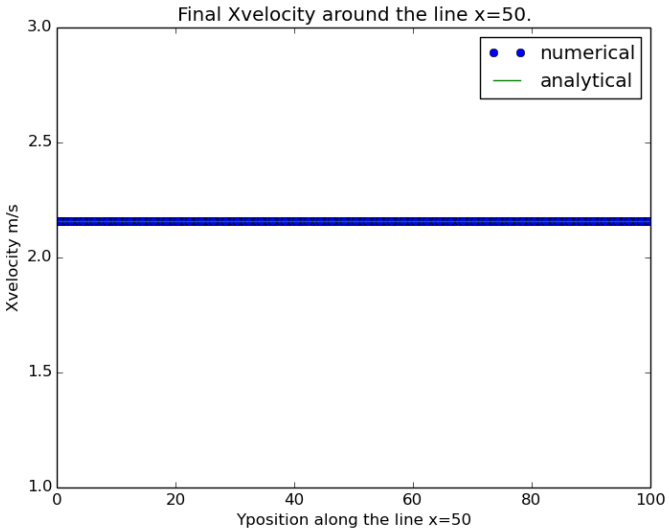

Figure 2.61: x-velocity along the cross-section $x = 50$ (i.e. a cross-section with constant bed elevation)

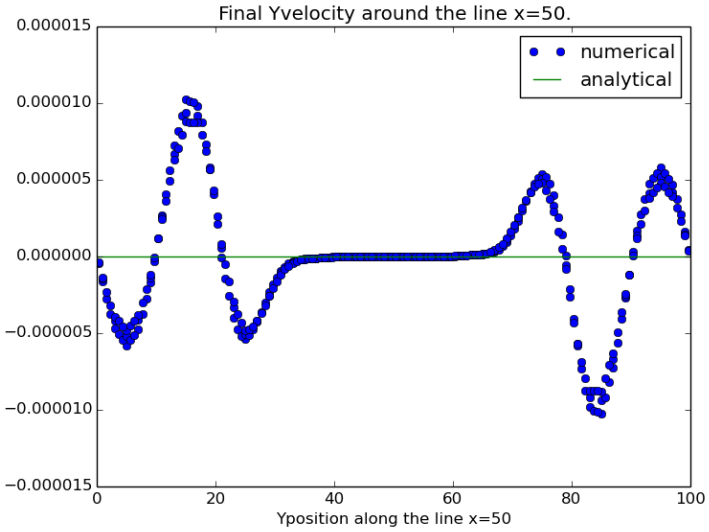

Figure 2.62: y-velocity along the cross-section $x = 50$ (i.e. a cross-section with constant bed elevation)

2.18 Shallow flow down a mild slope with coarsely resolved topography

This case simulates very shallow flow running down a mild slope, with coarsely resolved topography, and a very low discharge. It represents a numerically more challenging idealisation of the rainfall-runoff problem, as compared to the case with higher discharge and resolution. This case has an analytical solution, and in particular, we consider the steady-uniform solution with the values of bed slope and friction slope are the same.

Suppose that we are given a one dimensional domain. The steady state conditions with a contant water depth everywhere make the shallow water equations to the single identity

$$z_x = -S_f. \tag{2.51}$$

Here $q = uh$ is the momentum or water discharge and S_f is the symbol for the force of bottom friction involving Manning's coefficient n. We take

$$S_f = n^2 \frac{q|q|}{h^{10/3}}. \tag{2.52}$$

If q, n, and z_x are given, then the analytical solution is

$$u(x) = \left[-n^{-2} q^{4/3} z_x\right]^{3/10}, \tag{2.53}$$

$$h(x) = \frac{q}{u}. \tag{2.54}$$

2.18.1 Results

For our test, we consider a square dimensional domain with length and width 100. We take $q = 1/1000.$, $n = 0.03$, and $z_x = -0.1$. The topography is

$$z(x, y) = -0.1x. \tag{2.55}$$

The initial condition is $u = v = 0$ and

$$w(x, y, 0) = -0.1x + 0.01. \tag{2.56}$$

Some simulation results are as follows. Figures 2.63 shows the steady state depth in the downstream direction. There should be a good agreement with the analytical solution in the middle of the domain (the boundaries will not reach steady-uniform flow). Figures 2.66 and 2.67 show the steady state x- and y-velocities, along a slice in the cross slope direction (near $x = 50$). In the middle of the domain the x-velocities should agree well with the analytical solution, and the y-velocities should be zero.

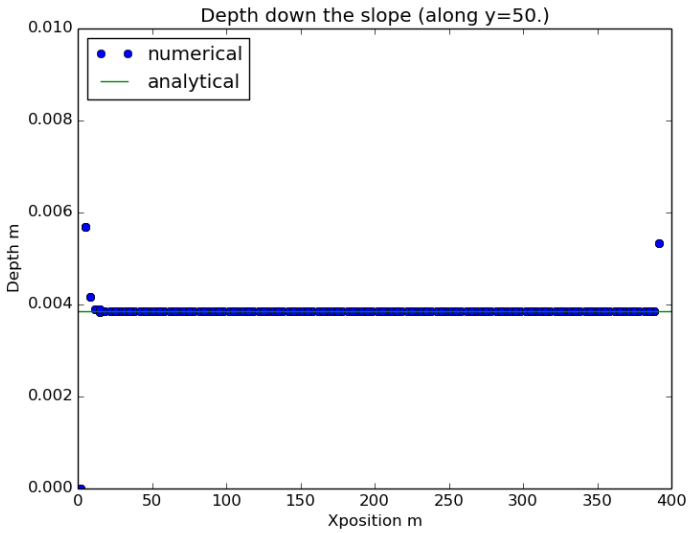

Figure 2.63: Depth in the downstream direction

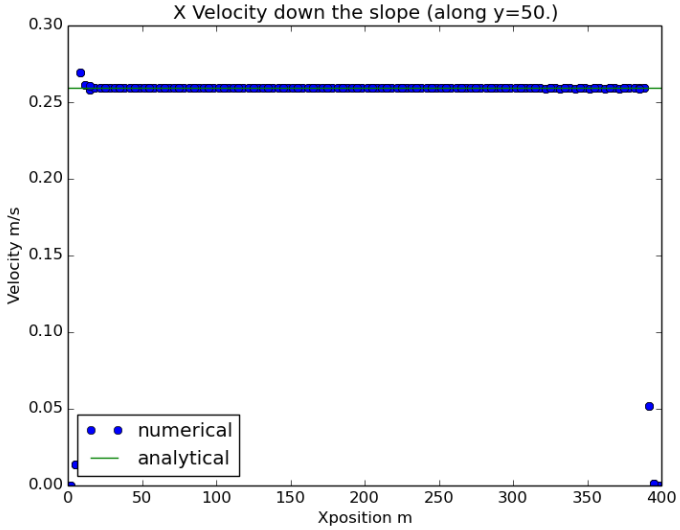

Figure 2.64: X velocity in the downstream direction

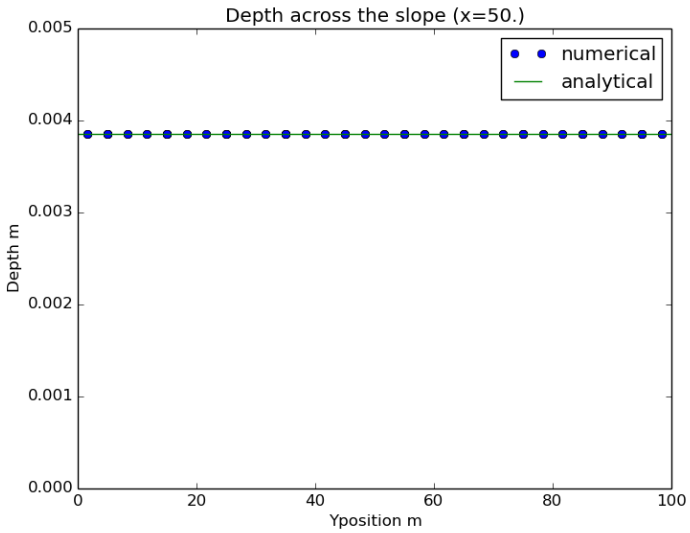

Figure 2.65: Depth in the downstream direction

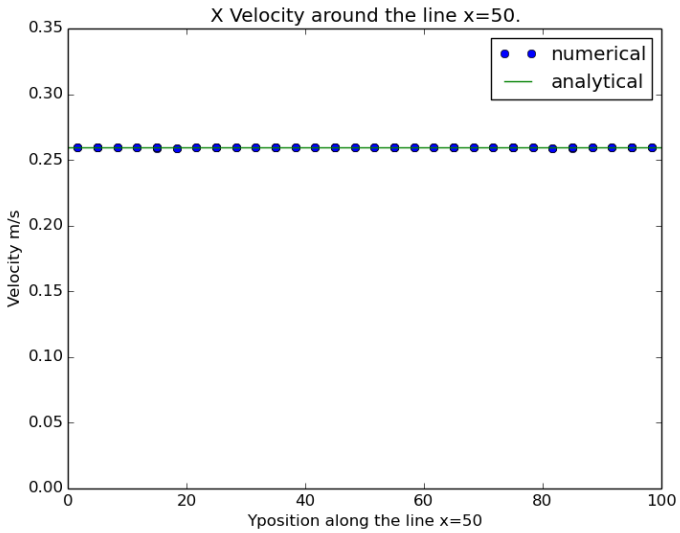

Figure 2.66: x-velocity along the cross-section $x = 50$ (i.e. a cross-section with constant bed elevation)

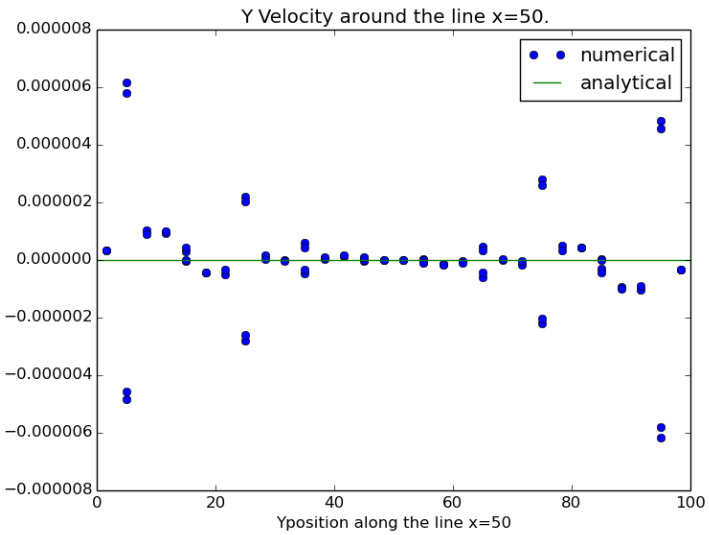

Figure 2.67: y-velocity along the cross-section $x = 50$ (i.e. a cross-section with constant bed elevation)

2.19 Subcritical flow without a shock over a bump

This is a subcritical flow over a bump. This test is adapted from Goutal and Maurel [9]. No shock occurs in this scenario.

Consider a one dimensional domain $[0, 25]$ with topography

$$z(x) = \begin{cases} 0.2 - 0.05\,(x-10)^2 & \text{if} \quad 8 \le x \le 12\,, \\ 0 & \text{otherwise}\,, \end{cases} \tag{2.57}$$

together with Dirichlet boundary conditions. Physically, the boundary conditions mean that there is a source of flow upstream at the point $x = 0^-$ and at the same time there exists a sink of flow downstream at the point $x = 25^+$.

The analytical height is found by solving the Bernoulli equation. The simplified Bernoulli equation is the following cubic equation

$$h^3 + \left(z - \frac{q^2}{2gH^2} - H \right) h^2 + \frac{q^2}{2g} = 0\,, \tag{2.58}$$

where H is the upstream height and $q = uh$ is the discharge or x-momentum. When the height h has been found, the velocity is computed as $u = q/h$.

2.19.1 Results

For our test we consider the initial condition

$$u(x, y, 0) = v(x, y, 0) = 0\,, \quad w(x, y, 0) = 0.2\,, \tag{2.59}$$

and the Dirichlet boundary conditions at $x = 0^-$ and 25^+ to be

$$[w, hu, hv] = [2, 4.42, 0]\,. \tag{2.60}$$

Representatives of the simulation results are given in the following three figures. Even though we have small discrepancy in the numerical and analytical momenta, these numerical an analytical solutions should agree quite well. Note the vertical scale of the plots (matplotlib may offset the vertical scale, check top-left of figures).

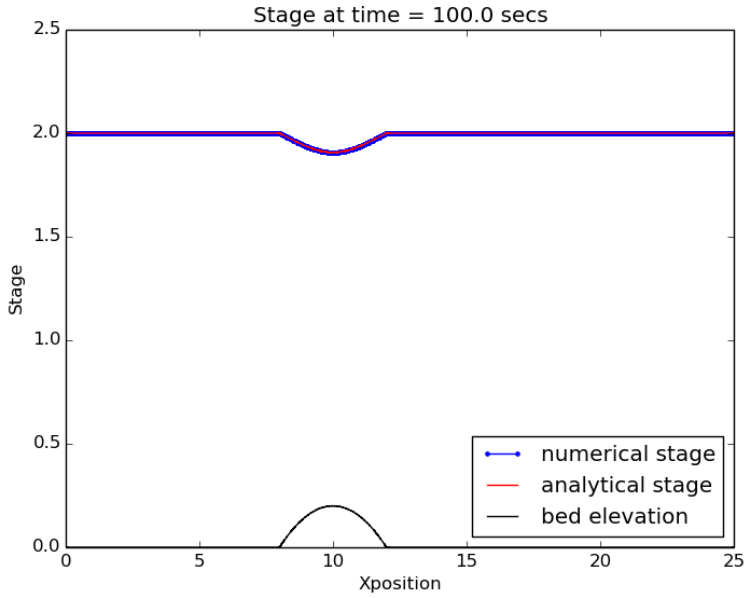

Figure 2.68: Stage results

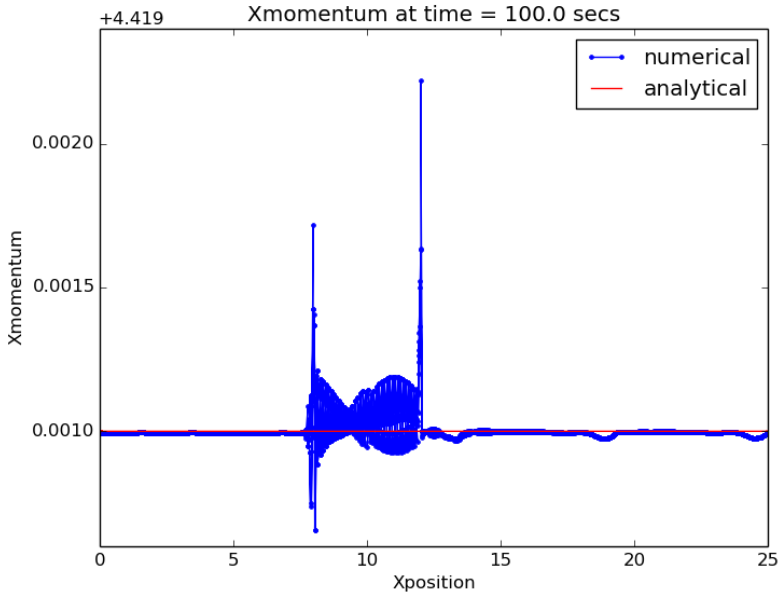

Figure 2.69: Xmomentum results

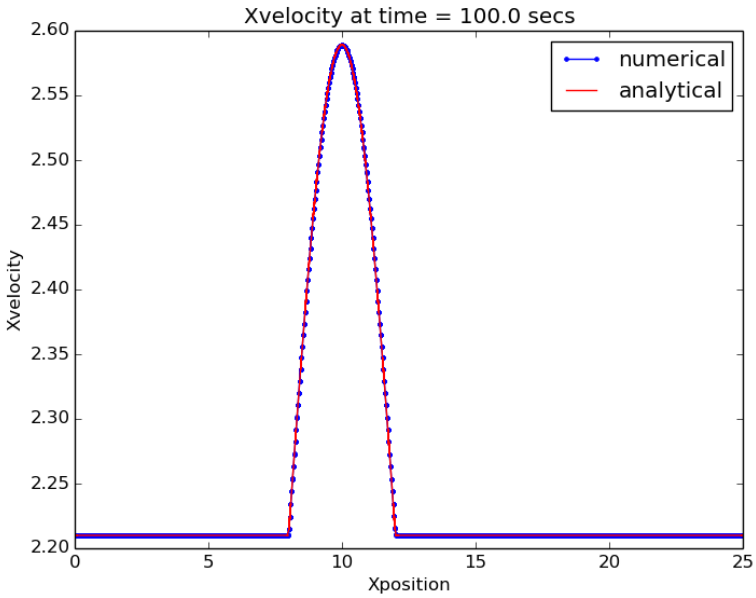

Figure 2.70: Xvelocity results

2.20 Constant Subcritical flow

This is a very simple test of constant (subcritical) flow down a channel. The constant state should be preserved.

2.20.1 Results

For our test we consider the initial condition

$$u(x, y, 0) = v(x, y, 0) = 0\,, \quad w(x, y, 0) = 1.5\,, \tag{2.61}$$

and the Dirichlet boundary conditions at $x = 0^-$ and 25^+ to be

$$[w, hu, hv] = [2, 4.42, 0]\,. \tag{2.62}$$

Representatives of the simulation results are given in the following three figures. We should see a very accurate reproduction of the steady flow $w = 2$ $u = 2.21$, $q = 4.42$ by 20secs.

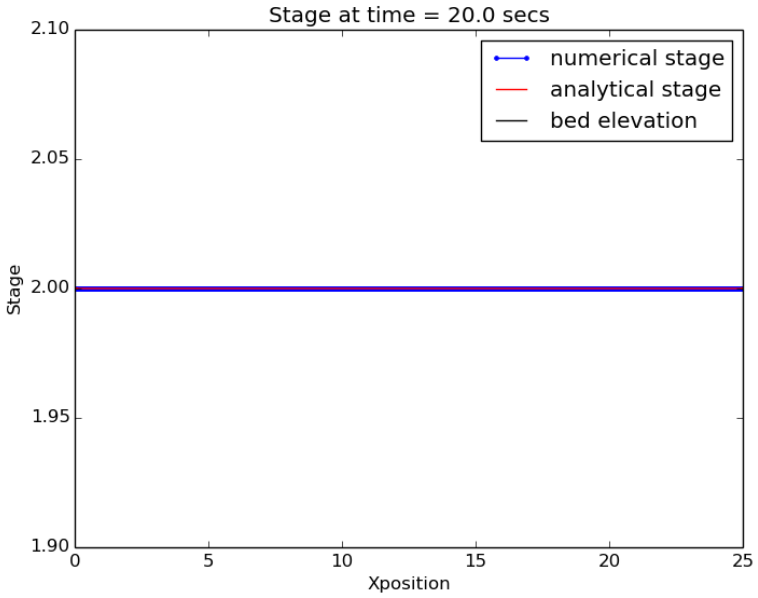

Figure 2.71: Stage results

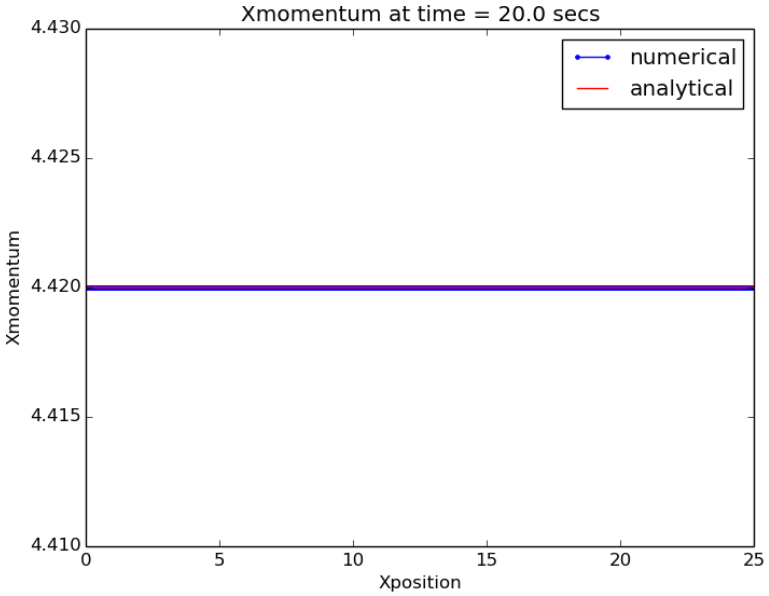

Figure 2.72: Xmomentum results

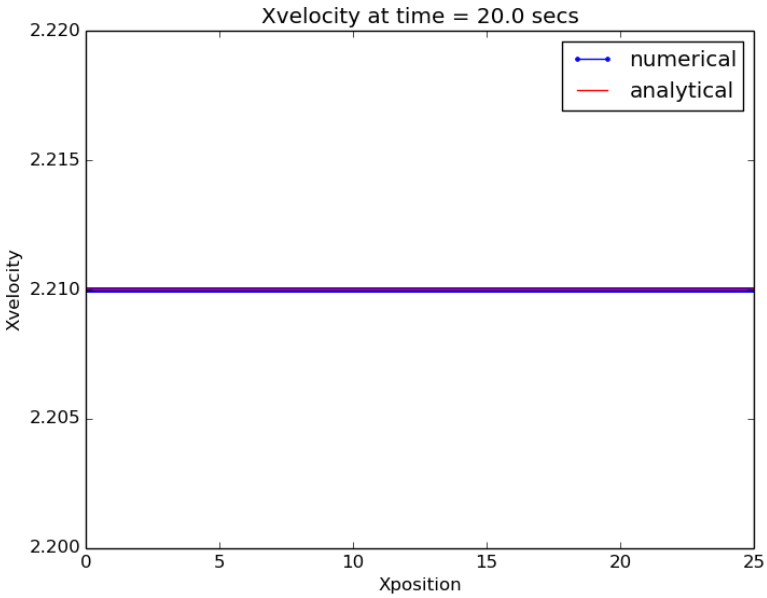

Figure 2.73: Xvelocity results

2.21 Transcritical flow with a shock over a bump

This scenario simulates a transcritical flow over a bump with a shock. The topography and the initial conditions are the same as those used in the subcritical flow (See the description given in the report on the subcritical flow test). However, to get a transcritical flow, the boundary conditions are different from those used in the subcritical flow test. Here we refer to the parameters used by Goutal and Maurel [9].

Referring to our description for the subcritical flow test, the analytical height or depth h of the transcritical flow at smooth regions is found by solving the Bernoulli equation. The analytical solution for the shock position is found by implementing three equations, namely, (a) the Bernoulli equation at upstream (on the left of the shock), (b) the Bernoulli equation at downstream (on the right of the shock), and (c) the Rankine-Hugoniot relation. The Rankine-Hugoniot relation for the steady flow can be expressed as

$$q^2 \left(\frac{1}{h_1} - \frac{1}{h_2} \right) + \frac{g}{2} \left(h_1^2 - h_2^2 \right) = 0 \,, \tag{2.63}$$

where q is the discharge or momentum, h_1 is the height upstream (on the left of the shock), and h_2 is the height downstream (on the right of the shock). When the height h has been found, the velocity is computed as $u = q/h$.

2.21.1 Results

For our simulation, we consider Dirichlet boundary conditions at $x = 0^-$ given by

$$[w, hu, hv] = [0.41373588752426715, \quad 0.18, \quad 0] \,, \tag{2.64}$$

and at 25^+ given by

$$[w, hu, hv] = [0.33, \quad 0.18, \quad 0] \,. \tag{2.65}$$

With these conditions, representatives of the simulation results are shown in the following three figures. They show the stage, x-momentum, and x-velocity respectively. We should see good agreement between the analytical and numerical solutions.

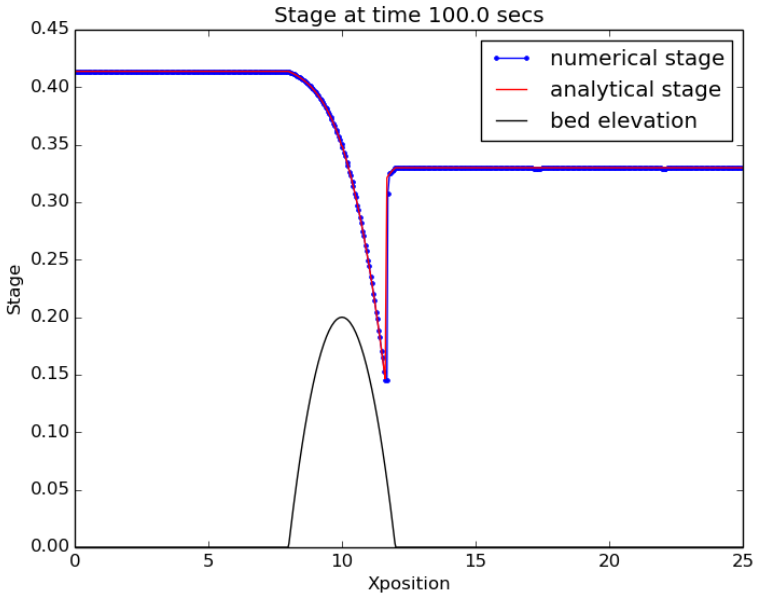

Figure 2.74: Stage results

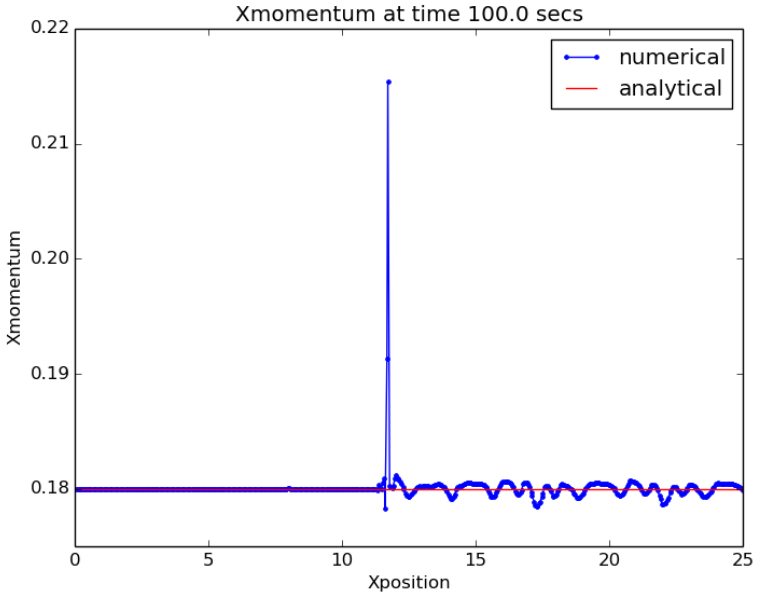

Figure 2.75: Xmomentum results

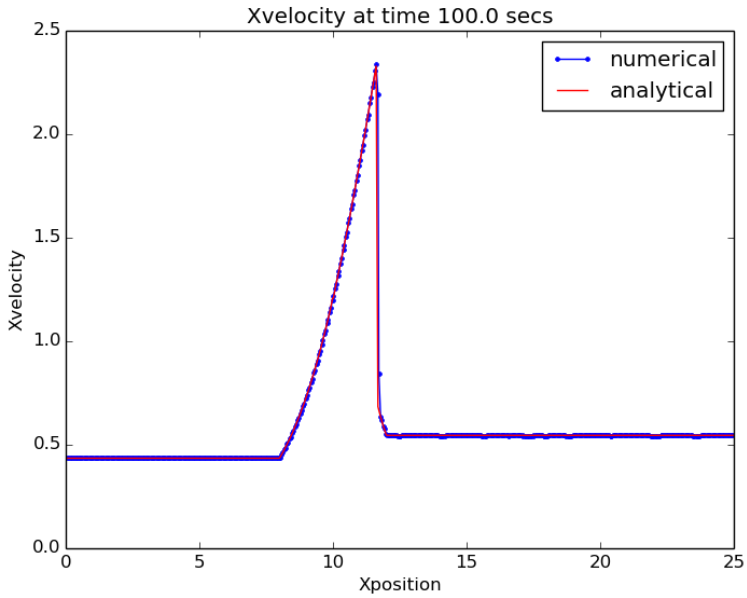

Figure 2.76: Xvelocity results

2.22 Transcritical flow without a shock over a bump

This scenario exhibits transcritical flow without a shock over a bump. This test is adapted from Goutal and Maurel [9]. The topography and the initial conditions are the same as those used in the subcritical flow as well as the transcritical flow with a shock (See the description given in the report on the subcritical flow and transcritical flow with a shock). The boundary conditions are different from those used in the subcritical flow test. Here we refer to the parameters used by Goutal and Maurel [9]. The analytical height or depth h of the transcritical flow is calculated the Bernoulli equation. The velocity is computed as $u = q/h$.

2.22.1 Results

Referring to Goutal and Maurel [9], we consider the initial condition

$$u(x, y, 0) = v(x, y, 0) = 0\,, \quad w(x, y, 0) = 0.66\,, \tag{2.66}$$

We enforce Dirichlet boundary conditions at $x = 0^-$ given by

$$[w, hu, hv] = [1.0144468506259066, \quad 1.53, \quad 0]\,, \tag{2.67}$$

and at 25^+ given by

$$[w, hu, hv] = [0.4057809296474606, \quad 1.53, \quad 0]\,. \tag{2.68}$$

Representatives of the simulation results are given in the following three figures. We should see excellent agreement between the analytical and numerical solutions. Small discrepancy may occurs for the x-momentum. It is not clear what makes this discrepancy. Numerical analysis may be conducted further to investigate why this discrepancy occurs.

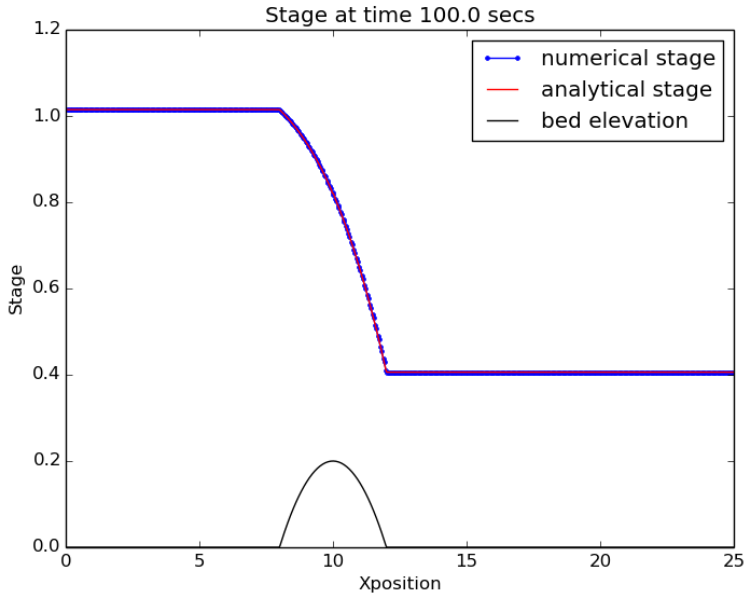

Figure 2.77: Stage results

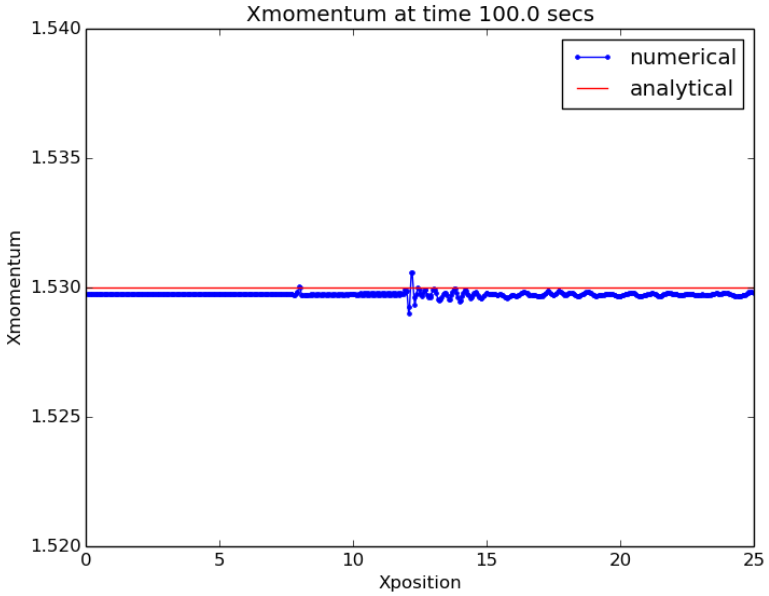

Figure 2.78: Xmomentum results

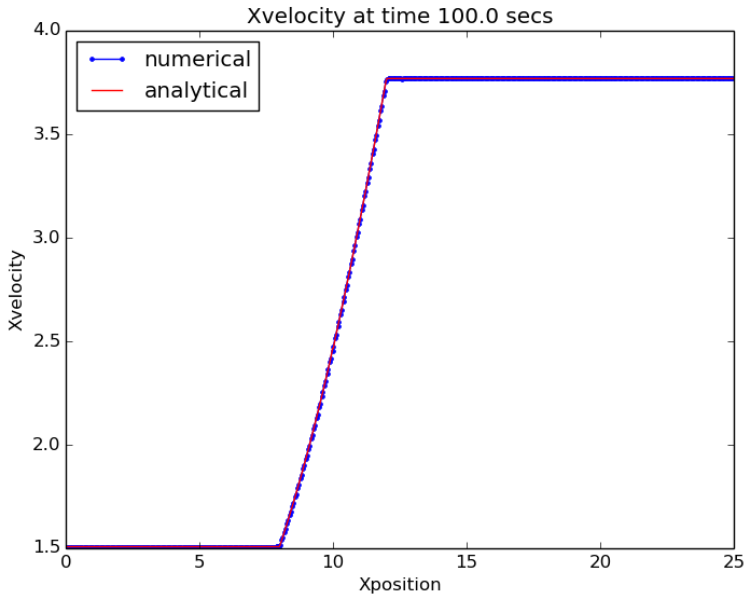

Figure 2.79: Xvelocity results

2.23 Supercritical flow without a shock over a bump

This is a supercritical flow over a bump. This test is adapted from Goutal and Maurel [9]. No shock occurs in this scenario.

Consider a one dimensional domain $[0, 25]$ with topography

$$z(x) = \begin{cases} 0.2 - 0.05\,(x-10)^2 & \text{if} \quad 8 \le x \le 12\,, \\ 0 & \text{otherwise}\,, \end{cases} \tag{2.69}$$

together with Dirichlet boundary conditions. Physically, the boundary conditions mean that there is a source of flow upstream at the point $x = 0^-$ and at the same time there exists a sink of flow downstream at the point $x = 25^+$.

The analytical height is found by solving the Bernoulli equation. The simplified Bernoulli equation is the following cubic equation

$$h^3 + \left(z - \frac{q^2}{2gH^2} - H \right) h^2 + \frac{q^2}{2g} = 0\,, \tag{2.70}$$

where H is the upstream height and $q = uh$ is the discharge or x-momentum. When the height h has been found, the velocity is computed as $u = q/h$.

2.23.1 Results

For our test we consider the initial condition

$$u(x, y, 0) = v(x, y, 0) = 0\,, \quad w(x, y, 0) = 2\,, \tag{2.71}$$

and the Dirichlet boundary conditions at $x = 0^-$ and 25^+ to be

$$[w, hu, hv] = [0.5, 10., 0]\,. \tag{2.72}$$

Representatives of the simulation results are given in the following three figures. Even though we have small discrepancy in the numerical and analytical momenta, these numerical an analytical solutions should agree quite well.

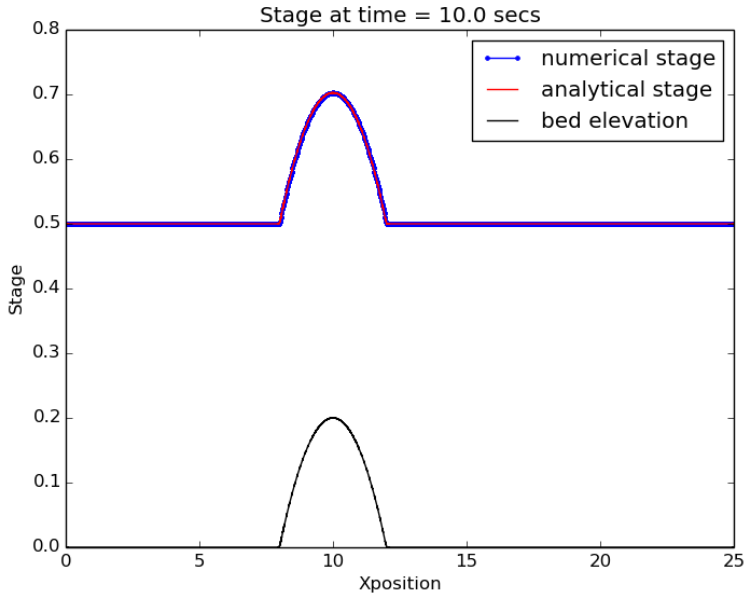

Figure 2.80: Stage results

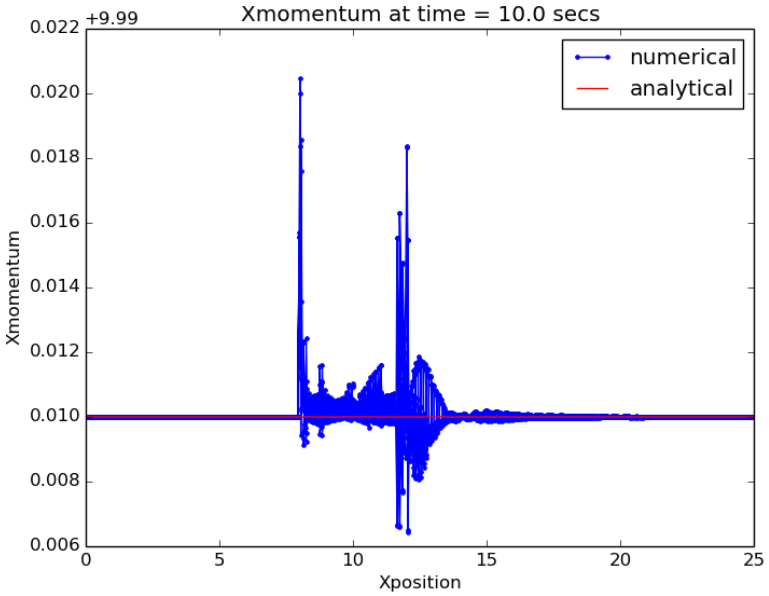

Figure 2.81: Xmomentum results

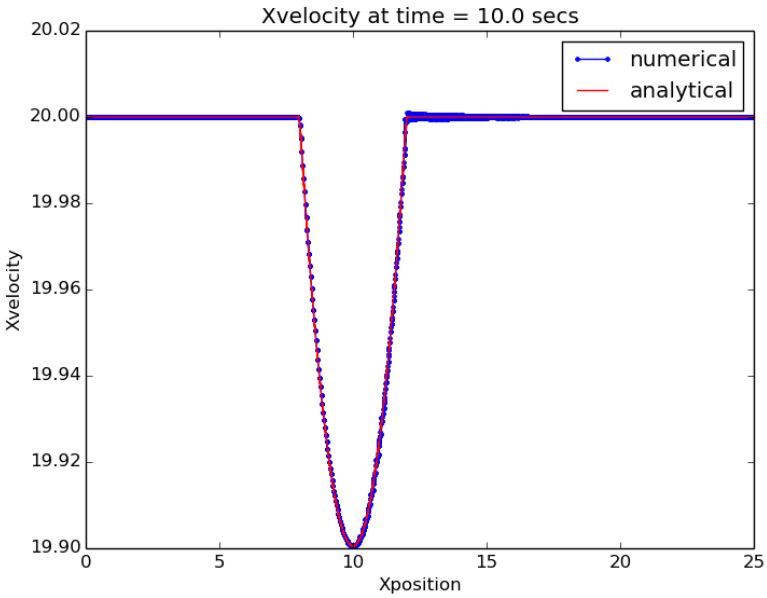

Figure 2.82: Xvelocity results

2.24 Trapezoidal channel steady uniform flow case

This scenario simulates steady, uniform flow in a trapezoidal channel. It tests the ability of the model to compute the correct flow depth, and the correct lateral distribution of flow velocity, and to conserve mass.

2.24.1 Results

Figure 2.83 shows the along-channel depth and velocity (in the deepest part of the channel). Both should be nearly constant away from the boundaries, and be close to the analytical solutions.

We do not expect perfect agreement, because the mesh is not very fine in this example (triangle side length of around 1m, just enough to resolve the banks). There will probably be some numerical diffusion in the cross-channel velocity profiles, which will in turn cause errors in the mid-channel velocity and free surface elevation. We deliberately choose to not use a finer mesh, because in realistic problems, it is often not possible to resolve all channels very well.

Figure 2.84 shows the cross-channel velocity profiles at a number of cross-sections. Ideally it should agree with the analytical solution, however, this may be difficult due to numerical diffusion in the cross-channel direction. Irrespective, the velocity profile should be qualitatively correct – highest velocities should be in the channel centre, with lower velocities towards the banks.

Figure 2.85 show the hydrographs through various cross sections showing the flows limiting to the expected inflow Q (For coarser grids there is a discrepency between the expected and calculated limiting hydrograph due to the error in back-calculating the hydrograph from ANUGA outputs - although in ANUGAs internal computations the discharge is correct). It is also noted that the transient flow is quite different for different grid sizes. We theorize that the coarser grids produce a rougher bed which slows down the flow.

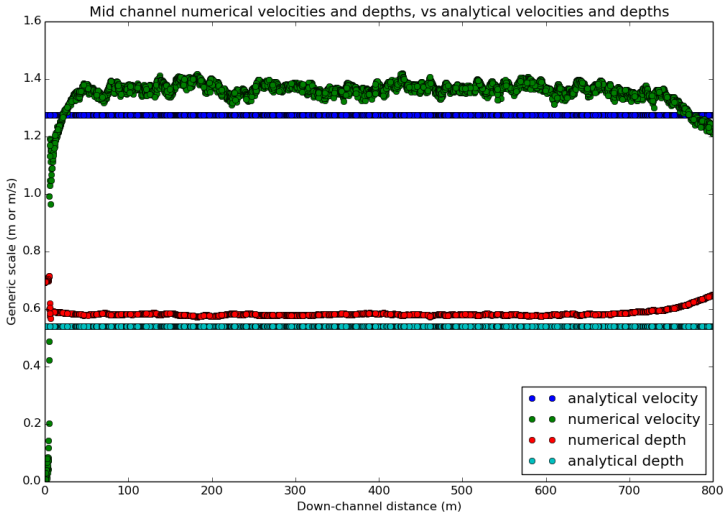

Figure 2.83: Depth and y-velocity in the middle of the channel, in the downstream direction.

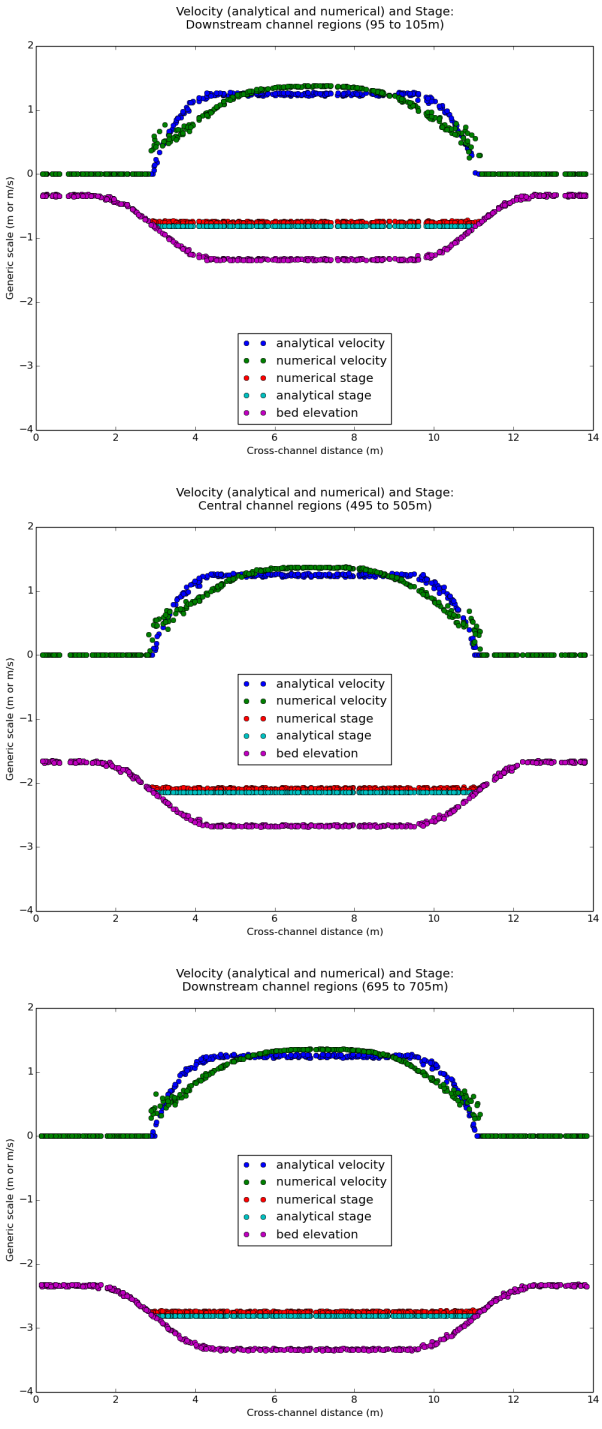

Figure 2.84: y-velocity distribution over a number of cross-sections.

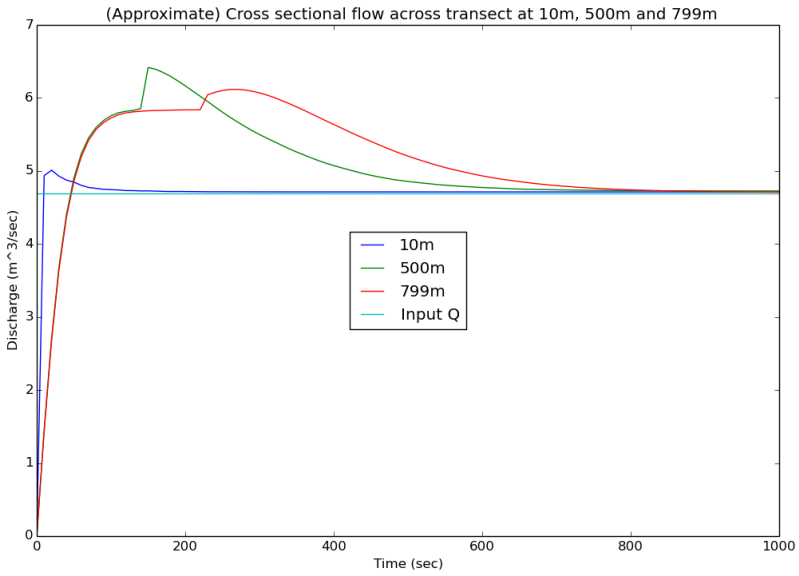

Figure 2.85: Hydrographs over a number of cross-sections.

Chapter 3

Tests against reference data or solutions

3.1 The Yeh–Petroff dam break problem

Yeh and Petroff of the University of Washington conducted experimental dam break with an obstruction column, as shown in Figure 3.1. The Yeh–Petroff dam break problem was further simulated by Gomez-Gesteira and Dalrymple [8] and Silvester and Cleary [26]. A similar problem was studied by Arnason et al. [1]. We shall compare our ANUGA solution to the experimental data of Yeh and Petroff.

3.1.1 Results

We should see broad agreement between the experimental data and the numerical solution. Some disagreement is expected because the flows in this experimental situation show fairly rapid spatial and temporal variations, which are to some extent outside the domain of the shallow water approximation.

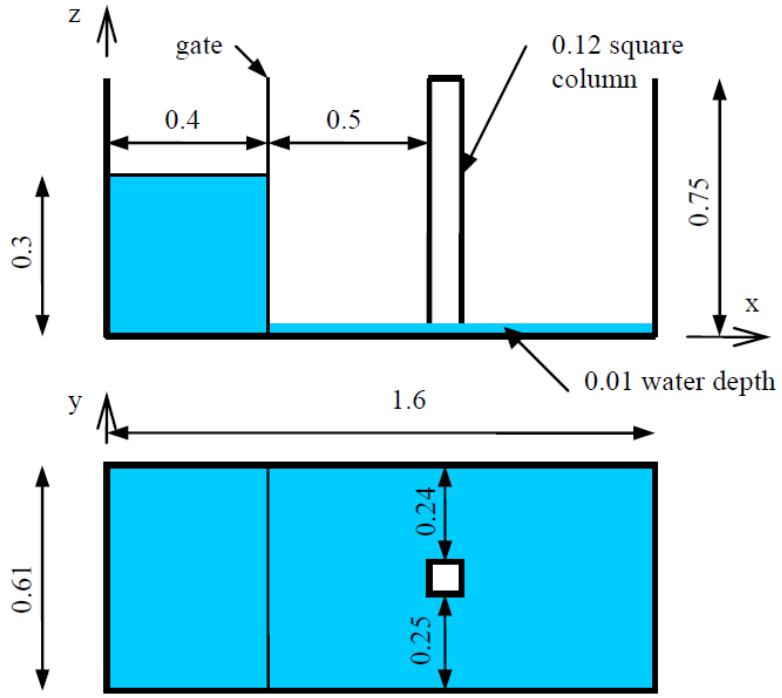

Figure 3.1: Schematic diagram of the inital condition and geometry of the Yeh–Petroff dam break problem (source: Silvester and Cleary [26].)

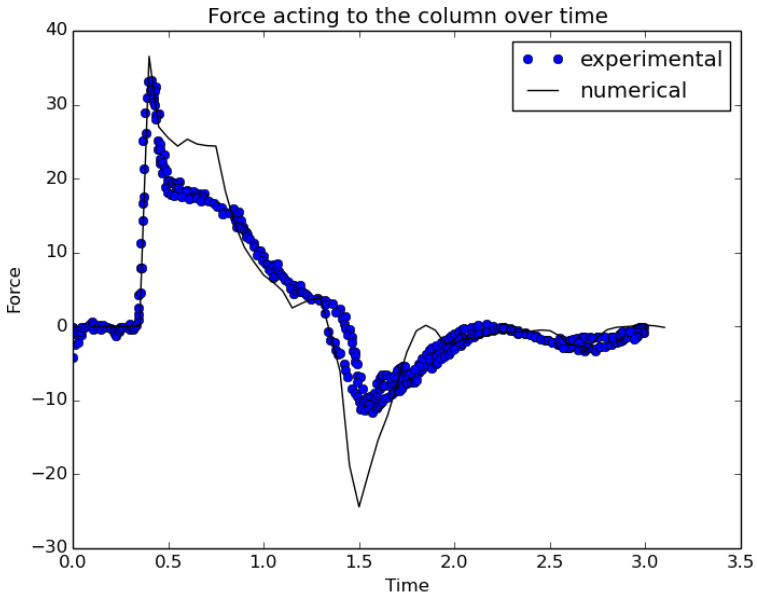

Figure 3.2: Stage results

3.2 Okushiri Benchmark

We set up the Okushiri Island benchmark as published by the

```
The Third International Workshop on Long-Wave Runup Models
June 17-18 2004
Wrigley Marine Science Center
Catalina Island, California
```

`http://isec.nacse.org/workshop/2004_cornell/`

The validation data was downloaded and made available in this directory for convenience but the original data is available at `http://isec.nacse.org/workshop/2004_cornell/bmark2.html` where a detailed description of the problem is also available.

Run `create_okushiri.py` to process the boundary condition and build the mesh before running the script `run_okushiri.py`.

3.2.1 Results

ANUGA should produce results that match the stage values at a number of gauge locations

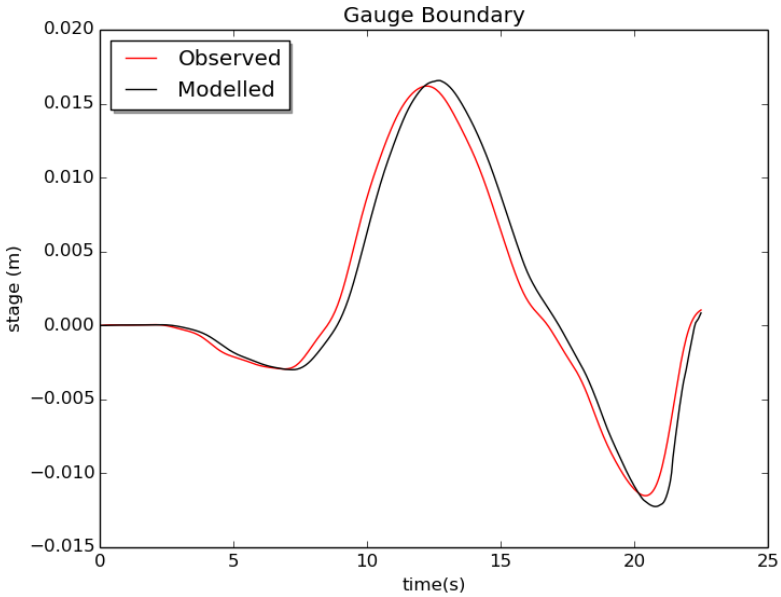

Figure 3.3: Stage at boundary gauge

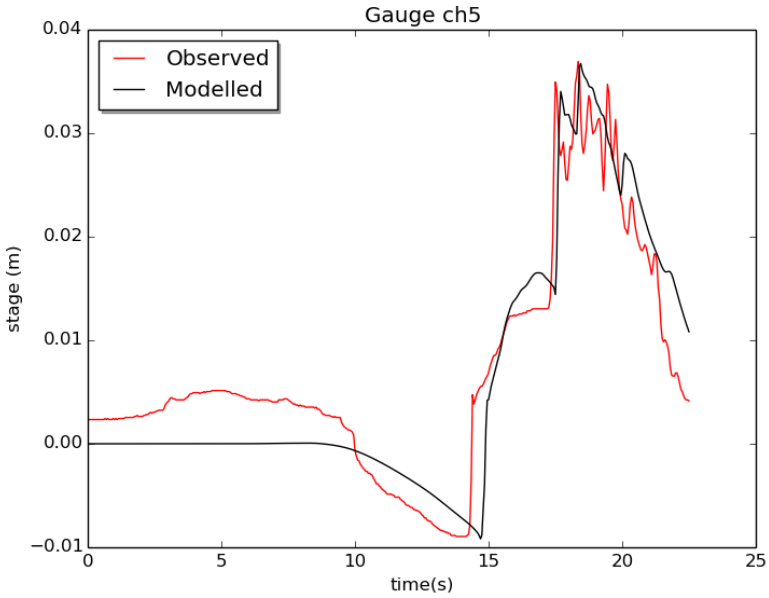

Figure 3.4: Stage at gauge station 5

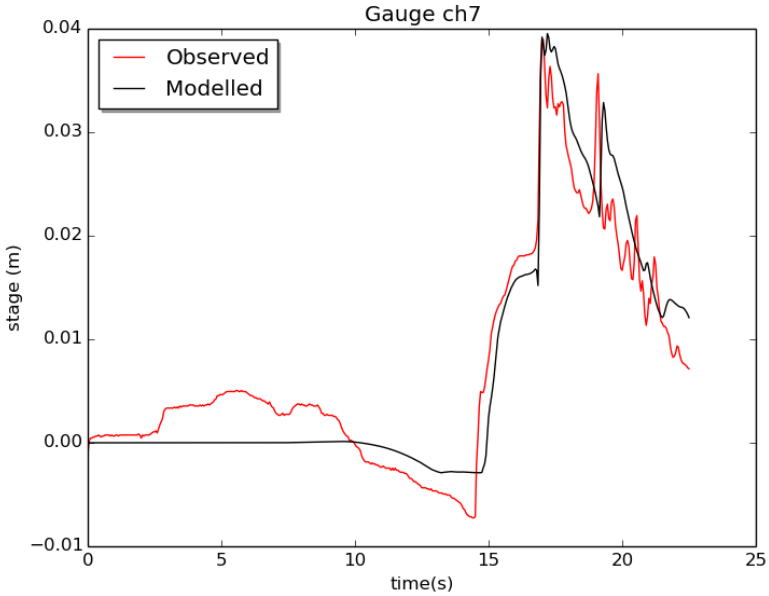

Figure 3.5: Stage at at gauge station 7

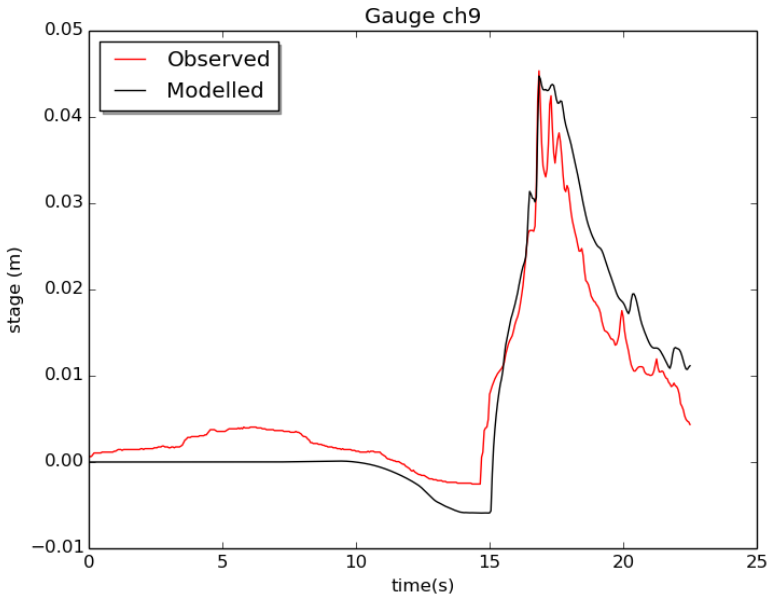

Figure 3.6: Stage at at gauge station 9

3.3 Lid-driven cavity flow

Lid-driven cavity flow is flow in a unit square containing a unit depth of water with horizontal topography. The top (north) boundary has a unit velocity and the other three boundaries are solid wall. The initial condition is water at rest. This is a standard test for numerical methods used to solve the two-dimensional Navier–Stokes equations. This is not a usual test for shallow water models [5]. However, it may benefit to check the behaviour of numerical solutions of ANUGA to this problem.

The analytical solution to this problem is not available, but a large number of researchers have proposed numerical solutions. Some of the literatures amongst others are Cueto-Felgueroso et al. [5] and Erturk et al. [7].

3.3.1 Results

The following figures show numerical solutions of ANUGA to this lid-driven cavity flow problem. We focus on the velocity and velocity fields. Note that the current version of ANUGA is set up for inviscid fluid (water). That is, the Reynolds number is infinity. An accurate result should show secondary vortices around the corners for high Reynolds numbers.

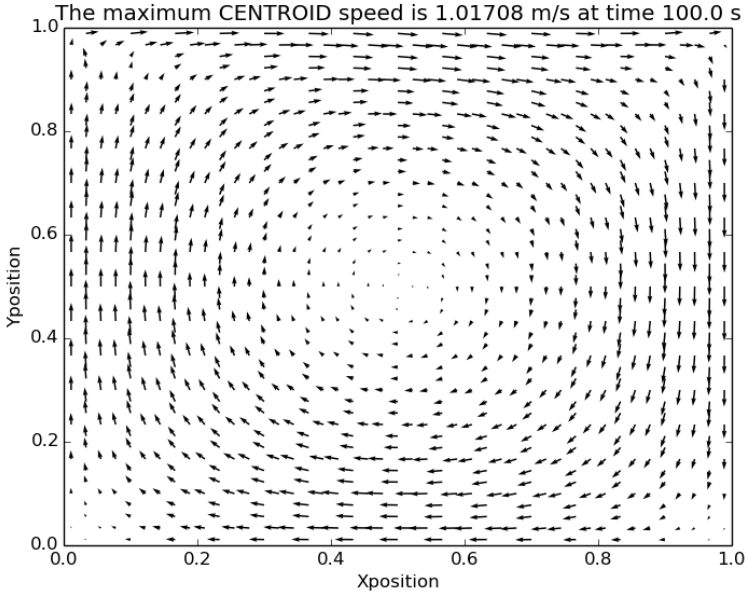

Figure 3.7: Velocity at the centroids of computational elements at an instant of time.

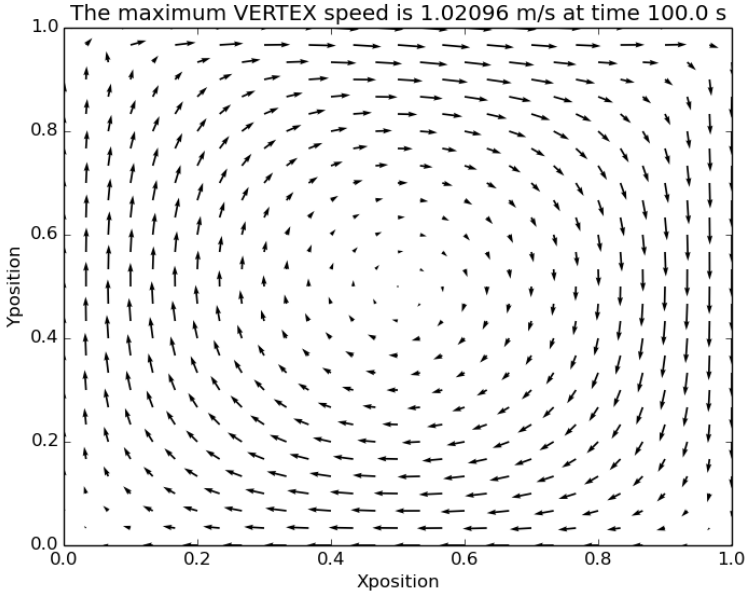

Figure 3.8: Velocity at the vertices of computational elements at an instant of time.

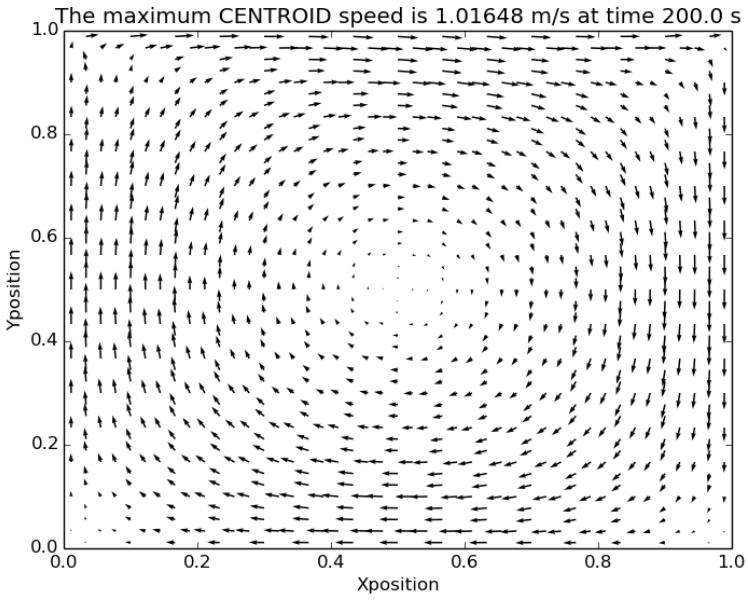

Figure 3.9: Velocity at the centroids of computational elements at the final time step.

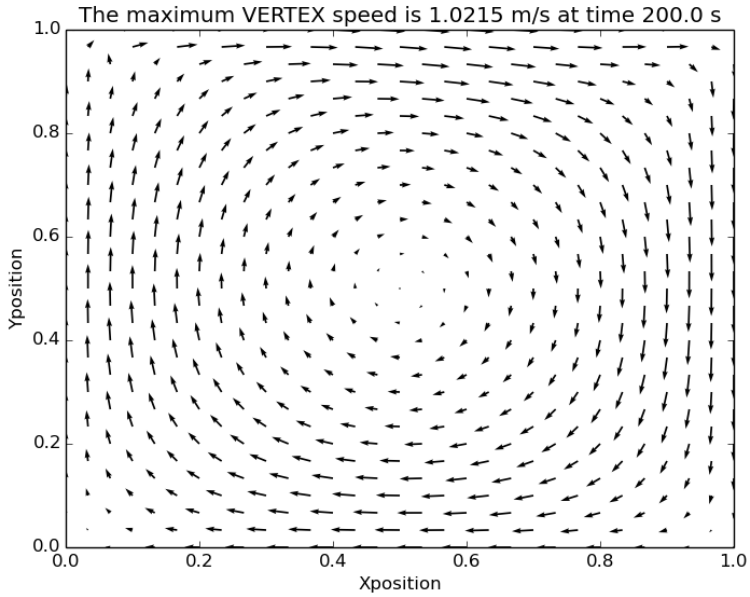

Figure 3.10: Velocity at the vertices of computational elements at the final time step.

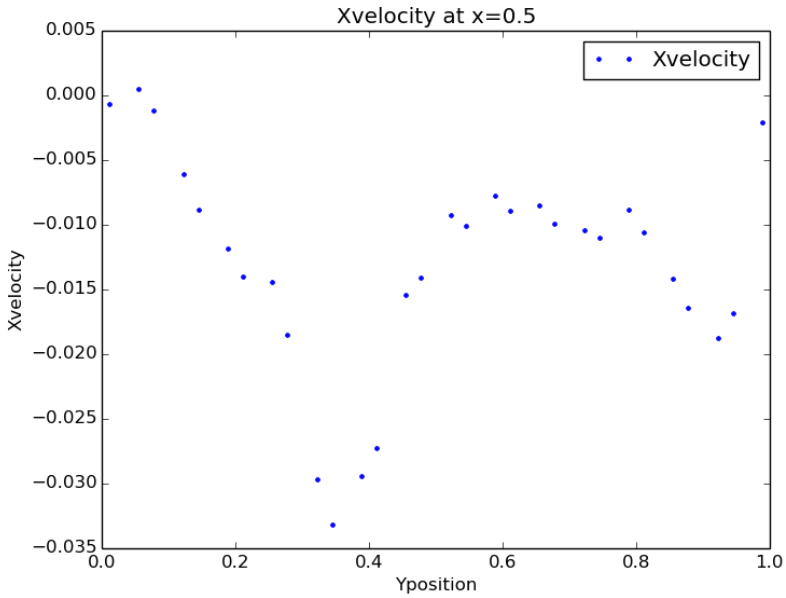

Figure 3.11: Xvelocity at $y = 0.5$.

3.4 Flow over a weir

In this problem water runs up a broad sloping floodplain, which is split into 2 by a thin weir (riverwall). The landward side of the floodplain is initially dry but becomes wet as the water overtops the weir. We use the change in mass on the landward side of the weir to compute the flux over the weir according to ANUGA, and compare with direct computation of the weir equation.

ANUGA allows computation of flow over a weir using the riverwall structure (supported for Discontinuous Elevation Algorithms only as of 01/07/2014). The default method adjusts the edge flux over the weir to satisfy a basic weir relation with Villemonte's submergence correction. However at high submergence ratios, or when the depth of flow over the weir is large compared with the weir height, ANUGA smoothly reverts to the shallow water solution (because the weir relations are not sensible in these situations). This is required so that e.g. a weir of 1cm height covered by flow of 1m is basically no different from the shallow water solution - weir relations by themselves will not achieve this. See the documentation of riverwalls for more information.

3.4.1 Results

The following figures show the discharge over the weir computed with ANUGA, and with the simple weir equation with Villemonte's submergence correction. For reference we also show other weir equations. Before 1100s the discharge is quite similar for all methods. There is still a small difference between ANUGA and the simple-weir equation because the latter is computed only using 2 water level gauges (rather than by integration as in ANUGA), and because of the discretization of the model geometry.

At later times the water elevations on the landward and seaward sides of the wall are very similar, and submergence relations play a greater role in influencing the weir flow. The flow computed by ANUGA reduces much more rapidly than do the other methods. This is due to the blending with the shallow water solution in ANUGA at high submergence ratios (¿ s1). The user can adjust this behaviour in ANUGA by changing the s1, s2, h1, h2 parameters (see riverwall documentation). The Qfactor parameter can also be adjusted to increase/decrease the ideal weir flow.

We have not found much information on how other models treat the transition from weir to shallow water fluxes. However, according to the HecRAS 4.1 Technical Reference manual, HecRas switches to the energy equation when the submergence ratio is 0.95 (default), which corresponds to our default choice of s2=0.95. Our default submergence ratio at which blending begins is s1=0.9.

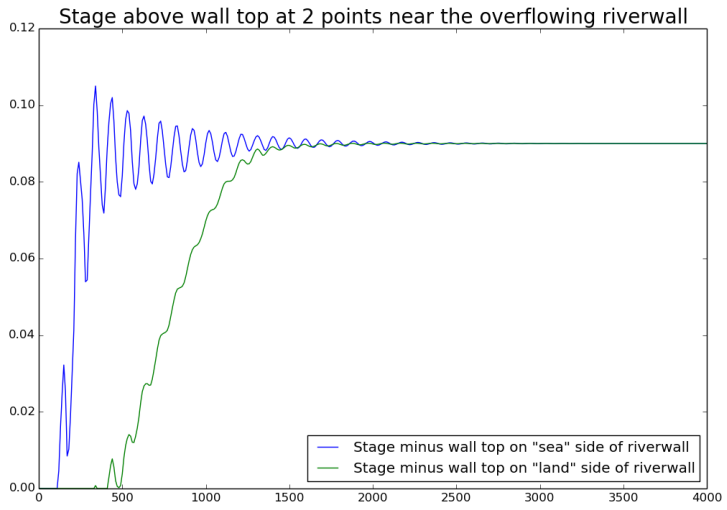

Figure 3.12: Stage (above the riverwall crest) at 2 points either side of the riverwall

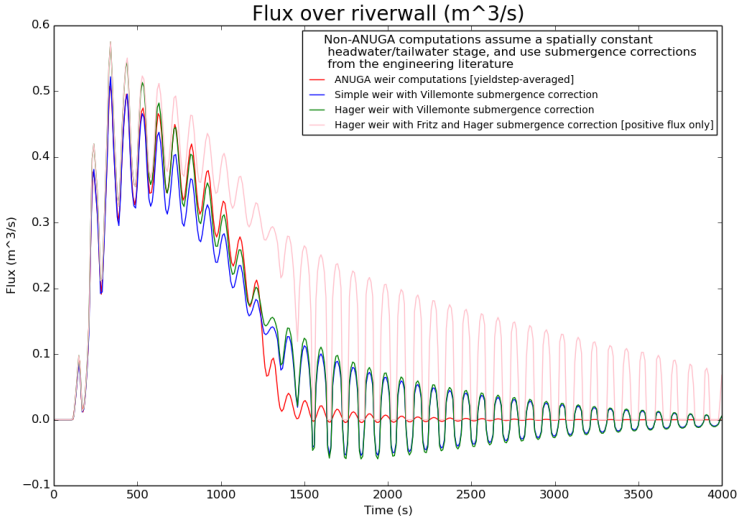

Figure 3.13: Fluxes over the riverwall, computed with a range of methods.

3.5 Bridges in HECRAS and ANUGA

This test compares a prismatic channel flow with a bridge in HECRAS and ANUGA. A 10m wide, 1000m long channel (slope of 1/200, bankfull depth of 1m, rectangular cross-section) flows through a floodplain (10m wide on either side of the channel) (Figure 3.18). 500m downstream there is a bridge with a 1.3m high rectangular opening over the channel, and a deck elevation of -1m. In HECRAS the bridge is modelled using the enegy method, wheras in ANUGA the boyd-box-culvert routines are used for the bridge opening, and the shallow water equations are used for bridge overflow. Both models have a uniform Manning's n of 0.03.

A discharge timeseries is imposed upstream for both models, with the discharge increasing from $1m^3/s$ initially to $70m^3/s$ at the end of the simulation. Details of the model setup can be seen in the code / input files in this directory.

3.5.1 Results

Figure 3.17 show stage timeseries at various stations downstream in each model. The ANUGA and HECRAS results are qualitatively similar. Just upstream of the bridge (stations 525+), ANUGA shows a backwater effect earlier than HECRAS, while the final steady-state stage is somewhat lower than in HECRAS. This is attributable to the different bridge models used (energy equation for HECRAS vs culvert+shallow-water for ANUGA). HECRAS includes several other bridge models (based on the momentum equation or other methods), and these would also give different results.

Another minor point is that for the channelised flow, HECRAS computes the friction slope in the channel using the hydraulic radius, which include the 'bank-drag' effect, whereas ANUGA does not. Hence, even away from the bridge steady-state results can differ slightly.

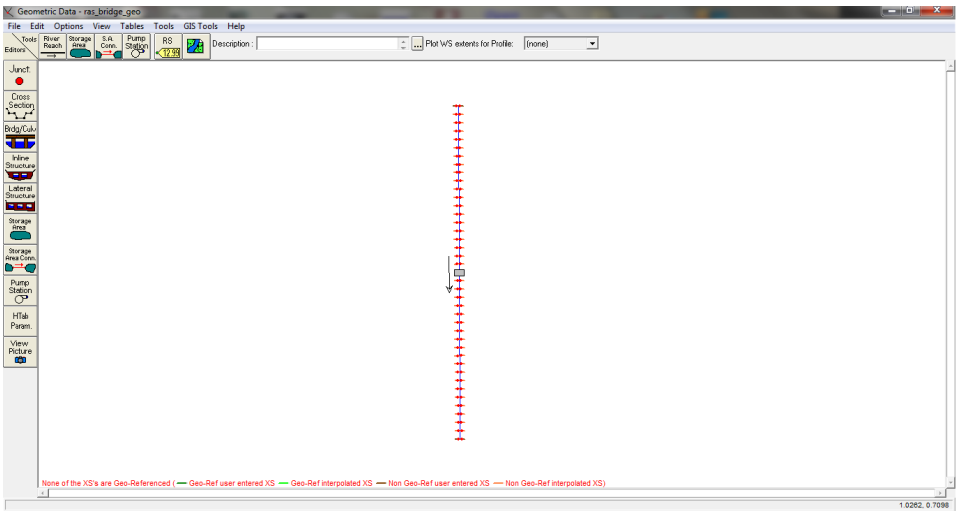

Figure 3.14: Screenshot showing the HECRAS model geometry schematization

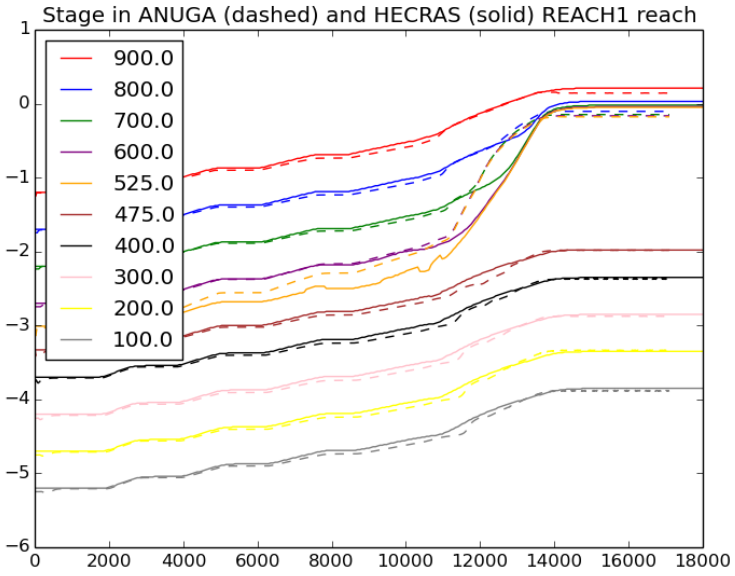

Figure 3.15: Stage at various points downstream in the channel

3.6 Bridges in HECRAS and ANUGA using an internal boundary operator

This test compares a prismatic channel flow with a bridge in HECRAS and ANUGA. A 10m wide, 1000m long channel (slope of 1/200, bankfull depth of 1m, rectangular cross-section) flows through a floodplain (10m wide on either side of the channel) (Figure 3.18). 500m downstream there is a bridge with a 1.3m high rectangular opening over the channel, and a deck elevation of -1m. In HECRAS the bridge is modelled using the energy method, see the associated HECRAS files for details. In ANUGA the bridge is modelled by inserting the bridge deck (upper chord) into the topography, with an internal boundary operator to describe the bridge underflow. The rating curves for the bridge underflow (used to compute the bridge discharge from the upstream and downstream stage) were derived for ANUGA from HECRAS by raising the upper chord of the bridge in HECRAS (far about the flow) and computing internal boundary tables, which were then copied into a csv file for use by ANUGA. The bridge overflow in ANUGA is modelled with the shallow water equations (although riverwalls could also be used to apply weir type equations instead). Both models have a uniform Manning's n of 0.045, which prevents too much supercritical flow in HECRAS (and the associated numerical supression of the inertial terms that HECRAS uses to retain stability).

A discharge timeseries is imposed upstream for both models, with the discharge increasing from $1m^3/s$ initially to $70m^3/s$ at the end of the simulation. Details of the model setup can be seen in the code / input files in this directory.

3.6.1 Results

Figure 3.17 show stage timeseries at various stations downstream in each model. The ANUGA and HECRAS results are qualitatively similar, but differ in detail.

In early stages of the simulation when discharges are lower, ANUGA shows stages slightly below HECRAS (particularly away from the bridge). This reflects the fact that HECRAS models side-wall friction while ANUGA does not, so there is more drag in the HECRAS model.

As the discharge increases, the models show more deviation around the bridge and upstream, and ultimately approach different steady states. At high flows, the main reason for this is that they use different methods to model the bridge overflow, which begins when station 525 exceeds -1m. ANUGA uses the shallow water equations, while HECRAS uses an energy method. Even before this, the models show differences once the flow goes overbank (above -2.4m at station 525). Because the ANUGA model here has a fairly coarse mesh, numerical diffusion causes additional drag for overbank

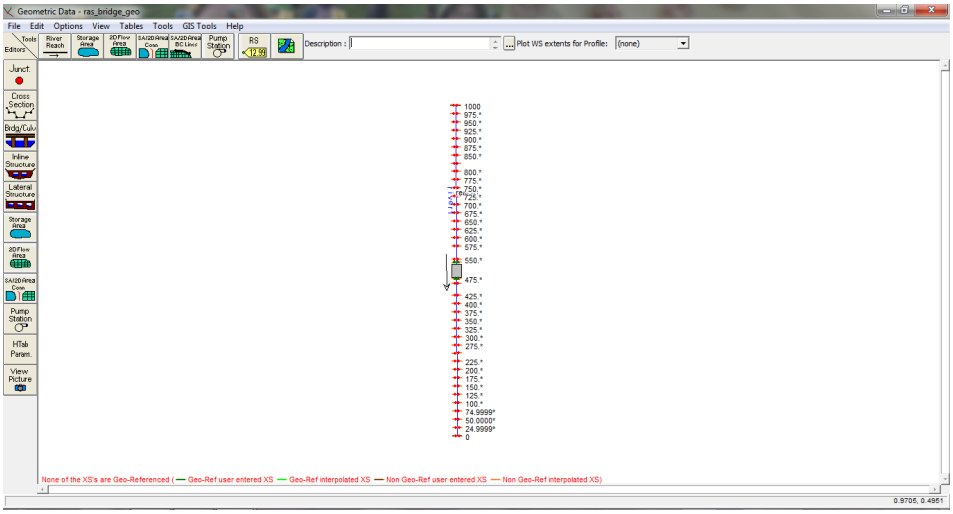

Figure 3.16: Screenshot showing the HECRAS model geometry schematization

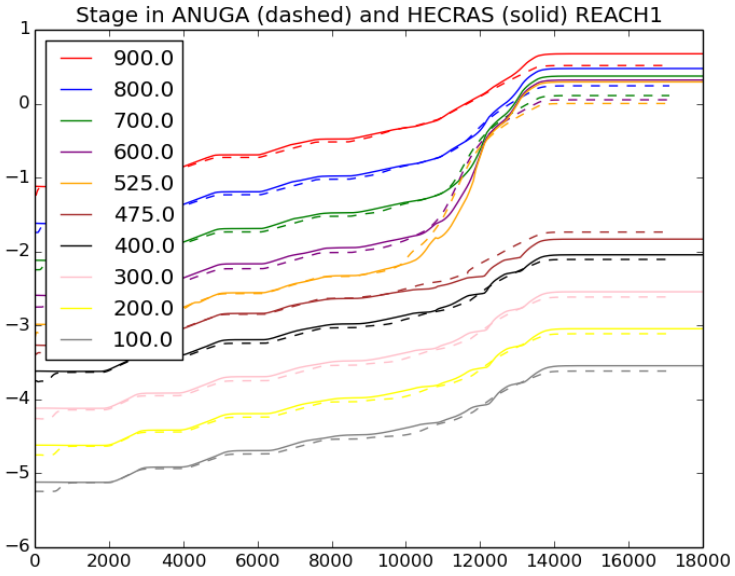

Figure 3.17: Stage at various points downstream in the channel

flows.

Several additional factors will contribute to deviations between the models. ANUGA models cross-channel variations in the water surface elevation, which is assumed constant in HECRAS. The under-bridge flux in ANUGA is based on the water elevations in the central channel up-and-down stream of the bridge, thus the 2D representation will have an effect on the under-bridge flow. Further, since the ANUGA model here is fairly coarsely resolved, the flow details near the bridge are noticably affected by the choice of flow algorithm. The models also flux the momentum under the bridge in different ways. ANUGA's method is to compute the average momentum in each direction along the upstream bridge inflow, and assume that this is advected by the discharge (as computed from the internal boundary rating curves). HECRAS's method is based on the energy equation.

3.7 Lateral weirs in HECRAS and ANUGA

This test compares riverwalls in ANGUA with default lateral structures in HECRAS.

A HECRAS model was set up with 3 uniform parallel channels ('left', 'middle', 'right', orientations defined when looking downstream). All channels had lengths of 1000m, bed-slope 3/1000, manning's n of 0.03, while their widths were 10m, 20m, and 10m respectively (Figure 3.18). The cross-sections were all nearly-flat (three-points with bank elevations 1cm above the central bed elevation), and for all reaches the most upstream cross-section (1000) had an elevation of 0m. These three channels were connected with broad-crested lateral weirs (using HECRAS's default lateral weir drag coefficient of 1.1 in metric units). The 'right' and 'middle' channels were connected with a 198m long weir with an elevation 0.5m above the bed, from stations 799 to 601. The 'left' and 'middle' channels were connected with a 198m long weir with an elevation 0.5m above the bed from stations 699 to 501.

Throughout the simulation the 'left' and 'right' channels were given a discharge of $0.1\text{m}^3/\text{s}$ (just enough to prevent them drying, which causes numerical blow-up in in HECRAS). The 'middle' channel was given a discharge timeseries, increasing from $1\text{m}^3/\text{s}$ to $21\text{m}^3/\text{s}$ over a few hours of simulated time. The entire model is run for 24hours.

As the discharge in the central channel increases, water starts to overtop the riverwalls and flows into the side channels. The loss/gain and final equilibrium flow state in each channel is determined by the flow over the riverwalls, which is itself a function of the stage in each river. Although both riverwalls are 0.5m above the bed, the 'right' channel receives more water than the 'left' channel because it has the most upstream connection to the 'middle' channel. Further downstream the 'middle' channel has already lost a significant part of its discharge, so it flows less deeply and there is less flux over the more downstream riverwall.

An analogous ANUGA model was set up with riverwalls connecting 3 channels. The 'Qfactor' for both riverwalls was set to ($1.1/1.7 \simeq 0.65$) to make the ANUGA riverwall drag coefficient equivalent to the default HECRAS drag coefficient (the default Qfactor in ANUGA is 1). The same discharge timeseries and elevations were used. The manning's n values were slightly increased to account for the fact that HECRAS uses side-wall friction in the channels, whereas ANUGA doesn't. The correction was derived by equating the ANUGA and HECRAS friction slope terms assuming a final flow depth of $d \simeq 0.5m$, and channel width of $w \simeq 10\text{m}$. Denoting n_A as ANUGA's manning's n and n_H as HECRAS's value (0.03), we have:

$$n_A \simeq n_H \frac{d^{2/3}}{(\frac{dw}{2d+w})^{2/3}} \simeq 0.032 \tag{3.1}$$

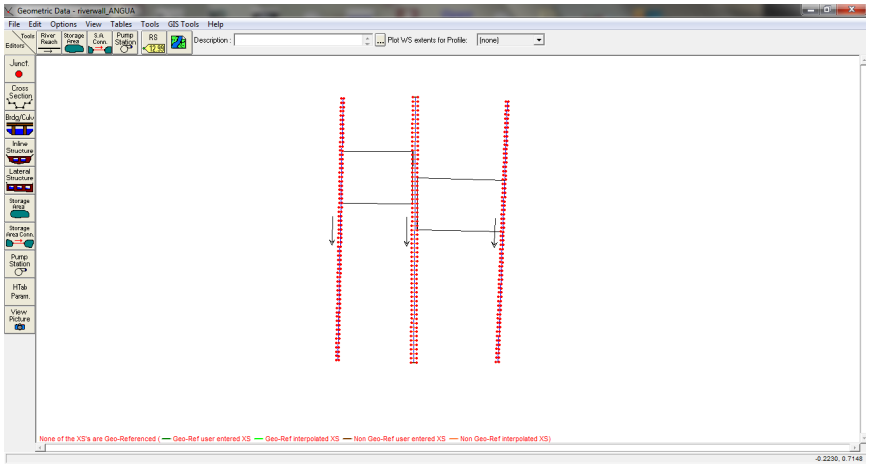

Figure 3.18: HECRAS model geometric schematization. The 'right' channel appears on the left side of this figure, and the 'left' on the right.

where the denominator on the right hand side is the hydraulic radius. This correction is not exact since the depths and widths actually vary, but despite those second order effects it does improve the agreement between the 2 models.

The initial conditions in each model are slightly different but this is only important in the first hour of simulation. HECRAS needs 'well-behaved' initial conditions to maintain stability.

3.7.1 Results

Figures 3.19-3.21 show stage timeseries at various stations downstream in each channel. The results are qualitatively similar, with stages typically differing by a few cm. In the downstream parts of the left/right channels, the stage is completely determined by the mass flux over the upstream weirs, and so the agreement between HECRAS and ANUGA here shows that both models are predicting a similar mass flux.

The main difference between the 2 models is in areas just upstream of the weir (800 on the right channel, 700 on the left), where HECRAS predicts a greater a backwater effect in the receiving channel than ANUGA. Further investigation has shown this is because of differences in the transport of momentum over the riverwall. HECRAS apparently only transfers mass over the weir, whereas ANUGA transfers both mass and momentum. This causes more stagnation at the upstream parts of the riverwall overflow in HECRAS, since the water is transferred to the side channels without a downstream component of momentum. We have done other ANUGA runs where the momentum flux over the weir was forced to zero (by modifying

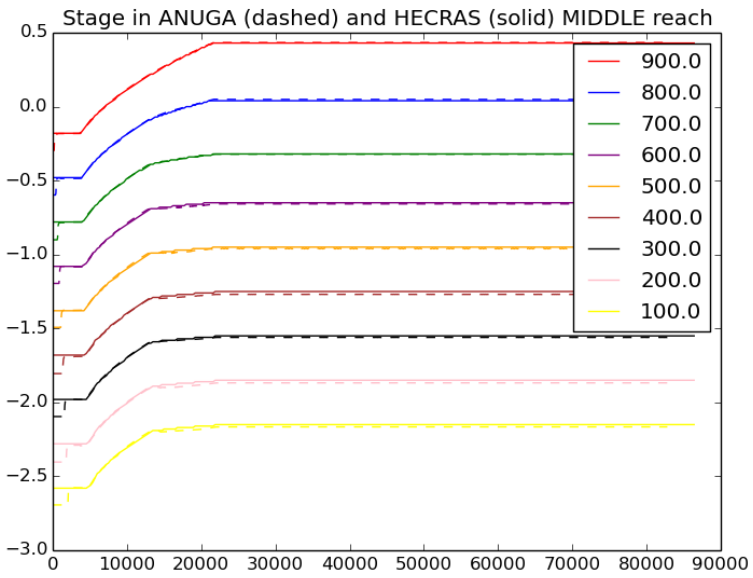

Figure 3.19: Stage at various points downstream in the middle channel

ANUGA's source code), and in that instance the models agree well in the aforementioned areas as well.

Irrespective, the main point of this comparison is that both ANUGA and HECRAS are giving similar results for this case study.

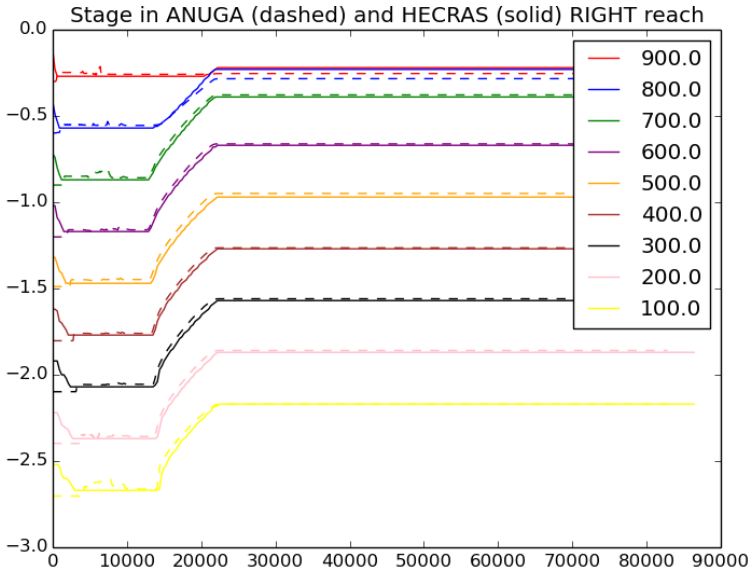

Figure 3.20: Stage at various points downstream in the right channel

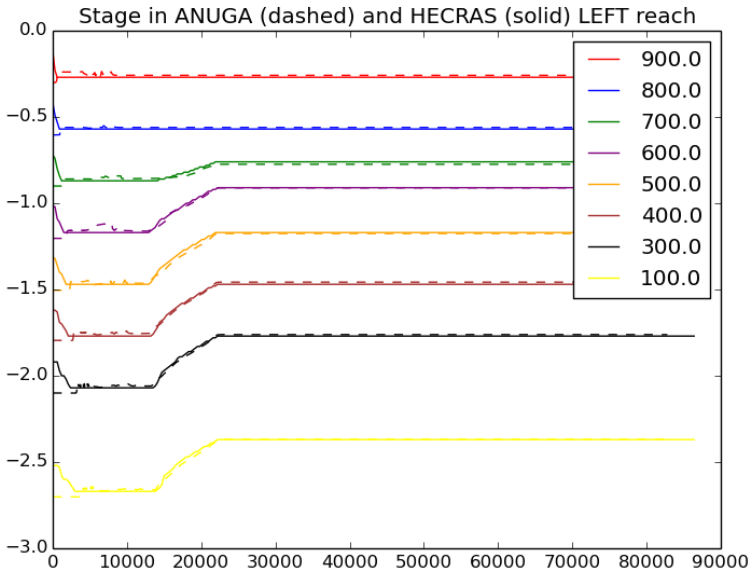

Figure 3.21: Stage at various points downstream in the left channel

3.8 Tides in HECRAS and ANUGA

This test compares idealised tidal channel flow in HECRAS and ANUGA. The tidal amplitude (0.4m) is a significant fraction of the channel depth ($\simeq$ 1m), so nonlinear tidal deformation is significant.

A 20m wide, 1000m long straight channel with rectangular cross-section flows through a floodplain (10m wide on either side of the channel). Upstream of 220m the bed elevation is constant (1m below the floodplain), downstream of 100m it is 3m below the floodplain, and it varies linearly in between. The floodplain has a constant elevation (1m). Manning's n is 0.03. The upstream boundary is reflective, while at the downstream boundary a stage timeseries $y(t)$ is imposed (where t is time in seconds):

$$y = 0.6 + 0.4 * \sin(2\pi t/(1800))$$

3.9 Results

Figure 3.22 show stage timeseries at various stations downstream in each model. For visual clarity the gauges are offset vertically. The ANUGA and HECRAS results should be visually indistinguishable. There is a clear deformation of the tide as it travels upstream, with the incoming tide having a shorter duration than the outgoing tide at upstream stations, which is typical for tides in shallow channels when overbank effects are not dominant. In this example there is minor overbank inundation in parts of both models, but it is just a few cm deep.

Note that this ANUGA model uses a coarse mesh with discontinuous elevation to resolve the banks, so this example should not run with non-discontinuous elevation flow algorithms.

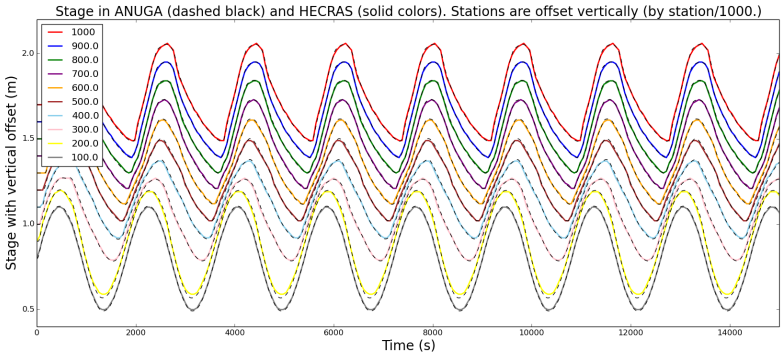

Figure 3.22: Tidal levels in HECRAS and ANUGA

3.10 Radial dam break on a dry bed

A radial dam break test problem involving a dry bed. Should show a rarefaction fan. Note that the reference solution is found from the 1D FVM for SWE involving varying width and topography. See a paper of Roberts and Wilson [25].

3.10.1 Results

We should see excellent agreement between the reference and numerical solutions.

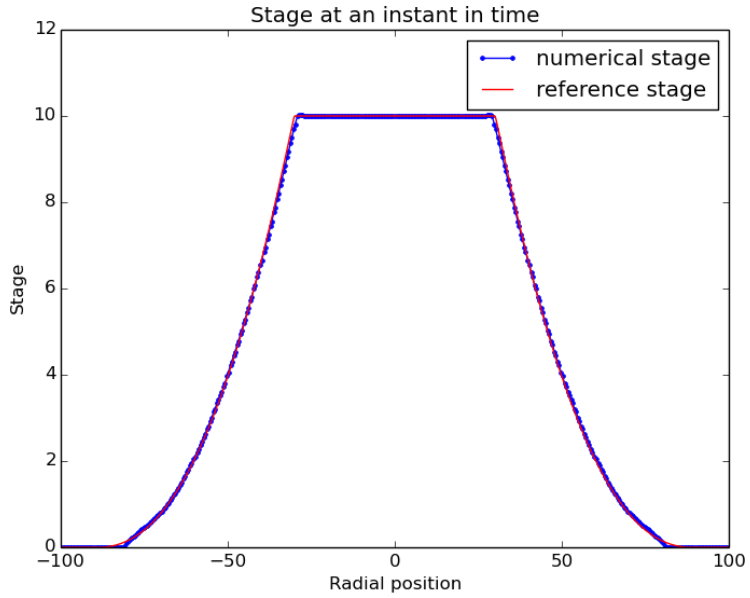

Figure 3.23: Stage results

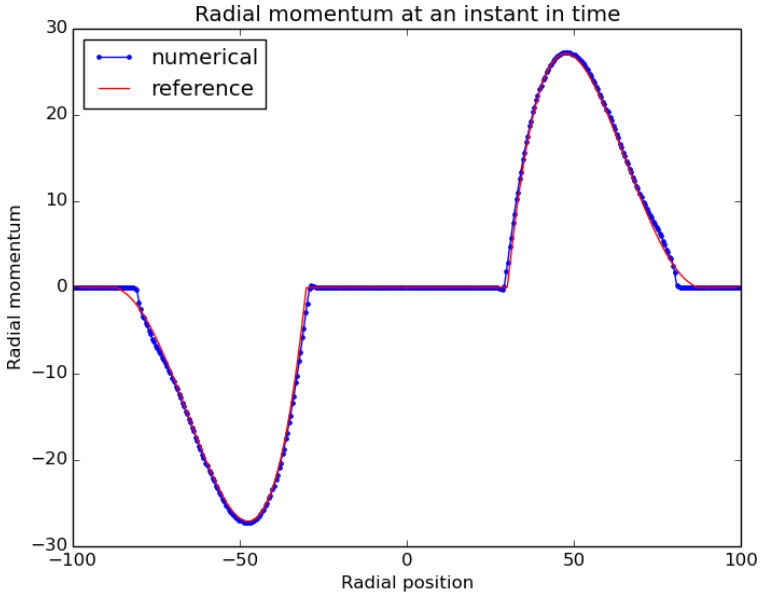

Figure 3.24: Radial momentum results

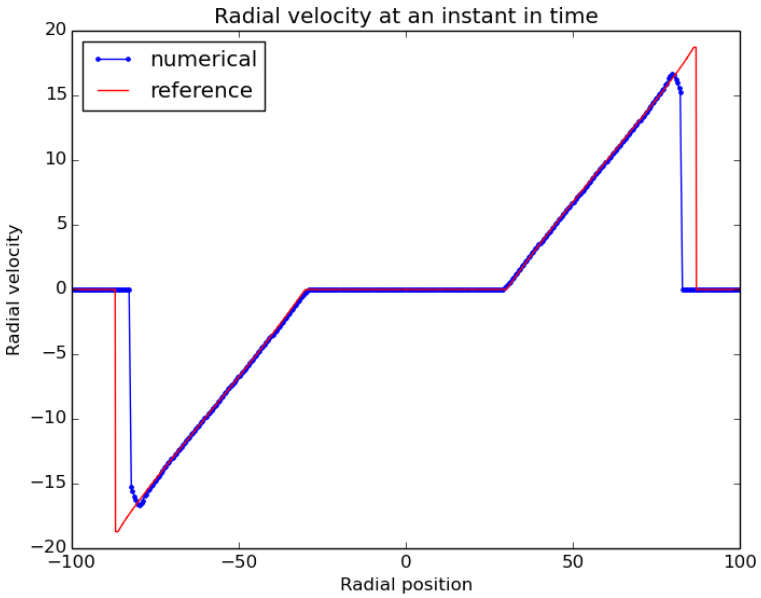

Figure 3.25: Radial velocity results

3.11 Radial dam break on a wet bed

A radial dam break test problem involving a wet bed. Should show a rarefaction fan and a shock. Note that the reference solution is found from the 1D FVM for SWE involving varying width and topography. See a paper of Roberts and Wilson [25].

3.11.1 Results

We should see excellent agreement between the reference and numerical solutions.

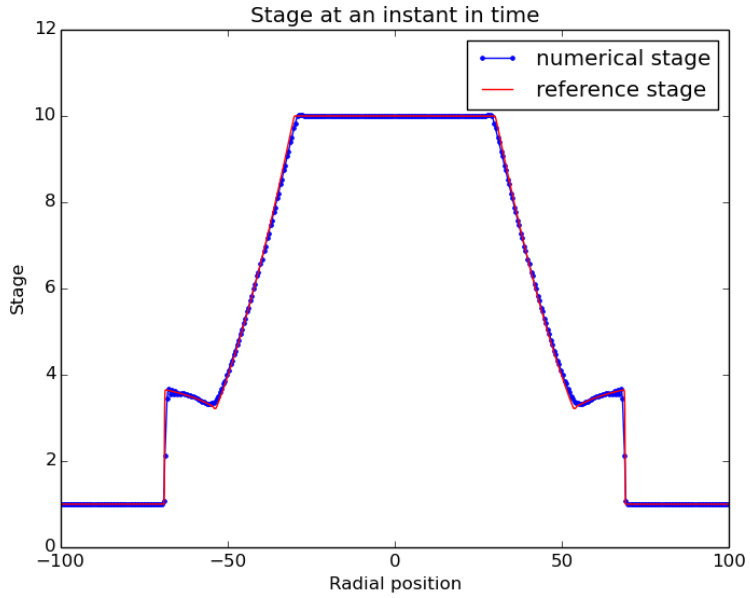

Figure 3.26: Stage results

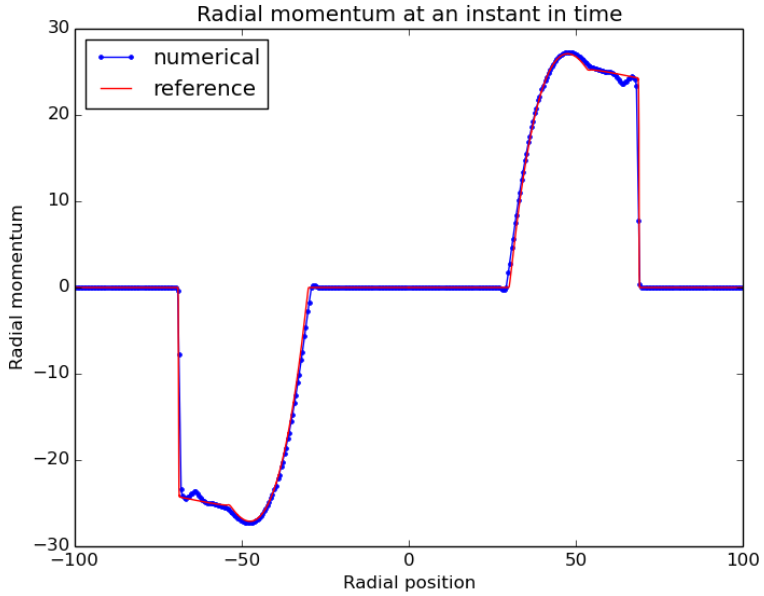

Figure 3.27: Radial momentum results

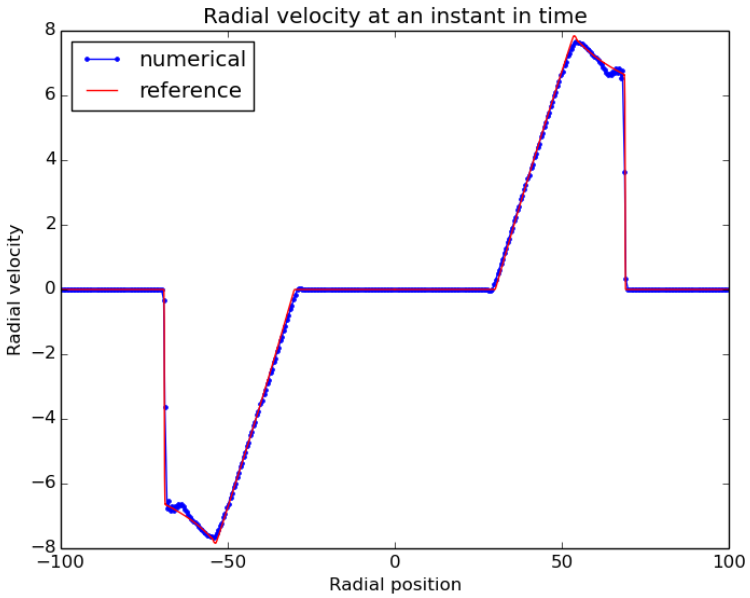

Figure 3.28: Radial velocity results

Chapter 4

Realistic large-scale cases

Code for a number of realistic applications is in the case_studies directory, however they are not included here by default, because they take a long time to run.

Appendix A

Adding New Tests

To setup a new validation test, create a test directory under one of the validation directories. In that directory there should be the test code, a TEX file `results.tex` and a python script `produce_results.py`, which runs the simulation and produces the outputs. Copy the format from one of the other test directories.

In this TEX file, `report.tex`, add a line

```
\inputresults{../Directory/Name}
```

A.1 Algorithm Parameters

Note that parameters can be communicated from the `local_parameters.py` file in the `validation_tests/reports` directory. If there is no file `local_parameters.py` then the parameters are taken from the `anuga.validation_utilities.parameters`.

In particular the values of `alg` (flow algorithm) and `cfl` (CFL Condition) are passed as command options when calling `produce_results.py` in the test directories.

Within ANUGA script you can obtain command line parameters via

```
args = anuga.get_args()
alg = args.alg
verbose = args.verbose
```

to obtain the values of `alg`(flow algorithm) and `verbose`(flag)

You can pass though the standard parameters as follows

```
from anuga.validation_utilities.parameters import alg
from anuga.validation_utilities.parameters import cfl
```

A.2 Generic form of `produce_results.py`

The `produce_results.py` files in the test directories should have the following general form

```
import anuga
from anuga.validation_utilities import produce_report

args = anuga.get_args()

produce_report('run_simulation.py', args=args)
```

Bibliography

[1] H. Arnason, C. Petroff, and H. Yeh. Tsunami bore impingement onto a vertical column. *Journal of Disaster Research*, 4(6):391–403, 2009. www.fujipress.jp.

[2] G. F. Carrier and H. P. Greenspan. Water waves of finite amplitude on a sloping beach. *Journal of Fluid Mechanics*, 4(1):97–109, 1958. http://dx.doi.org/10.1017/S0022112058000331.

[3] G. F. Carrier, T. T. Wu, and H. Yeh. Tsunami run-up and drawdown on a plane beach. *Journal of Fluid Mechanics*, 475:79–99, 2003. http://dx.doi.org/10.1017/S0022112002002653.

[4] P. Constabile, C. Constanzo, and F. Macchione. A storm event watershed model for surface runoff based on 2d fully dynamic wave equations. *Hydrological Processes*, 27(4):554–569, 2013. http://dx.doi.org/10.1002/hyp.9237.

[5] L. Cueto-Felgueroso, I. Colominas, J. Fe, F. Navarrina, and M. Casteleiro. High-order finite volume schemes on unstructured grids using moving least-squares reconstruction. application to shallow water dynamics. *International Journal for Numerical Methods in Engineering*, 65(3):295–331, 2006. http://dx.doi.org/10.1002/nme.1442.

[6] O. Delestre, C. Lucas, P.-A. Ksinant, F. Darboux, C. Laguerre, T.-N. Tuoi Vo, F. James, and S. Cordier. Swashes: a compilation of shallow water analytic solutions for hydraulic and environmental studies. *International Journal for Numerical Methods in Fluids*, Early View, 2012. http://dx.doi.org/10.1002/fld.3741.

[7] E. Erturk, T. C. Corke, and C. Gokcol. Numerical solutions of 2-d steady incompressible driven cavity flow at high reynolds numbers. *International Journal for Numerical Methods in Fluids*, 48(7):747–774, 2005. http://dx.doi.org/10.1002/fld.953.

[8] M. Gomez-Gesteira and R. A. Dalrymple. Using a three-dimensional smoothed particle hydrodynamics method for wave impact on a tall

structure. *Journal of Waterway, Port, Coastal, and Ocean Engineering*, 130(2):63–69, 2004. http://dx.doi.org/10.1061/(ASCE)0733-950X(2004)130:2(63).

[9] N. Goutal and F. Maurel. *Technical Report HE-43/97/016/B: Proceedings of the 2nd Workshop on Dam-Break Wave Simulation.* Direction des études et recherches, Electricité de France, Paris, 1997.

[10] B. Johns. Numerical integration of the shallow water equations over a sloping shelf. *International Journal for Numerical Methods in Fluids*, 2(3):253–261, 1982. http://dx.doi.org/10.1002/fld.1650020304.

[11] Georges Kesserwania and Yueling Wang. Discontinuous galerkin flood model formulation: luxury or necessity? *Water Resources Research*, Accepted Article, 2014.

[12] A. Kurganov and D. Levy. Central-upwind schemes for the Saint-Venant system. *ESAIM: M2AN*, 36(3):397–425, 2002. http://dx.doi.org/10.1051/m2an:2002019.

[13] A. Kurganov, S. Noelle, and G. Petrova. Semidiscrete central-upwind schemes for hyperbolic conservation laws and Hamilton-Jacobi equations. *SIAM Journal on Scientific Computing*, 23(3):707–740, 2001. http://dx.doi.org/10.1137/S1064827500373413.

[14] I. MacDonald, M. J. Baines, N. K. Nichols, and P. G. Samuels. Steady open channel test problems with analytic solutions. *Numerical Analysis Report 3/95, University of Reading*, 1995. http://www.reading.ac.uk/web/FILES/maths/03-95.pdf.

[15] I. MacDonald, M. J. Baines, N. K. Nichols, and P. G. Samuels. Analytic benchmark solutions for open-channel flows. *Journal of Hydraulic Engineering*, 123(11):1041–1045, 1997. http://dx.doi.org/10.1061/(ASCE)0733-9429(1997)123:11(1041).

[16] A. Mangeney, P. Heinrich, and R. Roche. Analytical solution for testing debris avalanche numerical models. *Pure and Applied Geophysics*, 157(6–8):1081–1096, 2000. http://dx.doi.org/10.1007/s000240050018.

[17] S. Mungkasi and S. G. Roberts. On the best quantity reconstructions for a well balanced finite volume method used to solve the shallow water wave equations with a wet/dry interface. *ANZIAM Journal (E)*, 51:C48–C65, 2010. http://journal.austms.org.au/ojs/index.php/ANZIAMJ/article/view/2576/1289.

[18] S. Mungkasi and S. G. Roberts. A new analytical solution for testing debris avalanche numerical models. *ANZIAM Journal (E)*, 52:C349–C363, 2011. http://journal.austms.org.au/ojs/index.php/ANZIAMJ/article/view/3785/1465.

[19] S. Mungkasi and S. G. Roberts. Analytical solutions involving shock waves for testing debris avalanche numerical models. *Pure and Applied Geophysics*, 169(10):1847–1858, 2012. http://dx.doi.org/10.1007/s00024-011-0449-1.

[20] S. Mungkasi and S. G. Roberts. Approximations of the Carrier–Greenspan periodic solution to the shallow water wave equations for flows on a sloping beach. *International Journal for Numerical Methods in Fluids*, 69(4):763–780, 2012. http://dx.doi.org/10.1002/fld.2607.

[21] M. Naaim, S. Vial, and R. Couture. Saint Venant approach for rock avalanches modelling. *Proceedings of the Saint Venant Symposium: Multiple scale analyses and coupled physical systems,* Presses de l'École Nationale des Ponts et Chaussées, Paris, pages 61–69, 1997.

[22] S. Popinet. Adaptive modelling of long-distance wave propagation and fine-scale flooding during the tohoku tsunami. *Natural Hazards and Earth System Science*, 12:1213–1227, 2012. http://dx.doi.org/10.5194/nhess-12-1213-2012.

[23] A. Ritter. Die fortpflanzung der wasserwellen. *Zeitschrift des Vereines Deutscher Ingenieure*, 36(33):947–954, 1892.

[24] S. Roberts, O. Nielsen, D. Gray, and J. Sexton. *ANUGA User Manual.* Geoscience Australia, 2010. http://anuga.anu.edu.au.

[25] S. G. Roberts and P. Wilson. A well balanced scheme for the shallow water wave equations in open channels with (discontinuous) varying width and bed. *ANZIAM Journal (E)*, 52:C967–C987, 2011. http://journal.austms.org.au/ojs/index.php/ANZIAMJ/article/view/3948/1542.

[26] T. B. Silvester and P. W. Cleary. *Wave-structure interaction using smoothed particle hydrodynamics.* Fifth International Conference on CFD in the Process Industries, 13–15 December 2006, CSIRO, Melbourne, Australia, 2006. www.cfd.com.au/cfd_conf06/PDFs/026Sil.pdf.

[27] J. J. Stoker. The formation of breakers and bores. *Communications on Pure and Applied Mathematics*, 1(1):1–87, 1948. http://dx.doi.org/10.1002/cpa.3160010101.

[28] J. J. Stoker. *Water Waves: The Mathematical Theory with Application*. Interscience Publishers, New York, 1957. http://onlinelibrary.wiley.com/book/10.1002/9781118033159.

[29] W. C. Thacker. Some exact solutions to the nonlinear shallow water equations. *Journal of Fluid Mechanics*, 107:499–508, 1981. http://dx.doi.org/10.1017/S0022112081001882.

[30] S. B. Yoon and J. H. Cho. Numerical simulation of coastal inundation over discontinuous topography. *Water Engineering Research*, 2(2):75–87, 2001.